

AD \_\_\_\_\_

Award Number: DAMD17-01-1-0502

TITLE: Breast Cancer Detection and Management Using 3D  
Quantitative Ultrasonic Diffraction Tomography

PRINCIPAL INVESTIGATOR: Xiaochuan Pan, Ph.D.

CONTRACTING ORGANIZATION: The University of Chicago  
Chicago, Illinois 60637

REPORT DATE: May 2002

TYPE OF REPORT: Annual

PREPARED FOR: U.S. Army Medical Research and Materiel Command  
Fort Detrick, Maryland 21702-5012

DISTRIBUTION STATEMENT: Approved for Public Release;  
Distribution Unlimited

The views, opinions and/or findings contained in this report are those of the author(s) and should not be construed as an official Department of the Army position, policy or decision unless so designated by other documentation.

20030923 086

# REPORT DOCUMENTATION PAGE

Form Approved  
OMB No. 074-0188

Public reporting burden for this collection of information is estimated to average 1 hour per response, including the time for reviewing instructions, searching existing data sources, gathering and maintaining the data needed, and completing and reviewing this collection of information. Send comments regarding this burden estimate or any other aspect of this collection of information, including suggestions for reducing this burden to Washington Headquarters Services, Directorate for Information Operations and Reports, 1215 Jefferson Davis Highway, Suite 1204, Arlington, VA 22202-4302, and to the Office of Management and Budget, Paperwork Reduction Project (0704-0188), Washington, DC 20503.

1. AGENCY USE ONLY (Leave blank)

2. REPORT DATE  
May 2002

3. REPORT TYPE AND DATES COVERED  
Annual (1 May 01 - 30 Apr 02)

4. TITLE AND SUBTITLE

Breast Cancer Detection and Management Using 3D  
Quantitative Ultrasonic Diffraction Tomography

5. FUNDING NUMBERS

DAMD17-01-1-0502

6. AUTHOR(S)

Xiaochuan Pan, Ph.D.

7. PERFORMING ORGANIZATION NAME(S) AND ADDRESS(ES)

The University of Chicago  
Chicago, Illinois 60637

E-Mail: xpan@uchicago.edu

8. PERFORMING ORGANIZATION  
REPORT NUMBER

9. SPONSORING / MONITORING AGENCY NAME(S) AND ADDRESS(ES)

U.S. Army Medical Research and Materiel Command  
Fort Detrick, Maryland 21702-5012

10. SPONSORING / MONITORING  
AGENCY REPORT NUMBER

11. SUPPLEMENTARY NOTES

12a. DISTRIBUTION / AVAILABILITY STATEMENT

Approved for Public Release; Distribution Unlimited

12b. DISTRIBUTION CODE

13. Abstract (Maximum 200 Words) (abstract should contain no proprietary or confidential information)

The broad objective of the proposed project is to investigate, develop, and evaluate the application of three-dimensional (3D) ultrasonic diffraction tomography (UDT) for detection of breast cancer. UDT can be viewed as a generalization of X-ray tomography where X-rays have been replaced with an acoustical wavefield. It can determine refractive index distributions within the breast that are of interest clinically and can be an excellent imaging modality for breast cancer because it can provide important information complementary to that obtained from mammograms and because it is non-invasive, free of radiation hazard, and reproducible. While UDT promises several potentially important advantages over conventional ultrasonic imaging and has found important uses in a wide variety of engineering and scientific disciplines, its application to breast imaging still remains largely unexplored. In the last year, our research on this project has, we believe, been successful and productive. We have investigated, developed, and evaluated computationally efficient and statistically optimal algorithms for accurate reconstruction of UDT images that may find applications in UDT imaging of breast cancer. We have made contributions to UDT research, as summarized in the report, by addressing numerous scientific and engineering problems involved in UDT image reconstruction. These results are necessary in making UDT a viable medical technique for imaging of breast cancer.

14. SUBJECT TERMS

ultrasonic diffraction tomography, breast cancer detection

15. NUMBER OF PAGES

69

16. PRICE CODE

17. SECURITY CLASSIFICATION  
OF REPORT

Unclassified

18. SECURITY CLASSIFICATION  
OF THIS PAGE

Unclassified

19. SECURITY CLASSIFICATION  
OF ABSTRACT

Unclassified

20. LIMITATION OF ABSTRACT

Unlimited

## Table of Contents

Cover.....	1
SF 298.....	2
Introduction.....	4
Body.....	4
Key Research Accomplishments.....	7
Reportable Outcomes.....	8
Conclusions.....	9
References.....	10
Appendices.....	11

# 1 Introduction

Ultrasonic diffraction tomography (UDT) [1–3] can be viewed as a generalization of X-ray tomography where X-rays have been replaced with an acoustical wavefield. Because UDT is non-invasive, free of radiation hazard, and reproducible, it is potentially an excellent tool for imaging of breast cancer [4, 5]. While UDT promises several potentially important advantages over conventional ultrasonic imaging and has found important uses in a wide variety of engineering and scientific disciplines, its application to imaging of breast cancer still remains largely unexplored. The broad objective of the proposed project is to investigate, develop, and evaluate computationally efficient [6] and statistically optimal [7–9] algorithms for accurate image reconstruction in three-dimensional (3D) UDT imaging of the breast cancer. In the last year, our research on this project has, we believe, been successful and productive. The report below summarizes our research activities and results on the project to date.

## 2 Body

Our research activities on the project to date can be grouped naturally into 4 categories. The first was the investigation of efficient linear algorithms for image reconstruction from 3D data and from minimum scan data. The second was the development of efficient nonlinear algorithms for 2D and 3D image reconstructions. The third was the applications of the developed algorithms to simulated and experimental data for evaluation of their performance. Finally, as a by product, we developed short-scan reconstruction algorithms for reflection-mode ultrasound tomography that can also be a potentially important modality for imaging of the breast cancer.

### 2.1 Development of efficient linear reconstruction algorithms

In breast imaging applications of ultrasound, the first-order Born or Rytov approximations are typically not valid, and consequently, a linearized Helmholtz equation may not accurately describe the relationship between the measured scattered wavefield and the scattering tissue [10–18]. However, many nonlinear reconstruction algorithms that account for multiple-scattering effects, including the ones we discuss below [19], involve the recursive application of a linear reconstruction algorithm (that assumes the validity of the first-order Born or Rytov approximation.) It is therefore very important to develop computational efficient and numerically robust linear reconstruction algorithms for DT. Below, we discuss our results on this salient topic.

#### 2.1.1 Development of 3D efficient reconstruction algorithms

In 2D DT, the filtered backpropagation (FBPP) algorithm is [1] widely used for image reconstruction and is generally regarded as being more accurate than direct Fourier reconstruction approaches. However, objects such as the female breast are inherently three-dimensional and

must be reconstructed using fully 3D reconstruction algorithms in order to avoid significant artifacts and a loss of quantitative accuracy. We developed and evaluated novel reconstruction algorithms for 3D DT, referred to as the estimation-combination (E-C) reconstruction algorithms, that effectively solve the (fully) 3D DT reconstruction problem by performing a series of 2D Radon transform inversions [20]. This greatly reduces the large computational load that is generally required by any other 3D DT reconstruction technique such as the 3D FBPP algorithm. This is vitally important for the development of computationally tractable 3D nonlinear algorithms that involve the recursive application of a 3D linear reconstruction algorithm. We also demonstrated that, in the presence of data noise, there is redundant information contained in the 3D DT data function that can be exploited by the 3D E-C algorithms to reduce the variance of the reconstructed image [19].

### 2.1.2 Development of minimum-scan reconstruction algorithms

In many applications of tomographic imaging it is desirable to minimize the angular range over which the measurement data are acquired. This reduces the time necessary to collect the measurement data, which can reduce artifacts due to patient motion. Furthermore, in certain situations it may not be experimentally possible to collect data over a complete  $2\pi$  range. We demonstrated that a minimal-scan data set acquired using view angles only in  $[0, \phi_{min}]$  contains all the information necessary to reconstruct exactly a 2D scattering object function, where  $\pi \leq \phi_{min} \leq 3\pi/2$  is a function of the measurement geometry. Based on this observation, we developed, investigated, and numerically implemented minimal-scan FBPP and E-C reconstruction algorithms for 2D DT that can exactly reconstruct the scattering object function from the minimal scan data set. *Prior to our work, all reconstruction algorithms for DT required a full  $2\pi$  worth of angular measurements to reconstruct an accurate image.* We numerically demonstrated that the minimal-scan E-C reconstruction algorithms were less susceptible to the effects of data noise and inconsistencies than were the minimal-scan FBPP reconstruction algorithms. We also generalized this work to 2D DT using the fan-beam geometry and revealed a novel relationship between the maximum scanning angle and achievable image resolution. This work may provide useful insights into the development of minimum-scan reconstruction algorithms for 3D DT that can be used for breast imaging [21].

## 2.2 Development of efficient nonlinear reconstruction algorithms

In certain situations of the breast imaging, the first-order Born or Rytov approximations may not be valid. Consequently, a linearized Helmholtz equation may not accurately describe the relationship between the measured scattered wavefield and the scattering object, and nonlinear algorithms are necessary for obtaining accurate images. We proposed to develop efficient nonlinear reconstruction algorithms for UDT.

### **2.2.1 Development of 2D efficient nonlinear reconstruction algorithms**

Previously we described our development and investigation of E-C reconstruction algorithms for linear DT. We have generalized these algorithms to the case where a forward scattering model includes multiple-scattering effects. Two forward scattering models were utilized that captured higher-order terms in the Born or Rytov perturbation series, and are therefore potentially useful for modeling ultrasound wave propagation in breast tissue [22, 23]. For each of the two forward scattering models, we developed families of nonlinear E-C reconstruction algorithms to solve the inverse problem [19]. The nonlinear E-C reconstruction algorithms operate by relating, in 2D Fourier space of the Radon transform, the  $n$ -th order perturbation of the measured data function to the  $n$ -th order perturbation of the scattering object function. The algorithms are recursive in the sense that calculation of the  $n$ -th order perturbation of the object function requires knowledge of the  $(n-1)$ -th order perturbation. The computational efficiency of the E-C algorithms is therefore very relevant to this problem. We also identified consistency conditions for the nonlinear imaging models employed by the two families of nonlinear E-C algorithms. For both imaging models, the consistency conditions for linear DT were contained as special cases.

### **2.2.2 Development of 3D efficient nonlinear reconstruction algorithms**

Although we have been largely successful in the theoretical development of computationally efficient nonlinear algorithms for 2D UDT, the applicability of such algorithms can be restrictive because the multi-scattering effect in the breast imaging is generally 3D in nature. Therefore, we have also investigated 3D nonlinear reconstruction algorithms. Our strategy for the development of 3D nonlinear reconstruction algorithms is similar to that for 2D nonlinear reconstruction discussed above. Specifically, we proposed to investigate the two mentioned forward models in 3D and to use the perturbation series for the inversion. The inversion of the solution at each perturbative order will be accomplished through the use of our developed linear 3D E-C algorithms for improving the computational efficiency. We are currently continuing the development of such 3D perturbative nonlinear algorithms.

## **2.3 Implementation and evaluation of the proposed algorithms**

We have implemented the proposed linear algorithms and nonlinear algorithms and evaluated them by use of computer simulated data and real data.

### **2.3.1 Implementation and evaluation of linear reconstruction algorithms**

We have implemented the linear E-C reconstruction algorithms and investigated their noise properties by using a large number of computer simulated data sets. Through our simulation studies, we have demonstrated that it is possible to achieve a bias-free reduction of the statistical variation in the reconstructed object function by utilizing complementary statistical

information inherent in the scattered data. (The use of an explicit smoothing operation generally introduces bias in the reconstructed scattering object function.) We have quantitatively demonstrated that the E-C algorithms are less susceptible to data noise and other finite sampling effects than are the corresponding FBPP algorithms. This result is consistent with the observation that the FBPP algorithms involve more complicated numerical operations (e.g., backpropagation) than do the E-C algorithms, which may amplify the propagation of noise and errors into the reconstructed image. Using simulated strongly scattering data, we have demonstrated that the E-C algorithms are less susceptible to modeling errors due to violation of first-order scattering approximations. These same results have been verified for the minimum-scan DT problem.

### **2.3.2 Implementation and evaluation of nonlinear reconstruction algorithms**

Using simulated strongly scattering data, we have started to numerically investigate nonlinear reconstruction algorithms for 2D DT. As described in Section 2.2.1, our nonlinear reconstruction algorithms utilize a forward scattering operator that assumes the validity of a higher-order Born or Rytov terms. An accurate numerical implementation of the forward scattering operator is critical for obtaining accurate reconstructions using our algorithms. In a preliminary study, we have encountered difficulty in achieving an accurate numerical implementation of this operator. The forward scattering models employed by our families of nonlinear algorithms involve an integration over a complex frequency variable, which is not computable in practice. Accordingly, numerical inaccuracies were introduced by truncating the limits of integration, which we observed to introduce a severe degradation in the reconstructed image quality. We are currently investigating methods for mitigating the effects of the integration truncation used by the forward scattering operator.

## **2.4 Development and evaluation of reconstruction algorithms for reflectivity tomography**

Reflectivity tomography has been applied to numerous biomedical and non-destructive test imaging problems [24–27]. It has a strong relationship to UDT and can be a potential useful technique for imaging the breast cancer. The task in reflectivity tomography is to reconstruct from the measured data a function describing the reflectivity distribution within the breast. It has been generally considered that accurate images can be reconstructed only from full scan data over  $2\pi$ . Recently, we have investigated and evaluated image reconstruction from minimum-scan data in reflectivity tomography. Using the so-called potato-peeler perspective that we developed, we showed that accurate images can be reconstructed from minimum-scan data in reflectivity tomography. We also performed quantitative studies by use of computer simulated data, and the results in such studies validated our theoretical results for image reconstruction in minimum-scan reflectivity tomography.

### 3 Key research accomplishments

- We have developed and evaluated computationally efficient 3D linear reconstruction algorithms that are more than 100 times faster than the conventional 3D FBPP algorithm.
- We have investigated, developed, and evaluated algorithms for image reconstruction from minimum-scan data in UDT with plane wave sources.
- We have investigated, developed, and evaluated algorithms for image reconstruction from full-scan and minimum-scan data in UDT with fan-beam wave sources.
- We have developed and evaluated computationally efficient 3D linear reconstruction algorithms for UDT with spherical wave sources.
- We have developed computationally efficient 2D nonlinear reconstruction algorithms for UDT with plane wave sources.
- We have investigated theoretically the development of computationally efficient nonlinear reconstruction algorithms for 3D UDT.
- We have developed computer codes that implement the proposed linear and nonlinear reconstruction algorithms.
- We have evaluated the developed linear and nonlinear reconstruction algorithms by use of computer simulated and experimental data.
- We have developed and evaluated reconstruction algorithms for short-scan reflectivity tomography.

### 4 Reportable outcomes

#### Peer-Reviewed Original Articles

1. M. Anastasio and X. Pan: Full- and minimal-scan reconstruction algorithms for fan-beam diffraction tomography, *Appl. Opt.*, **40**, 3334-3345, 2001.
2. X. Pan and M. Anastasio: On a limited-view reconstruction problem in wavefield tomography, *IEEE Trans. Med. Imaging.*, **21**, 413-416, 2002.
3. M. Anastasio and X. Pan: Numerically robust minimal-scan reconstruction algorithms for diffraction tomography via Radon transform inversion, *Int. J. Imag. Sys. Tech.*, (in press) 2002.
4. M. Anastasio and X. Pan: An improved reconstruction algorithm for 3D diffraction tomography with spheric-wave sources, *IEEE Trans. Biomed. Eng.*, (submitted), 2002.



5. X. Pan, Y. Zou, and M. Anastasio: Data redundancy and reduced-scan reconstruction algorithms in reflectivity tomography, *IEEE Trans. Image Processing*, (submitted), 2002.
6. X. Pan, Y. Zou, and M. Anastasio: Image reconstruction of reflectivity from short scan data, *CD Proc. of International Symposium on Biomedical Imaging*, Washington D. C., 2002.

#### **Ph.D. Thesis**

1. M. Anastasio: Development and analysis of image reconstruction algorithms in diffraction tomography, The University of Chicago, 2001.

#### **Peer-Reviewed Proceedings Articles**

1. X. Pan and M. Anastasio: Minimal-scan reconstruction algorithms for fan-beam diffraction tomography and their analogy to halfscan fan-beam CT, *IEEE Medical Imaging Conference Record (CD)*, 2001.
2. M. Anastasio and X. Pan: Development and evaluation of minimal-scan reconstruction algorithms for diffraction tomography, *Proc. SPIE*, (in press), 2001.

#### **Abstracts and Presentations**

1. X. Pan and M. Anastasio: Reconstruction algorithms in diffraction tomography, Advanced Light Source, Lawrence Berkeley National Laboratory, California, (Host: Dr. Malcolm Howells), October 29, 2001.
2. M. Anastasio, Y. Zou, and X. Pan: Reflectivity tomography using temporally truncated data, *The 2nd Joint Meeting of the IEEE Engineering in Medicine and Biology Society and Biomedical Engineering Society*, (submitted,) Houston, 2002.
3. Y. Zou, M. Anastasio, and X. Pan: Data truncation and the exterior problem in reflection-mode tomography, *IEEE Medical Imaging Conference*, (submitted,) Norfolk, 2002.

## **5 Conclusion**

Ultrasonic diffraction tomography is a potentially important technique for imaging of the breast cancer. In this project, we have investigated, developed, and evaluated computationally efficient and statistically optimal algorithms for accurate reconstruction of UDT images that may find applications in UDT imaging of breast cancer. In the last year, we have made contributions to UDT research, as summarized above. Our research on UDT have addressed numerous scientific and engineering problems involved in UDT image reconstruction. These results are necessary in making UDT a viable medical imaging technique for imaging breast cancer.

## References

- [1] A. Devaney. A filtered backpropagation algorithm for diffraction tomography. *Ultrasonic Imaging*, 4:336–350, 1982.
- [2] S. Pan and A. Kak. A computational study of reconstruction algorithms for diffraction tomography: Interpolation versus filtered backpropagation. *IEEE Transactions on Acoustics, Speech, and Signal Processing*, 31:1262–1275, 1983.
- [3] M. Kaveh, M. Soumekh, and J. Greenleaf. Signal processing for diffraction tomography. *IEEE Transactions on Sonics and Ultrasonics*, 31:230–239, 1984.
- [4] M. Andre, H. Janee, G. Otto, P. Martin, G. Otto, and B. Spivey. High-speed data acquisition in a diffraction tomography system employing large-scale toroidal arrays. *Int. J. Imaging Syst. Technol.*, 8:137–147, 1997.
- [5] R. Waag, A. Nachman, and T. Mast. New method and apparatus for imaging. In *Department of Defense Breast Cancer Research Program Meeting*, Washington, D.C., 1997.
- [6] M. Anastasio and X. Pan. Full- and minimal-scan reconstruction algorithms for fan-beam diffraction tomography. *Appl. Opt.*, 40, 2001.
- [7] D. Rouseff and R. Porter. Diffraction tomography and the stochastic inverse scattering problem. *Journal of the Acoustical Society of America*, 89:1599–1605, 1991.
- [8] G. Tsihrintzis and A. Devaney. Stochastic diffraction tomography: Theory and computer simulation. *Signal Processing*, 93:49–64, 1993.
- [9] X. Pan. A unified reconstruction theory for diffraction tomography with considerations of noise control. *Journal of the Optical Society of America*, 15:2312–2326, 1998.
- [10] F. Lin and M. Fiddy. Image estimation from scattered field data. *Int. J. Imag. Sys. Tech.*, 2:76–95, 1990.
- [11] R. G. Newton. Inverse scattering II. Three dimensions. *J. Math Phys.*, 21:1698–1715, 1981.
- [12] R. G. Newton. Inverse scattering II. Three dimensions, continued. *J. Math Phys.*, 22:2191–2200, 1981.
- [13] D. Colton and P. Monk. The inverse scattering problem for time harmonic acoustic waves in an inhomogeneous medium. *Q. J. Mech. Appl. Math.*, 41:97–125, 1988.
- [14] Y. Wang and W. C. Chew. Solution of large 2-D inhomogeneous scatterers for TM waves by fast recursive algorithm. *Micro. Opt. Tech. Lett.*, 4, 1991.

- [15] S. Johnson and M. Tracy. Inverse scattering solutions by a sinc basis, multiple source, moment method - Part I:theory. *Ultrasonic Imaging*, 5:361–375, 1983.
- [16] S. Johnson and M. Tracy. Inverse scattering solutions by a sinc basis, multiple source, moment method - Part II:numerical evaluations. *Ultrasonic Imaging*, 5:376–392, 1983.
- [17] M. Moghaddam and W. C. Chew. Study of some practical issues in inversion with the Born iterative method using time domain data. *IEEE Trans. Antennas Propag.*, 41:177–184, 1993.
- [18] W. Chew and Y. Wang. Reconstruction of two-dimensional permittivity distribution using the distorted Born iterative method. *IEEE Transactions on Medical Imaging*, 9:218–225, 1990.
- [19] M. Anastasio. Development and analysis of image reconstruction algorithms in diffraction tomography. Ph.D. Thesis, The University of Chicago, 2001.
- [20] M. Anastasio and X. Pan. Computationally efficient and statistically robust image reconstruction in 3D diffraction tomography. *J. Opt. Soc. Am.*, 17:391–400, 2000.
- [21] X. Pan and M. Anastasio. On a limited-view reconstruction problem in wavefield tomography. *IEEE Trans. Med. Imaging*, 21, 2002.
- [22] C. Lu, W. Chew, and G. Otto. Image reconstruction with acoustic measurement using distorted Born iterative method. *Ultrasonic Imaging*, 18:140–156, 1996.
- [23] G. A. Tsihrintzis and A. J. Devaney. Higher-order (nonlinear) diffraction tomography: Reconstruction algorithms and computer simulation.
- [24] S. Norton and M. Linzer. Ultrasonic reflectivity imaging in three dimensions: Exact inverse scattering solutions for plane, cylindrical, and spherical apertures. *J. Acous. Soc. Am.*, 67, 1980.
- [25] M. Moshfeghi. Ultrasound reflection-mode tomography using fan-shaped-beam insonification. *IEEE Transactions on Ultrasonics, Ferroelectrics and Frequency Control*, 33:299–314, 1986.
- [26] K. Dines and A. Goss. Computer ultrasonic reflection tomography. *IEEE Transactions on Ultrasonics, Ferroelectrics and Frequency Control*, 34:309–317, 1987.
- [27] J. Ylitalo, J. Kaovukangas, and J. Oksman. Ultrasonic reflection mode computed tomography through a skullbone. *IEEE Transactions on Biomedical Engineering*, 37:1059–1065, 1990.

## Appendix: Attached articles

# Full- and minimal-scan reconstruction algorithms for fan-beam diffraction tomography

Mark A. Anastasio and Xiaochuan Pan

Diffraction tomography (DT) is a tomographic inversion technique that reconstructs the spatially variant refractive-index distribution of a scattering object. In fan-beam DT, the interrogating radiation is not a plane wave but rather a cylindrical wave front emanating from a line source located a finite distance from the scattering object. We reveal and examine the redundant information that is inherent in the fan-beam DT data function. Such redundant information can be exploited to reduce the reconstructed image variance or, alternatively, to reduce the angular scanning requirements of the fan-beam DT experiment. We develop novel filtered backpropagation and estimate-combination reconstruction algorithms for full-scan and minimal-scan fan-beam DT. The full-scan algorithms utilize measurements taken over the angular range  $0 \leq \phi \leq 2\pi$ , whereas the minimal-scan reconstruction algorithms utilize only measurements taken over the angular range  $0 \leq \phi \leq \phi_{\min}$ , where  $\pi \leq \phi_{\min} \leq 3\pi/2$  is a specified function that describes the fan-beam geometry. We demonstrate that the full- and minimal-scan fan-beam algorithms are mathematically equivalent. An implementation of the algorithms and numerical results obtained with noiseless and noisy simulated data are presented. © 2001 Optical Society of America

OCIS codes: 100.3190, 100.3010, 100.6950.

## 1. Introduction

Diffraction tomography (DT) is an inversion scheme that can be used for obtaining the spatially variant refractive-index distribution of a scattering object. Applications of DT can be found in various scientific fields such as medical imaging,<sup>1,2</sup> nondestructive evaluation of materials,<sup>3,4</sup> and geophysics.<sup>5,6</sup> Unlike the x rays used in computed tomography (CT), the optical or acoustical wave fields employed in DT do not generally travel along straight lines, thus precluding the use of the geometrical optics approximation. Therefore a wide variety of techniques that are suitable for reconstruction of CT images cannot be used directly for reconstruction of diffraction tomographic images. CT can be viewed as a limiting case of DT, in which the frequency of the probing radiation tends toward infinity.

A vast majority of the algorithm development ef-

forts in DT have utilized the classic scanning geometry,<sup>7</sup> which assumes that the interrogating radiation is plane wave and the transmitted scattered wave field is measured in a plane (or in two dimensions, along a line) on the opposite side of the scattering object. This geometry is analogous to the parallel-beam geometry of x-ray CT. In many practical situations, however, the interrogating radiation may be not plane wave but rather produced by a line source located a finite distance from the scattering object. We refer to this configuration as the fan-beam geometry of DT,<sup>8</sup> which is somewhat analogous to the two-dimensional (2D) fan-beam geometry of CT.

The Born and Rytov approximations<sup>9</sup> are weak-scattering approximations that effectively linearize the inhomogeneous Helmholtz and Riccati equations, respectively. The relative merits of the Born and Rytov approximations in the context of DT have been widely explored in the literature.<sup>10,11</sup> Under weak-scattering conditions it is customary and useful in DT to invoke the Born or Rytov approximation that permits the derivation of the Fourier diffraction projection (FDP) theorem. The FDP theorem relates the one-dimensional (1D) Fourier transform of the measured scattered data to the 2D Fourier transform of the scattering object. For 2D DT employing plane-wave illumination and the classic scan configuration, Devaney<sup>7</sup> utilized the FDP theorem to develop the

M. A. Anastasio and X. Pan (x-pan@uchicago.edu) are with the Graduate Program in Medical Physics, Department of Radiology, University of Chicago, 5841 South Maryland Avenue, Chicago, Illinois 60637.

Received 10 October 2000; revised manuscript received 4 April 2001.

0003-6935/01/203334-12\$15.00/0

© 2001 Optical Society of America

well-known filtered backpropagation (FBPP) algorithm, which can be viewed as a generalization of the conventional filtered backprojection (FBPJ) algorithm of x-ray CT. Alternative families of plane-wave DT reconstruction algorithms, referred to as estimate-combination (E-C) algorithms and generalized FBPP algorithms, have been developed<sup>12</sup> and investigated.<sup>13,14</sup> The family of plane-wave E-C algorithms effectively operates by transforming (in 2D Fourier space) the DT problem into a 2D Radon transform problem that can be efficiently and stably inverted by use of the FBPJ algorithm. The family of plane-wave generalized FBPP algorithms reconstructs the image directly from the DT data function and includes the FBPP algorithm as a special member. Both the generalized FBPP and E-C algorithms generally require scattered data measured from view angles in  $[0, 2\pi)$  to perform an exact reconstruction of a complex-valued scattering object. Accordingly, we refer to these algorithms as being full-scan algorithms.

Previously we showed<sup>15</sup> that, in plane-wave DT that employs the 2D classic scanning geometry, a minimal-scan data set acquired by use of view angles only in  $[0, \phi_{\min} = 3\pi/2]$  contains all the information necessary for exact reconstruction of the scattering object function. As the frequency of the probing radiation tends toward infinity,  $\phi_{\min} \rightarrow \pi$ , which reflects the well-known fact that measurements corresponding to  $\phi \in [0, \pi]$  completely specify the 2D Radon transform. [Of course, compactly supported objects are mathematically specified by a sinogram  $p(\xi, \phi_0)$ , where  $\phi_0$  is contained in any open set  $[0, \epsilon)$ , but if  $p(\xi, \phi_0)$  is not continuously sampled this observation does not yield stable reconstruction algorithms.] We subsequently developed minimal-scan FBPP<sup>15</sup> and minimal-scan E-C<sup>16</sup> algorithms that were capable of reconstructing the scattering object function by use of the minimal-scan data set. Under the conditions of continuous sampling and in the absence of noise, we demonstrated<sup>16</sup> that the minimal-scan FBPP and E-C reconstruction algorithms were mathematically equivalent to the full-scan FBPP and E-C reconstruction algorithms, respectively.

Here we reveal and examine the redundant information that is inherent in the fan-beam DT data function. Such redundant information can be exploited to reduce the noise in the reconstructed image or, alternatively, to reduce the angular scanning requirements of the fan-beam DT experiment. We develop novel E-C and FBPP reconstruction algorithms for full-scan and minimal-scan fan-beam DT. We demonstrate that the minimal-scan algorithms, which utilize measurements taken over the angular range  $0 \leq \phi \leq \phi_{\min}$ , where  $\pi \leq \phi_{\min} \leq 3\pi/2$ , are mathematically equivalent to their full-scan counterparts that utilize measurements over the full angular range  $0 \leq \phi \leq 2\pi$ . An implementation of the algorithms and numerical results obtained with noiseless and with noisy simulated data are presented.

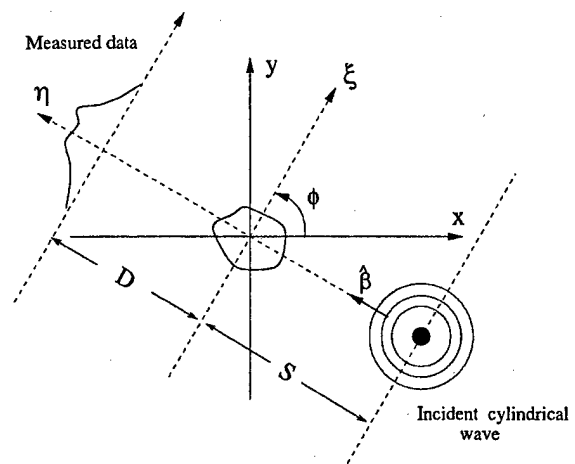


Fig. 1. Fan-beam scanning geometry of 2D DT. The interrogating cylindrical wave propagates along the  $\eta$  axis, and the scattered wave field is measured along the line  $\eta = l$ . We obtain full-scan and minimal-scan data sets by varying the measurement angle  $\phi$  between 0 and  $2\pi$  or between 0 and  $\phi_{\min}$  [see Eq. (29)], respectively. We assume that  $S$  and  $D$  are much larger than the transverse dimension of the scattering object.

## 2. Background

Here we briefly review the geometry and approximations that are traditionally employed in fan-beam DT, as described in the pioneering work of Devaney.<sup>8</sup> A table of the acronyms used in this manuscript is included in Appendix A.

### A. Fan-Beam Diffraction Tomography

The classic scanning configuration of fan-beam DT is shown in Fig. 1. The fixed coordinate system  $(x, y)$ , the rotated coordinate system  $(\xi, \eta)$ , and the usual polar coordinates  $(r, \theta)$  are related by  $x = r \cos \theta$ ,  $y = r \sin \theta$ ,  $\xi = x \cos \phi + y \sin \phi = r \cos(\phi - \theta)$ , and  $\eta = -x \sin \phi + y \cos \phi = -r \sin(\phi - \theta)$ . The scattering object is illuminated by a monochromatic cylindrical-wave source located at the position  $\eta = -S$  on the  $\eta$  axis, emitting a wave field of the form

$$u_i(\xi, \phi) = U_0 \frac{\exp(j2\pi\nu_0|\mathbf{r} - S\hat{\beta}|)}{|\mathbf{r} - S\hat{\beta}|} = U_0 \frac{\exp\{j2\pi\nu_0[\xi^2 + (S + D)^2]^{1/2}\}}{[\xi^2 + (S + D)^2]^{1/2}}, \quad (1)$$

where  $U_0$  is the complex amplitude,  $k = 2\pi\nu_0$  is the wave number,  $\hat{\beta}$  is a unit vector pointing along the positive  $\eta$  axis, and  $D$  is the distance of the detector surface from the center of rotation. The incident wave field  $u_i(\xi, \phi)$  could represent a pressure field in acoustical applications or a scalar electromagnetic field in optical applications, for example. From measurements of the scattered wave field obtained along the  $\xi$  axis oriented at a measurement angle  $\phi$  at a distance  $\eta = D$  from the origin, one seeks to reconstruct the scattering object function  $a(\mathbf{r})$ . The underlying physical property of the scattering object that is mapped in DT is the refractive-index distri-

bution  $n(\mathbf{r})$ , which is related to the scattering object function by the equation  $a(\mathbf{r}) = n^2(\mathbf{r}) - 1$ .

Let  $u(\xi, \phi)$  denote the measured total wave field along the line  $\eta = D$ , as shown in Fig. 1. The scattered data are given by

$$u_s(\xi, \phi) = u(\xi, \phi) - u_i(\xi, \phi), \quad (2)$$

which can be treated as a measurable data function because  $u(\xi, \phi)$  and  $u_i(\xi, \phi)$  can be measured. Therefore we can introduce a modified data function  $M(v_m, \phi)$ , which is given by

$$M(v_m, \phi) = \frac{\chi}{\pi v_0^2} v' \exp[-j2\pi(v' - v_0)D] \times \mathcal{F}_{v_m} \left\{ \frac{u_s(\xi, \phi)}{u_i(\xi, \phi)} \right\}, \quad (3)$$

where

$$\mathcal{F}_{v_m} \{h(\xi)\} = (1/2\pi) \int_{-\infty}^{\infty} h(\xi) \exp(-j2\pi v_m \xi) d\xi,$$

$$\chi = \sqrt{\frac{S}{S+D}}, \quad (4)$$

$$v' = \sqrt{v_0^2 - \frac{v_m^2}{\chi^2}}. \quad (5)$$

#### B. Fan-Beam Fourier Diffraction Projection Theorem

In plane-wave DT, the FDP theorem<sup>17</sup> relates the modified data function to the 2D Fourier transform of the scattering object and can be viewed as a generalization of the Fourier slice theorem of conventional x-ray CT. The FDP theorem is valid under conditions of weak scattering and plane-wave illumination. To establish the FDP theorem for the fan-beam DT geometry it is necessary to assume the weak-scattering approximation and the so-called paraxial approximation,<sup>8</sup> which is a well-known approximation in the optics literature. The paraxial approximation requires that both  $S$  and  $D$  be much larger than the dimension size of the scattering object. This amounts to requiring that the largest angle subtended by the object when the object is viewed from either the source or the measurement location be much smaller than a radian.

Under the Born and paraxial approximations, Devaney derived the fan-beam FDP theorem,<sup>8</sup> which is given by

$$M(v_m, \phi) = \int_{-\infty}^{\infty} \int_{-\infty}^{\infty} a(\mathbf{r}) \exp \left\{ -j2\pi \left[ \frac{v_m}{\chi^2} \xi - (v' - v_0)\eta \right] \right\} d\mathbf{r} \quad |v_m| \leq \chi v_0, \\ = 0 \quad |v_m| > \chi v_0. \quad (6)$$

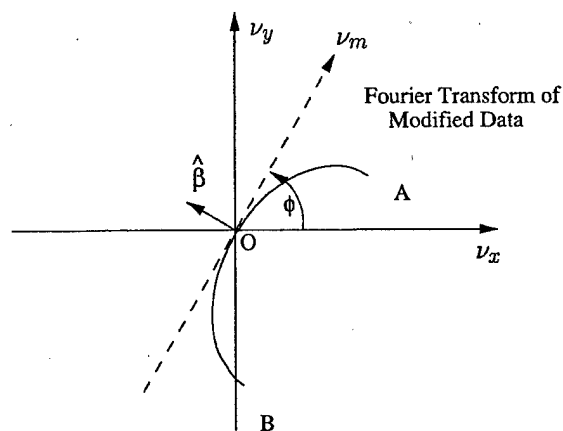


Fig. 2. The fan-beam FDP theorem states that  $M(v_m, \phi)$  is equal to the 2D Fourier transform of  $a(\mathbf{r})$  along the semielliptic arc  $AOB$  that has semi-axes equal to  $v_0$  and  $v_0/\chi$ .

As displayed in Fig. 2, Eq. (6) states that the modified data function,  $M(v_m, \phi)$ , is equal to a semielliptical slice, oriented at angle  $\phi$ , through the 2D Fourier transform of the object function  $a(\mathbf{r})$ . One can also derive the FDP theorem by employing the Rytov approximation instead of the Born approximation. In this case, Eq. (6) remains unchanged and only Eq. (3) needs to be appropriately redefined.<sup>8</sup>

### 3. Full-Scan Reconstruction Algorithms for Fan-Beam Diffraction Tomography

First, we present families of full-scan FBPP and E-C reconstruction algorithms for fan-beam DT. These fan-beam algorithms are novel and contain the previously developed families of plane-wave FBPP and E-C algorithms as limiting cases. They will be generalized to the minimal-scan situation in Section 4 below.

#### A. Fan-Beam Full-Scan Estimate-Combination Algorithms

The Radon transform<sup>18</sup> of the scattering object function  $a(r, \theta)$  is defined as

$$p(\xi, \phi_0) = \int_{-\infty}^{\infty} \int_{-\infty}^{\infty} a(r, \theta) \delta[\xi - r \cos(\phi_0 - \theta)] dr, \quad (7)$$

where  $\phi_0$  is the projection angle,  $\xi = r \cos(\phi_0 - \theta)$ , and  $\eta = -r \sin(\phi_0 - \theta)$ . The 2D Fourier transform of  $p(\xi, \phi_0)$  is defined as [strictly speaking,  $P_k(v_a)$  is the com-

bination of the 1D Fourier transform with respect to  $\nu_a$  and a 1D Fourier series expansion with respect to  $\phi_0$  of the Radon transform]

$$P_k(\nu_a) = \frac{1}{2\pi} \int_0^{2\pi} \int_{-\infty}^{\infty} p(\xi, \phi_0) \times \exp[-j2\pi\nu_a\xi - jk\phi_0] d\xi d\phi_0, \quad (8)$$

where  $\nu_a$  is the spatial frequency with respect to  $\xi$  and the integer  $k$  is the angular frequency index with respect to  $\phi_0$ . It is well known that  $a(r, \theta)$  can readily be reconstructed exactly from its Radon transform  $p(\xi, \phi_0)$  [or, equivalently,  $P_k(\nu_a)$ ] by use of a wide variety of computationally efficient and numerically stable reconstruction algorithms such as the FBPJ algorithm. Therefore the task of image reconstruction in fan-beam DT is tantamount to the task of estimating  $P_k(\nu_a)$ . Furthermore, because  $P_k(\nu_a)$  for  $\nu_a \geq 0$  contains full knowledge of the Radon transform, one needs to estimate  $P_k(\nu_a)$  from the measured scattered data only for  $\nu_a \geq 0$ .

Comparison of Eqs. (9) and (11) yields that, for  $|\nu_m| \leq \chi\nu_0$ ,

$$P_k(\nu_a) = \gamma(\nu_m/\chi^2)^k M_k(\nu_m), \quad (13)$$

provided that

$$\nu_a^2 = \left(\frac{\nu_m}{\chi^2}\right)^2 + \left\{ \left[ \nu_0^2 - \left(\frac{\nu_m}{\chi}\right)^2 \right]^{1/2} - \nu_0 \right\}^2. \quad (14)$$

From Eq. (14) we see that  $\nu_a$  is real (that is,  $0 \leq \nu_a \leq \nu_0 \sqrt{1 + 1/\chi^2}$ ) only for  $|\nu_m| \leq \chi\nu_0$ .

In the absence of data noise or inconsistencies, one can use Eq. (13) to obtain  $P_k(\nu_a)$  exactly from  $M_k(\nu_m)$ , which can readily be obtained from the modified data function. In the presence of data noise or inconsistencies, one can use Eq. (13) to obtain an estimate of  $P_k(\nu_a)$ . For any given  $0 \leq \nu_a \leq \nu_0 \sqrt{1 + 1/\chi^2}$ , we show in Appendix B that four different roots  $\nu_{mi}$ ,  $i = 1, 2, 3, 4$ , satisfy Eq. (14). However, only two of these four roots correspond to real-valued frequencies, which are given by

$$\nu_{m1} = -\nu_{m2} = \nu_m = \nu_a \left( 1 - \frac{\nu_a^2}{4\nu_0^2} \right)^{1/2} \left( \frac{\chi^4}{\frac{1}{2}[1 - (1 - \chi^2)(\nu_a^2/2\nu_0^2)] + [1 - \chi^2(1 - \chi^2)(\nu_a^2/\nu_0^2)]^{1/2}} \right)^{1/2} \quad (15)$$

From Eqs. (7) and (8) it can be shown<sup>19</sup> that

$$P_k(\nu_a) = (-j)^k \int_{\theta=0}^{2\pi} \int_{r=0}^{\infty} a(\mathbf{r}) \times \exp(-jk\theta) J_k(2\pi\nu_a r) r dr d\theta, \quad (9)$$

where  $J_k$  indicates the  $k$ th-order Bessel function of the first kind. Because  $M(\nu_m, \phi)$  is a periodic function of  $\phi$ , it can be expanded into a Fourier series with expansion coefficients given by

$$M_k(\nu_m) = \frac{1}{2\pi} \int_0^{2\pi} M(\nu_m, \phi) \exp(-jk\phi) d\phi. \quad (10)$$

Substituting Eq. (6) into Eq. (10), noting that  $\xi = r \cos(\phi - \theta)$  and  $\eta = -r \sin(\phi - \theta)$ , and carrying out the integration over angle  $\phi$  (Ref. 19) yield

$$M_k(\nu_m) = (-j)^k \gamma(\nu_m')^{-k} \int_{r=0}^{\infty} \int_{\theta=0}^{2\pi} a(\mathbf{r}) \exp(-jk\theta) J_k(2\pi r \sqrt{\nu_m'^2 - \nu_\mu^2}) r dr d\theta \quad |\nu_m| \leq \chi\nu_0, \\ = 0 \quad |\nu_m| > \chi\nu_0, \quad (11)$$

where  $\nu_m' = \nu_m/\chi^2$ ,  $\nu_\mu = j(\nu' - \nu_0)$ , and

$$\gamma(\nu_m') = \frac{\sqrt{\nu_m'^2 - \nu_\mu^2}}{\nu_m' + \nu_\mu}. \quad (12)$$

In the plane-wave case there are only two roots,<sup>12</sup> which one can obtain from Eq. (15) by letting  $\chi = 1$ .

Therefore, for a given  $0 \leq \nu_a \leq \nu_0(1 + 1/\chi^2)^{1/2}$ , one can obtain two estimates of  $P_k(\nu_a)$  from knowledge of  $M_k(\nu_m)$  at  $\nu_{m1}$  and  $\nu_{m2}$ , namely,

$$P_k(\nu_a) = \left[ \gamma\left(\frac{\nu_{m1}}{\chi^2}\right) \right]^k M_k(\nu_{m1}) = \left[ \gamma\left(\frac{\nu_m}{\chi^2}\right) \right]^k M_k(\nu_m), \quad (16)$$

$$P_k(\nu_a) = \left[ \gamma\left(\frac{\nu_{m2}}{\chi^2}\right) \right]^k M_k(\nu_{m2}) \\ = (-1)^k \left[ \gamma\left(\frac{\nu_m}{\chi^2}\right) \right]^{-k} M_k(-\nu_m). \quad (17)$$

In establishing Eq. (17) we used the property  $\gamma(-\nu_m') = -\gamma(\nu_m')^{-1}$ . It can readily be shown that, as the

incident wave becomes planar (i.e., as  $\chi \rightarrow 1$ ), the above results become the results in Ref. 12 for the plane-wave case.

In the absence of noise, Eqs. (16) and (17) yield identical (and exact) values of  $P_k(\nu_a)$ . In the presence of data noise (or other inconsistencies), the two

estimates of  $P_k(v_a)$  are distinct, suggesting that it may be beneficial to combine the two estimates linearly<sup>12</sup> to form a final estimate of  $P_k(v_a)$  as

$$P_k(v_a) = \omega_k(v_m)[\gamma^k M_k(v_m)] + [1 - \omega_k(v_m)][(-1)^k \gamma^{-k} M_k(-v_m)], \quad (18)$$

where  $\omega_k(v_m)$  is a combination coefficient that dictates how Eqs. (16) and (17) are combined. This strategy of linear combination has been demonstrated to be useful in reducing the noise in the reconstructed image.<sup>12-14</sup> Because each selection of  $\omega_k(v_m)$  gives rise to a particular final estimate  $P_k(v_a)$ , Eq. (18) can be interpreted as an estimation method for obtaining  $P_k(v_a)$  (or, equivalently, the Radon transform). Because  $\omega_k(v_m)$  may be any complex-valued function of  $v_m$  and  $k$ , Eq. (18), in effect, provides infinite families of estimation methods. From the estimate  $P_k(v_a)$  (i.e., the Radon transform), one can subsequently reconstruct the image  $a(r)$  by use of the FBPP algorithm. For simplicity, the use of Eq. (18) to estimate  $P_k(v_a)$  coupled with the 2D FBPP algorithm to reconstruct  $a(r)$  is referred to as a fan-beam full-scan E-C reconstruction algorithm. As  $S \rightarrow \infty$ , we observe that  $\chi \rightarrow 1$  and that the fan-beam full-scan E-C reconstruction algorithms reduce to the plane-wave full-scan E-C reconstruction algorithms developed previously.<sup>12</sup>

#### B. Fan-Beam Full-Scan Filtered Backpropagation Algorithms

The fan-beam full-scan E-C algorithms discussed above first estimate  $P_k(v_a)$  (i.e., the Radon transform) from the modified data function  $M_k(v_m)$  and subsequently reconstruct the image by inverting the estimated Radon transform. Below, we develop algorithms that reconstruct images directly from the modified data function. Using Eq. (9), one can directly express the object function in terms of the estimate  $P_k(v_a)$  as

$$a(r) = 2\pi \sum_{k=-\infty}^{\infty} j^k \int_{v_a=0}^{\infty} P_k(v_a) \times \exp(jk\theta) J_k(2\pi v_a r) v_a dv_a. \quad (19)$$

Substituting Eq. (18) into Eq. (19) yields

$$a(r) = 2\pi \sum_{k=-\infty}^{\infty} j^k \exp(jk\theta) \int_{v_a=0}^{\infty} \sqrt{1+1/\chi^2} \{ \omega_k(v_m) \gamma^k M_k(v_m) + [1 - \omega_k(v_m)] (-1)^k \gamma^{-k} M_k(-v_m) \} J_k(2\pi v_a r) v_a dv_a. \quad (20)$$

Using the relationship between  $v_a$  and  $v_m$  in Eq. (14), one can show that, for  $0 \leq v_a \leq v_0 \sqrt{1+1/\chi^2}$ ,

$$v_a dv_a = \frac{v_m' dv_m'}{v'} [(1 - \chi^2) v' + \chi^2 v_0]. \quad (21)$$

Substituting this result into Eq. (20), and noting that  $v_m' = v_m/\chi^2$ , yields

$$a(r) = \pi \sum_{k=-\infty}^{\infty} j^k \exp(jk\theta) \int_{v_m=0}^{\chi v_0} \frac{v_m}{\chi^4 v'} [(1 - \chi^2) v' + \chi^2 v_0] \{ \omega_k(v_m) \gamma^k M_k(v_m) + [1 - \omega_k(v_m)] \times (-1)^k \gamma^{-k} M_k(-v_m) \} \times J_k[2\pi(v_m'^2 - v_\mu'^2 r)^{1/2}] dv_m. \quad (22)$$

To reduce Eq. (22) to the form of the FBPP algorithm, we assume that  $\omega_k(v_m) + \omega_k(-v_m) = 1$ . Using the integral identities<sup>12</sup>

$$(\pm)^k j^k \gamma(v_m')^{\pm k} \exp(jk\theta) J_k[2\pi(v_m'^2 - v_\mu'^2 r)^{1/2}] = \frac{1}{2\pi} \int_0^{2\pi} \exp\left[jk\phi \pm j2\pi v_m \frac{\xi}{\chi^2} + 2\pi v_\mu \eta\right] d\phi \quad (23)$$

and defining

$$M^{(\omega)}(v_m, \phi) = \sum_{k=-\infty}^{\infty} \exp(jk\phi) \omega_k(v_m) M_k(v_m) \quad (24)$$

yield for Eq. (22)

$$a(r) = \frac{1}{2} \int_0^{2\pi} \int_{-\chi v_0}^{\chi v_0} \frac{|v_m|}{\chi^4 v'} [(1 - \chi^2) v' + \chi^2 v_0] M^{(\omega)}(v_m, \phi) \times \exp\left[j2\pi v_m \frac{\xi}{\chi^2} + 2\pi v_\mu \eta\right] d\phi dv_m. \quad (25)$$

Equation (25) describes a family of fan-beam full-scan FBPP algorithms [indexed by the choice of  $\omega_k(v_m)$ ], which becomes the family of FBPP algorithms for plane-wave full-scan DT<sup>12</sup> when  $\chi \rightarrow 1$ . In particular, when  $\omega_k(v_m) = 1/2$ , Eq. (25) corresponds to the fan-beam FBPP algorithm suggested by Devaney.<sup>8</sup> Because the derivation of the family of fan-beam full-scan FBPP algorithms was based on the family of fan-beam full-scan E-C algorithms [Eq. (20)], the E-C and FBPP algorithms are mathematically equivalent. However, as will be demonstrated below, these FBPP and E-C algorithms respond differently to data noise and other experimental errors.

#### 4. Minimal-Scan Reconstruction Algorithms for Fan-Beam Diffraction Tomography

As discussed above, the redundant information contained in the scattered data can be employed for reducing the image noise. Such information can also be used for reducing the angular scanning requirements in a DT experiment.

##### A. Consistency Conditions and the Fan-Beam Data Space

According to the fan-beam FDP theorem in Eq. (6), the modified data function  $M(v_m, \phi)$  satisfies the consistency condition

$$M(v_m, \phi) = M(-v_m, \phi + \pi - 2\alpha), \quad (26)$$



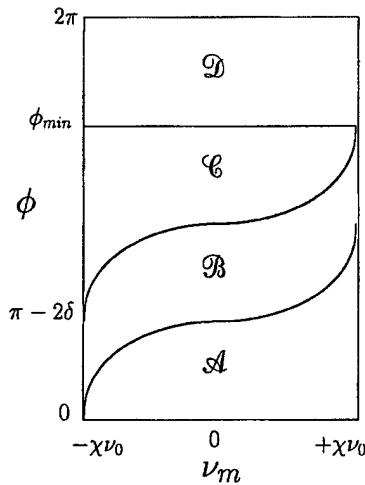


Fig. 3. Complete data space  $\mathcal{W} = \mathcal{A} \cup \mathcal{B} \cup \mathcal{C} \cup \mathcal{D}$  contains data from the view angles in  $[0, 2\pi]$ . Subset  $\mathcal{M} = \mathcal{A} \cup \mathcal{B} \cup \mathcal{C}$  obtained from the view angles in  $[0, \phi_{\min}]$  is called the minimal-complete data set. The minimal-complete data set contains all the information necessary for exact reconstruction of the scattering object function.

where

$$\sin \alpha = \text{sgn}(\nu_m) \left[ \frac{(\nu' - \nu_0)^2}{(\nu_m^2/\chi^2) + (\nu' - \nu_0)^2} \right]^{1/2}. \quad (27)$$

Let  $\mathcal{W} = [|\nu_m| \leq \chi\nu_0, 0 \leq \phi \leq 2\pi]$  denote the complete (or full-scan) data set. As shown in Fig. 3,  $\mathcal{W}$  can be divided into the four subspaces,  $\mathcal{A}$ ,  $\mathcal{B}$ ,  $\mathcal{C}$ , and  $\mathcal{D}$ , where

$$\begin{aligned} \mathcal{A} &= [|\nu_m| \leq \chi\nu_0, 0 \leq \phi \leq 2\alpha + 2\delta], \\ \mathcal{B} &= [|\nu_m| \leq \chi\nu_0, 2\alpha + 2\delta \leq \phi \leq \pi + 2\alpha], \\ \mathcal{C} &= [|\nu_m| \leq \chi\nu_0, \pi + 2\alpha \leq \phi \leq \phi_{\min}], \\ \mathcal{D} &= [|\nu_m| \leq \chi\nu_0, \phi_{\min} \leq \phi \leq 2\pi], \end{aligned}$$

where

$$\sin \delta = \frac{1}{(1 + 1/\chi^2)^{1/2}}, \quad \phi_{\min} = \pi + 2\delta. \quad (28)$$

Using Eqs. (26) and (27), one can verify that information in subspace  $\mathcal{C}$  is identical to that in subspace  $\mathcal{A}$  and that information in subspace  $\mathcal{B}$  is identical to that in subspace  $\mathcal{D}$ . As shown in Fig. 3, because the boundaries between the subspaces are generally functions of  $\nu_m$  and  $\phi$  and because each horizontal line in  $\mathcal{W}$  corresponds to a measurement acquired at a particular view angle, the information in subspace  $\mathcal{B}$  cannot in practice be determined independently of that in subspace  $\mathcal{C}$  and vice versa. We therefore refer to the union,  $\mathcal{M} = \mathcal{A} \cup \mathcal{B} \cup \mathcal{C} = [|\nu_m| \leq \chi\nu_0, 0 \leq \phi \leq \phi_{\min}]$ , as the minimal-complete data set. A plot of  $\phi_{\min}$  versus  $\chi$  is shown in Fig. 4. As  $\chi \rightarrow 1$ ,  $\phi_{\min} \rightarrow 3\pi/2$ , and  $\mathcal{M}$  reduces to the minimal-complete data set proposed previously for plane-wave DT.<sup>15</sup> However, for  $\chi < 1$ ,  $\phi_{\min} < 3\pi/2$ , which indicates that the

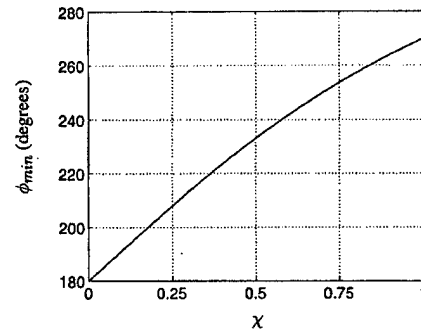


Fig. 4. Plot of  $\phi_{\min}$  versus  $\chi$  reveals that, in fan-beam DT, the required angular scanning range is less than  $270^\circ$ .

angular scanning requirements of fan-beam DT are less restrictive than for plane-wave DT.

Figure 5 clearly demonstrates that the minimal-complete data set contains all the information required for an exact reconstruction. According to the FDP theorem, the segment  $AOB$  corresponds to a semielliptical slice through the 2D Fourier transform of  $a(\mathbf{r})$ , which can be obtained from the modified data function  $M(\nu_m, \phi)$ . The Fourier space coverages produced by the segments  $OA$  and  $OB$  as  $\phi$  varies from 0 to  $\phi_{\min}$  are shown in Figs. 5(a) and 5(b), respectively.

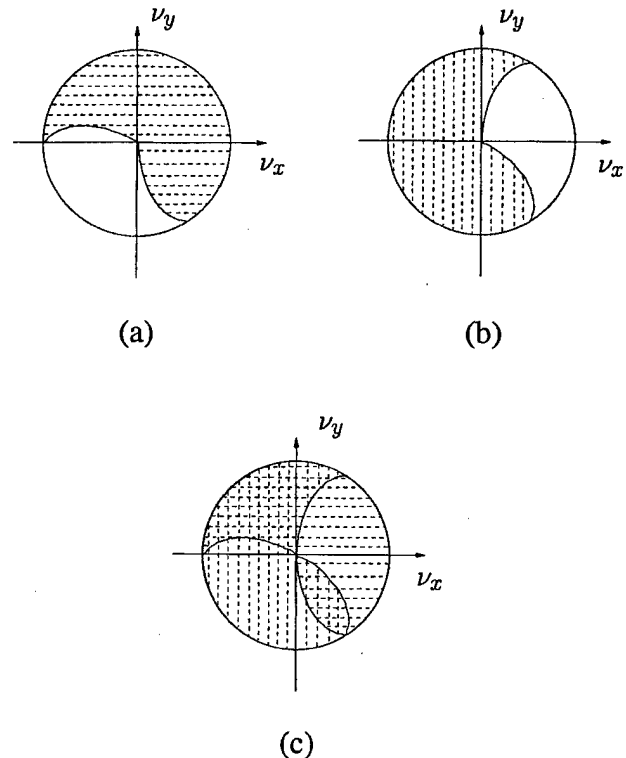


Fig. 5. As  $\phi$  varies from 0 to  $\phi_{\min}$ , the two segments  $OA$  and  $OB$  (Fig. 2) yield two incomplete coverages of the 2D Fourier space of the object function, which are shown in (a) and (b), respectively. Superimposing the two incomplete coverages in (a) and (b), one obtains a complete coverage, as shown in (c), of the 2D Fourier space of the object function.

tively. It can be observed that each of these two coverages alone provides only an incomplete coverage of the 2D Fourier space of  $a(\mathbf{r})$ . However, one can superimpose these two incomplete coverages in Figs. 5(a) and 5(b) to obtain complete coverage of the 2D Fourier space of  $a(\mathbf{r})$ , as shown in Fig. 5(c).

The redundant information contained in subspaces  $\mathcal{A}$  and  $\mathcal{C}$  of the minimal-complete data set needs to be normalized properly before or during the reconstruction procedure. Let  $M^{(m)}(\nu_m, \phi)$  denote the minimal scan data, where  $M^{(m)}(\nu_m, \phi) = M(\nu_m, \phi)$  for  $0 \leq \phi \leq \phi_{\min}$  and  $M^{(m)}(\nu_m, \phi) = 0$  for  $\phi_{\min} < \phi < 2\pi$ . Consider a weighted data set  $M'(\nu_m, \phi)$ , defined as

$$M'(\nu_m, \phi) = w(\nu_m, \phi) M^{(m)}(\nu_m, \phi), \quad (29)$$

where  $w(\nu_m, \phi)$  can be a function of  $\nu_m$  and  $\phi$  that satisfies

$$w(\nu_m, \phi) + w(-\nu_m, \phi + \pi - 2\alpha) = 1 \quad (30a)$$

in complete data space  $\mathcal{W}$ ,

$$w(\nu_m, \phi) = 1 \quad (30b)$$

in subspace  $\mathcal{B}$ , and

$$w(\nu_m, \phi) = 0 \quad (30c)$$

in subspace  $\mathcal{D}$ . One can choose different  $w(\nu_m, \phi)$  in subspaces  $\mathcal{A}$  and  $\mathcal{C}$  as long as these  $w(\nu_m, \phi)$  satisfy Eq. 30(a). In the numerical examples that follow, we used the explicit form for  $w(\nu_m, \phi)$  given by Eq. (38). We can now readily obtain minimal-scan reconstruction algorithms for fan-beam DT.

#### B. Fan-Beam Minimal-Scan Estimate-Combination Algorithms

Because of Eq. 30(c), Eq. (29) can also be rewritten as

$$M'(\nu_m, \phi) = w(\nu_m, \phi) M(\nu_m, \phi). \quad (31)$$

Using Eqs. (26) and (30a), one can verify that

$$M(\nu_m, \phi) = M'(\nu_m, \phi) + M'(-\nu_m, \phi + \pi - 2\alpha). \quad (32)$$

Using Eq. (32) in Eq. (10), one obtains

$$M_k(\nu_m) = [M'_k(\nu_m) + (-1)^k \gamma^{-2k} M'_k(-\nu_m)], \quad (33)$$

where

$$M'_k(\nu_m) = (1/2\pi) \int_0^{2\pi} \exp(-jk\phi) M'(\nu_m, \phi) d\phi.$$

Multiplying both sides of Eq. (33) by  $\gamma^k$  and noting Eq. (16), we conclude that, for  $|\nu_m| \leq \chi\nu_0$ ,

$$P_k(\nu_a) = [\gamma^k M'_k(\nu_m) + (-1)^k \gamma^{-k} M'_k(-\nu_m)], \quad (34)$$

where  $\nu_a$  and  $\nu_m$  are related by Eq. (14). A fan-beam minimal-scan E-C algorithm is formed by use of Eq. (34) to estimate the Radon transform from the minimal-complete data set acquired at measurement angles  $0 \leq \phi \leq \phi_{\min}$  and the FBPJ algorithm to reconstruct the final image. One can form different

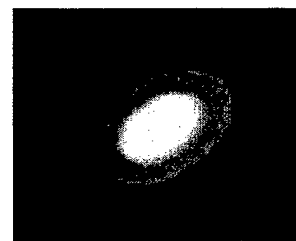


Fig. 6. The numerical phantom used in the simulation studies comprised two concentric ellipses. The fan-beam FDP theorem was used to calculate analytically the simulated scattered field data from the phantom.

fan-beam minimal-scan E-C algorithms by specifying different choices for  $w(\nu_m, \phi)$  in Eq. (31) that satisfy Eqs. (30).

#### C. Fan-Beam Minimal-Scan Filtered Backpropagation Algorithms

Using Eq. (34) in Eq. (19) and using the strategy outlined in Subsection 3.B, we can also develop fan-beam minimal-scan FBPP algorithms that can reconstruct the object function directly from the weighted minimal-complete data set that is given by

$$a(\mathbf{r}) = \int_0^{\phi_{\min}} \int_{-\chi\nu_0}^{\chi\nu_0} \frac{|\nu_m|}{\chi^4 \nu'} [(1 - \chi^2) \nu' + \chi^2 \nu_0] M'(\nu_m, \phi) \times \exp \left[ j2\pi \nu_m \frac{\xi}{\chi^2} + 2\pi \nu_\mu \eta \right] d\phi d\nu_m, \quad (35)$$

where  $\phi_{\min}$  is a function of  $\chi$  as stated in Eq. (28). One can form different fan-beam minimal-scan FBPP algorithms by specifying different choices for  $w(\nu_m, \phi)$  in Eq. (31) that satisfy Eqs. (30). When  $\chi = 1$ , the fan-beam minimal-scan FBPP algorithms reduce to the plane-wave minimal-scan FBPP algorithms derived previously.<sup>15</sup>

### 5. Numerical Results

We numerically investigated the fan-beam full- and minimal-scan reconstruction algorithms, using simulated noiseless and noisy data.

#### A. Data and Noise Model

We employed the numerical phantom composed of two concentric ellipses, as displayed in Fig. 6. The values of the scattering object function that correspond to the outer and inner ellipses are 0.0005 and 0.0001, respectively. We chose a fan-beam geometry specified by  $\chi = 0.8$ , but our observations below hold for arbitrary  $\chi$ . The FDP theorem was employed to calculate analytically the modified data function  $M(\nu_m, \phi)$  that by means of Eq. (3) determined the scattered field data  $u_s(\xi, \phi)$ . Therefore our simulations were designed to demonstrate the performance of the reconstruction algorithms under the condition that the Born and paraxial approximations are valid. The evaluation of the performance of the algorithms when the Born and paraxial approximations are not valid<sup>10,11,20</sup> remains a topic for future study. The

discrete complete data set comprised 128 equally spaced measurement angles in  $[0, 2\pi)$ . The discrete minimal-complete data set comprised 92 equally spaced measurement angles in  $[0, 4.49]$  (or, equivalently,  $[0, 257.3^\circ]$ ). In this way, both data sets had the same angular sampling increment,  $\Delta\phi = 2\pi/128 \approx 4.49/92$ . The data function  $M(v_m, \phi)$  contained 129 evenly spaced samples in  $[-\chi v_0, \chi v_0]$ .

To simulate the effects of data noise, we treated the scattered data  $u_s(\xi, \phi)$  as a complex stochastic process with a real and an imaginary component, denoted  $u_s^{(r)}(\xi, \phi)$  and  $u_s^{(i)}(\xi, \phi)$ , respectively. (Here, boldface type for  $u$  and  $a$  denotes a random variable.) Let  $u_s^{(r)} = u_s^{(r)} + \Delta u_s^{(r)}$  and  $u_s^{(i)} = u_s^{(i)} + \Delta u_s^{(i)}$ , where  $u_s^{(r)}$  and  $u_s^{(i)}$  are the means of  $u_s^{(r)}$  and  $u_s^{(i)}$ , respectively. The statistics of the deviates  $\Delta u_s^{(r)}$  and  $\Delta u_s^{(i)}$  are described by the circular Gaussian model,

$$p(\Delta u_s^{(r)}, \Delta u_s^{(i)}) = \frac{1}{2\pi\sigma_r\sigma_i} \times \exp\left[-\frac{1}{2}\left(\frac{\Delta u_s^{(r)2}}{\sigma_r^2} + \frac{\Delta u_s^{(i)2}}{\sigma_i^2}\right)\right], \quad (36)$$

where  $\sigma_r^2$  and  $\sigma_i^2$  are the variances of  $\Delta u_s^{(r)}(\xi, \phi)$  and  $\Delta u_s^{(i)}(\xi, \phi)$ , respectively.

To study the noise properties of the reconstructed images quantitatively, we generated  $N = 250$  noisy complete and minimal-complete data sets by using the noise model in Eq. (36) with  $\sigma_r = \sigma_i = 0.05$ . We used the fan-beam full-scan and minimal-scan E-C and FBPP algorithms to reconstruct sets of 250 noisy images from these noisy data sets. The matrix size of the reconstructed images was  $128 \times 128$  pixels, and the wavelength of the incident radiation was equal to 2 pixels. The local image variance was calculated empirically from the  $N$  sets of reconstructed images as

$$\text{var}[\mathbf{a}(\mathbf{r})] = \frac{1}{N-1} \left\{ \sum_{i=1}^N \mathbf{a}_i(\mathbf{r})^2 - \frac{1}{N} \left[ \sum_{i=1}^N \mathbf{a}_i(\mathbf{r}) \right]^2 \right\}, \quad (37)$$

where  $\mathbf{a}_i(\mathbf{r})$  is the  $i$ th image obtained by use of the reconstruction algorithm under investigation.

## B. Implementation Details

### 1. E-C Algorithms

From the uniformly sampled values of the scattered field  $u_s(\xi, \phi)$ ,  $M_k(v_m)$  can be determined at uniformly spaced values of  $v_m$ . However, because of the non-linear relationship [Eq. (14)] between  $v_a$  and  $v_m$ , the uniformly spaced values of  $v_m$  at which  $M_k(v_m)$  is sampled do not generally correspond to the uniformly spaced values of  $v_a$  at which one needs to evaluate  $P_k(v_a)$  (to utilize the fast Fourier transform in the FBPJ algorithm). For each of 65 evenly spaced values of  $v_a$  spanning the range  $0 \leq v_a \leq v_0\sqrt{1 + 1/\chi^2}$ , we used linear interpolation to determine the values

of  $M_k(v_m = \sqrt{v_a^2 + v_\mu^2})$  and  $M_k(v_m = -\sqrt{v_a^2 + v_\mu^2})$  from the sampled values of  $M_k(v_m)$  and  $M_k(-v_m)$ , which we subsequently used in Eq. (18) to evaluate  $P_k(v_a)$ . For each value of  $k$ , zero-padding interpolation was employed to increase the sampling density along the  $v_m$  axis of  $M_k(v_m)$  by a factor of 3 to increase the accuracy of the interpolation operation. We employed the consistency condition  $P_k(v_a) = (-1)^k P_k(-v_a)$  to obtain the 64 samples of  $P_k(v_a)$  for  $v_a$  spanning the range  $-v_0\sqrt{1 + 1/\chi^2} \leq v_a < 0$ . In our implementation of the FBPJ algorithm, an unapodized ramp filter was used. The interpolation necessary for aligning the backprojected data onto a  $128 \times 128$  pixel discrete image matrix was performed by bilinear interpolation. When  $M_k(v_m)$  is replaced by  $M_k'(v_m)$ , and Eq. (34) is employed in place of Eq. (18), the above paragraph also describes our implementation of the fan-beam minimal-scan E-C algorithm.

### 2. FBPP Algorithms

In the full-scan and minimal-scan FBPP algorithms, at each measurement angle  $\phi$ ,  $M(v_m, \phi)$  or  $M'(v_m, \phi)$ , respectively, was multiplied by the depth-dependent filter  $(|v_m|/\chi^4 v')[(1 - \chi^2)v' + \chi^2 v_0] \exp[2\pi v_\mu \eta]$  for each of 128 discrete values of  $\eta$ . For each value of  $\eta$ , the filtered data were zero padded to ensure that the pixel size of the reconstructed image matched the pixel size of the images reconstructed by use of the full- and minimal-scan E-C algorithms. The interpolation necessary for aligning the backpropagated data onto a  $128 \times 128$  pixel discrete image matrix was performed by bilinear interpolation.

The fan-beam minimal-scan E-C and minimal-scan FBPP algorithms utilized the weight function  $w(v_m, \phi)$  [see Eq. (29)] given by

$$w(v_m, \phi) = \begin{cases} \sin^2 \left[ \frac{\pi}{4} \frac{\phi}{(\pi/4) - \alpha} \right] & 0 \leq \phi \leq 2\delta + 2\alpha \\ 1 & 2\delta + 2\alpha \leq \phi \leq \pi + 2\alpha \\ \sin^2 \left[ \frac{\pi}{4} \frac{(3\pi/2) - \phi}{(\pi/4) + \alpha} \right] & \pi + 2\alpha \leq \phi \leq \phi_{\min} \\ 0 & \phi_{\min} \leq \phi \leq 2\pi \end{cases} \quad (38)$$

### C. Results

From the simulated noiseless complete and minimal-complete data sets we reconstructed the phantom, using the full- and minimal-scan fan-beam reconstruction algorithms. Figures 7(a) and 7(b) show the images obtained from the full-scan and the minimal-scan E-C reconstruction algorithms, respectively. The full-scan E-C algorithm was specified by  $\omega_k(v_m) = 1/2$  in Eq. (18). The images appear identical, as is consistent with our assertion that the full- and minimal-scan E-C algorithms are mathematically equivalent in the absence of noise or other errors. Figures 7(c) and 7(d) show the images obtained by use of the full-scan and the minimal-scan

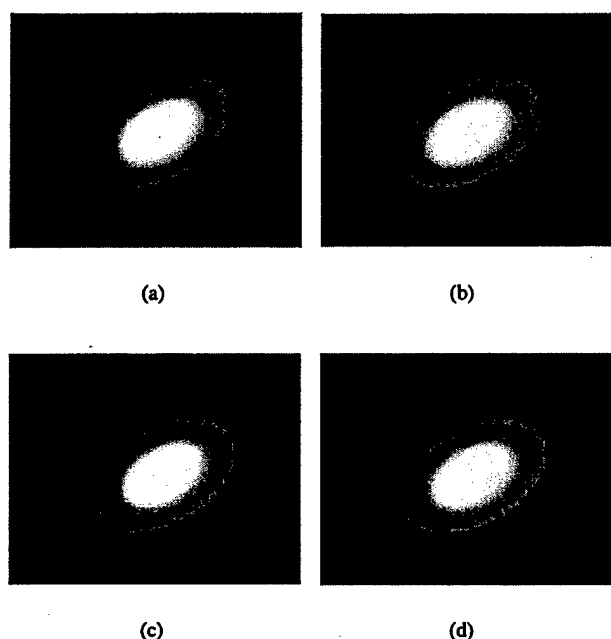


Fig. 7. Images reconstructed from noiseless data by use of (a) full-scan E-C, (b) minimal-scan E-C, (c) full-scan FBPP, and (d) minimal-scan FBPP reconstruction algorithms.

FBPP reconstruction algorithms, respectively. Again, the images appear identical, consistent with our assertion that the full- and minimal-scan FBPP algorithms are mathematically equivalent in the absence of noise or other errors. As expected, it is also observed that the images reconstructed with the full- and minimal-scan E-C algorithms [Figs. 7(a) and 7(b)] are identical to the images reconstructed with the full- and minimal-scan FBPP algorithms [Figs. 7(c) and 7(d)].

Using one of the simulated noisy complete and minimal-complete data sets, we again reconstructed the phantom, using the full- and minimal-scan E-C and FBPP reconstruction algorithms. Figures 8(a) and 8(b) show the images obtained by use of the full-scan and the minimal-scan E-C reconstruction algorithms, respectively. The images no longer appear identical, and the image reconstructed with the full-scan E-C algorithm appears less noisy than the image reconstructed with the minimal-scan E-C algorithm. Figures 8(c) and 8(d) show the images obtained by use of the full-scan and the minimal-scan FBPP reconstruction algorithms, respectively. Similarly, the image reconstructed with the full-scan FBPP algorithm appears less noisy than the image reconstructed with the minimal-scan FBPP algorithm.

The observation that the full-scan algorithms generate cleaner-looking images than do the minimal-scan algorithms is not surprising and can be qualitatively understood by examination of ways in which the redundant information inherent in the DT data function is utilized. The full-scan FBPP and E-C algorithms [with  $\omega_k(v_m) \neq 0, 1$ ] effectively use the redundant information to reconstruct two sepa-

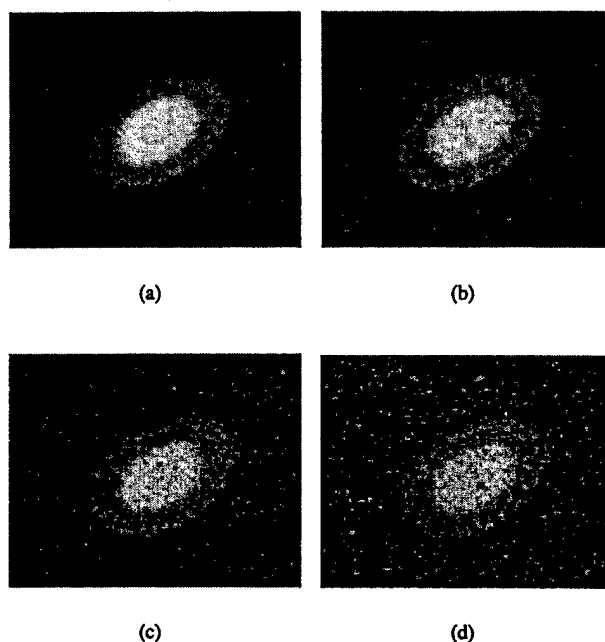


Fig. 8. Images reconstructed from noisy data by use of (a) full-scan E-C, (b) minimal-scan E-C, (c) full-scan FBPP, and (d) minimal-scan FBPP reconstruction algorithms. The noisy data were generated with  $\sigma_r = \sigma_t = 0.05$  in Eq. (36).

rate images that are averaged to form the final image. It has been quantitatively demonstrated that this effective averaging operation can result in an unbiased reduction of the reconstructed image variance.<sup>12,14</sup> The minimal-scan algorithms, however, utilize part of the redundant information that is inherent in the data function to reduce the angular range over which measurements are required for the reconstruction. The redundant information not used for this purpose can be used to reduce the image variance of the reconstructed image. Specifically, the complementary information contained in subspaces  $\mathcal{A}$  and  $\mathcal{C}$  of Fig. 3 is weighted, as described by Eq. (29), and is subsequently combined during the reconstruction procedure. However, unlike the full-scan algorithms, the minimal-scan algorithms cannot further reduce the reconstructed image variance by exploiting the fact that subspaces  $\mathcal{B}$  and  $\mathcal{D}$  contain redundant information.

Although the full- and minimal-scan E-C algorithms are mathematically equivalent to the full- and minimal-scan FBPP algorithms, we observed from Fig. 8 that the E-C and FBPP algorithms respond differently to noise that is present in a discrete data set. To confirm this observation quantitatively, we calculated the local image variances of images reconstructed, using the different methods. Figure 9(a) is a plot of the local variance obtained from the minimal-scan FBPP reconstructed images divided by the local variance obtained from the minimal-scan E-C reconstructed images. Clearly, the ratio of the variances is everywhere greater than 1, quantitatively demonstrating that the minimal-scan E-C reconstruction algorithms are less susceptible to the

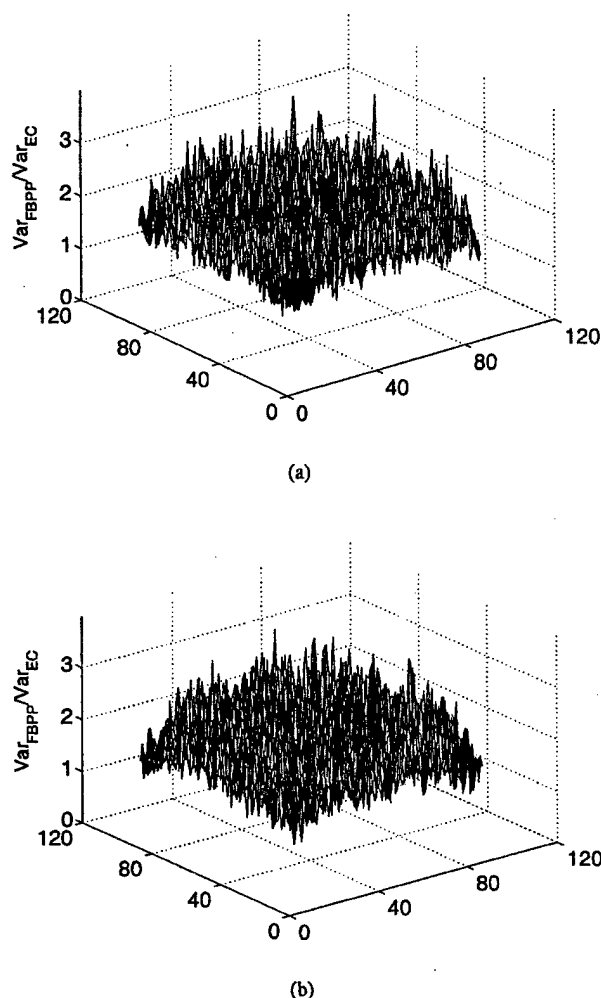


Fig. 9. (a) Plot of the local variance obtained from the full-scan FBPP reconstructed images divided by the local variance obtained from full-scan E-C reconstructed images. (b) Plot of the local variance obtained from the minimal-scan FBPP reconstructed images divided by the local variance obtained from minimal-scan E-C reconstructed images. In both the full- and the minimal-scan cases, the E-C algorithms did a better job of suppressing data noise than did the FBPP algorithms.

effects of data noise than are the minimal-scan FBPP reconstruction algorithms. Figure 9(b) is a plot of the local variance obtained from the full-scan FBPP reconstructed images divided by the local variance obtained from the full-scan E-C reconstructed images. The ratio of the variances is everywhere greater than 1, quantitatively demonstrating that the full-scan E-C reconstruction algorithms are less susceptible to the effects of data noise than are the full-scan FBPP reconstruction algorithms. These results are consistent with those obtained previously for full- and minimal-scan DT utilizing plane-wave illumination.<sup>16,21</sup>

## 6. Summary

In this study, we revealed and examined the redundant information that is inherent in the fan-beam DT

data function. Such information can be exploited to reduce the reconstructed image variance or alternatively to reduce the angular scanning requirements of the fan-beam DT experiment. We developed novel full-scan and minimal-scan E-C and FBPP reconstruction algorithms for fan-beam DT. The family of fan-beam full-scan E-C algorithms operates by transforming (in 2D Fourier space) the fan-beam DT problem into a 2D parallel-beam x-ray CT problem, which can be efficiently and stably inverted by use of the FBPJ algorithm. The family of fan-beam full-scan FBPP algorithms operates directly on the modified data function to reconstruct the image and contains the fan-beam FBPP algorithm suggested by Devaney<sup>8</sup> as a special member. Different members of the families of full-scan E-C and FBPP algorithms are specified by different choices of the combination coefficient  $\omega_k(v_m)$ , which controls ways in which the redundant information in the data function is combined. Reconstruction algorithms that correspond to different choices of  $\omega_k(v_m)$  will in general respond differently to the effect of noise and discrete sampling.<sup>12</sup>

The fan-beam minimal-scan E-C and FBPP algorithms were developed from the concept of the minimal-complete data set. The minimal-complete data set, which is acquired by use of view angles only in  $[0, \phi_{\min}]$  where  $\pi \leq \phi_{\min} \leq 3\pi/2$ , contains all the information necessary for exactly reconstructing the scattering object function. The fan-beam minimal-scan E-C and FBPP algorithms utilize a weighting function  $w(v_m, \phi)$  to normalize appropriately the partially redundant information inherent in the minimal-complete data set. Accordingly, one can form different fan-beam minimal-scan E-C and FBPP algorithms by specifying different choices for this weighting function. Reconstruction algorithms that correspond to different choices of  $w(v_m, \phi)$  will in general respond differently to the effect of noise and discrete sampling.<sup>15</sup> It can be readily verified that, under the conditions of continuous sampling and in the absence of noise, the minimal-scan E-C and FBPP algorithms are exact and mathematically equivalent to their full-scan counterparts that utilize measurements over the angular range  $0 \leq \phi \leq 2\pi$ .

An implementation of the fan-beam full-scan and minimal-scan algorithms has been presented, along with numerical results obtained with noiseless and with noisy simulated data. It was observed that the full-scan algorithms did a better job of suppressing data noise than did their minimal-scan counterparts. We quantitatively demonstrated that the full- and minimal-scan E-C algorithms are less susceptible to data noise and to finite sampling effects than are the full- and minimal-scan FBPP algorithms, respectively. This result is consistent with the observation that the FBPP-based algorithms involve more-complicated numerical operations than do the E-C-based algorithms, which may amplify the propagation of noise and errors into the reconstructed image.

We have assumed a 2D imaging model in this

study. Therefore the developed reconstruction algorithms may be useful for applications in which out-

It can readily be verified that the four roots of Eq. (A2) are given by

$$\nu_{m1} = -\nu_{m2} = \nu_a \left( 1 - \frac{\nu_a^2}{4\nu_0^2} \right)^{1/2} \left( \frac{\chi^4}{\frac{1}{2}\{1 - (1 - \chi^2)(\nu_a^2/2\nu_0^2) + [1 - \chi^2(1 - \chi^2)(\nu_a^2/\nu_0^2)]^{1/2}\}} \right)^{1/2}, \quad (\text{A3})$$

$$\nu_{m3} = -\nu_{m4} = \nu_a \left( 1 - \frac{\nu_a^2}{4\nu_0^2} \right)^{1/2} \left( \frac{\chi^4}{\frac{1}{2}\{1 - (1 - \chi^2)(\nu_a^2/2\nu_0^2) - [1 - \chi^2(1 - \chi^2)(\nu_a^2/\nu_0^2)]^{1/2}\}} \right)^{1/2}. \quad (\text{A4})$$

of-plane scattering is not significant. The full-scan E-C and FBPP reconstruction algorithms can be generalized readily to address the three-dimensional DT problem by use of spherical-wave sources and planar measurement surfaces. It remains unclear whether numerically stable versions of the minimal-scan E-C and FBPP reconstruction algorithms can be developed for three-dimensional imaging geometries.

Here we have developed linear reconstruction algorithms for fan-beam DT. It was not our intent to address the limitations of the Born or Rytov<sup>10,11</sup> weak-scattering approximation. The developed full- and minimal-scan algorithms will, however, provide a natural framework for the incorporation of higher-order scattering perturbation approximations<sup>22-24</sup> into the algorithms. It remains to be determined whether minimal-scan reconstruction algorithms can be developed without use of the paraxial approximation.<sup>25</sup> We intend to report on the theoretical development and numerical analysis of these problems in a forthcoming publication.

#### Appendix A: Acronyms Used

CT	Computed tomography
DT	Diffraction tomography
E-C reconstruction algorithm	Estimate-combination reconstruction algorithm
FBPJ reconstruction algorithm	Filtered backprojection reconstruction algorithm
FBPP reconstruction algorithm	Filtered backpropagation reconstruction algorithm
FDP theorem	Fourier diffraction projection theorem

#### Appendix B: Relationships between $\nu_m$ and $\nu_a$

From Eq. (14) we know that

$$\nu_a^2 = \left( \frac{\nu_m}{\chi^2} \right)^2 + \left\{ \left[ \nu_0^2 - \left( \frac{\nu_m}{\chi} \right)^2 \right]^{1/2} - \nu_0 \right\}^2. \quad (\text{A1})$$

For a given  $\nu_a$  that satisfies  $0 \leq \nu_a \leq \nu_0 \sqrt{1 + 1/\chi^2}$ , we would like to find the values of  $\nu_m$  that satisfy Eq. (A1). This is equivalent to solving for the roots of the fourth-order equation:

$$(1 - \chi^2)^2 \left( \frac{\nu_m}{\chi^2} \right)^4 + [4\nu_0^2 - 2(1 - \chi^2)\nu_a^2] \left( \frac{\nu_m}{\chi^2} \right)^2 + \nu_a^2(\nu_a^2 - 4\nu_0^2) = 0. \quad (\text{A2})$$

Because when  $0 \leq \nu_a \leq \nu_0 \sqrt{1 + 1/\chi^2}$

$$1 - (1 - \chi^2) \frac{\nu_a^2}{2\nu_0^2} < \left[ 1 - \chi^2(1 - \chi^2) \frac{\nu_a^2}{\nu_0^2} \right]^{1/2}, \quad (\text{A5})$$

we observe that the roots  $\nu_{m3}$  and  $\nu_{m4}$  are complex valued and therefore are not physically meaningful. As expected, when  $\chi \rightarrow 1$ , Eq. (A3) reduces to the known result<sup>12</sup> for plane-wave DT given by

$$\nu_{m1} = -\nu_{m2} = \nu_a \left( 1 - \frac{\nu_a^2}{4\nu_0^2} \right)^{1/2}. \quad (\text{A6})$$

This research was supported in part by National Institutes of Health grants R01 CA70449 and R01 CA85593 and U.S. Department of Defense grant DAMD17-01-1-0502.

#### References

1. M. P. Andre, P. J. Martin, G. P. Otto, L. K. Olson, T. K. Barrett, B. A. Apivey, and D. A. Palmer, "A new consideration of diffraction computed tomography for breast imaging," *Acoust. Imaging* **21**, 379-390 (1995).
2. L. Gelius, I. Johansen, N. Sponheim, and J. Stamnes, "Diffraction tomography applications in medicine and seismics," in *NATO Advanced Workshop on Inverse Problems in Scattering and Imaging* (Adam Hilger, New York, 1991), pp. 268-292.
3. R. Mueller, M. Kaveh, and G. Wade, "Reconstructive tomography and applications to ultrasonics," *Proc. IEEE* **67**, 567-587 (1979).
4. G. Kino, "Acoustic imaging for nondestructive evaluation," *Proc. IEEE* **67**, 510-525 (1979).
5. A. Devaney, "Geophysical diffraction tomography," *IEEE Trans. Geosci. Remote Sens.* **22**, 3-13 (1984).
6. E. Robinson, "Image reconstruction in exploration geophysics," *IEEE Trans. Sonics Ultrason.* **31**, 259-270 (1984).
7. A. Devaney, "A filtered backpropagation algorithm for diffraction tomography," *Ultrason. Imaging* **4**, 336-350 (1982).
8. A. Devaney, "Generalized projection-slice theorem for fan-beam diffraction tomography," *Ultrason. Imaging* **7**, 264-275 (1985).
9. A. Ishimaru, *Wave Propagation and Scattering in Random Media* (Academic, New York, 1978).
10. B. Chen and J. Stamnes, "Validity of diffraction tomography based on the first-Born and first-Rytov approximations," *Appl. Opt.* **37**, 2996-3006 (1998).
11. M. Slaney, A. C. Kak, and L. Larsen, "Limitations of imaging with first-order diffraction tomography," *IEEE Trans. Microwave Theory Tech.* **32**, 860-874 (1984).
12. X. Pan, "Unified reconstruction theory for diffraction tomog-

- raphy with considerations of noise control," *J. Opt. Soc. Am. A* **15**, 2312–2326 (1998).
13. M. Anastasio and X. Pan, "A new reconstruction algorithm for reflection-mode diffraction tomography," *IEEE Trans. Image Process.* **9**, 1262–1271 (2000).
  14. M. Anastasio and X. Pan, "Investigation of the noise properties of a new class of reconstruction methods in diffraction tomography," *Int. J. Imaging Syst. Technol.* **10**, 437–446 (2000).
  15. X. Pan and M. Anastasio, "Minimal-scan filtered backpropagation algorithms for diffraction tomography," *J. Opt. Soc. Am. A* **16**, 2896–2903 (1999).
  16. M. Anastasio and X. Pan, "Efficient and numerically robust minimal-scan reconstruction algorithms for diffraction tomography," submitted to *IEEE Trans. Image Process.*
  17. E. Wolf, "Three-dimensional structure determination of semi-transparent objects from holographic data," *Opt. Commun.* **1**, 153–156 (1969).
  18. H. H. Barrett, "The Radon transform and its applications," in *Progress in Optics*, E. Wolf, ed. (North-Holland, Amsterdam, 1984), Vol. 21, pp. 219–286.
  19. C. E. Metz and X. Pan, "A unified analysis of exact methods of inverting the 2-D exponential Radon transform, with implications for noise control in SPECT," *IEEE Trans. Med. Imag.* **14**, 643–658 (1995).
  20. M. Azimi and A. Kak, "Distortion in diffraction tomography caused by multiple scattering," *IEEE Trans. Med. Imag.* **2**, 176–195 (1983).
  21. M. Anastasio, M. Kupinski, and X. Pan, "Noise properties of reconstructed images in ultrasound diffraction tomography," *IEEE Trans. Nucl. Sci.* **45**, 2216–2223 (1998).
  22. Z.-Q. Lu and Y.-Y. Zhang, "Acoustical tomography based on the second-order Born transform perturbation approximation," *IEEE Trans. Ultrason. Ferroelectrics Freq. Control* **43**, 296–302 (1996).
  23. G. Tsihrintzis and A. Devaney, "Higher-order (nonlinear) diffraction tomography: reconstruction algorithms and computer simulation," *IEEE Trans. Image Process.* **9**, 1560–1572 (2000).
  24. G. Tsihrintzis and A. Devaney, "Higher order (nonlinear) diffraction tomography: inversion of the Rytov series," *IEEE Trans. Inf. Theory* **46**, 1748–1761 (2000).
  25. A. Devaney and G. Beylkin, "Diffraction tomography using arbitrary transmitter and receiver surfaces," *Ultrason. Imaging* **6**, 181–193 (1984).

# Correspondence

## On a Limited-View Reconstruction Problem in Diffraction Tomography

Xiaochuan Pan\* and Mark A. Anastasio

**Abstract**—Diffraction tomography (DT) is an inversion technique that reconstructs the refractive index distribution of a scattering object. We previously demonstrated that by exploiting the redundant information in the DT data, the scattering object could be exactly reconstructed using measurements taken over the angular range  $[0, \phi_{\min}]$ , where  $\pi < \phi_{\min} \leq 3\pi/2$ . In this paper, we reveal a relationship between the maximum scanning angle and image resolution when a filtered backpropagation (FBPP) reconstruction algorithm is employed for image reconstruction. Based on this observation, we develop short-scan FBPP algorithms that reconstruct a low-pass filtered scattering object from measurements acquired over the angular range  $[0, \Phi^c]$ , where  $\Phi^c < \phi_{\min}$ .

**Index Terms**—Diffraction tomography, limited-view tomography, wave-field inversion techniques.

### I. INTRODUCTION

In diffraction tomography (DT), a semi-transparent scattering object is interrogated using a diffracting optical or acoustical wavefield and the scattered wavefield around the object is measured and used to reconstruct the (low-pass filtered) refractive index distribution of the scattering object. The principles of DT have been extensively utilized for developing optical and acoustic tomographic imaging systems. Recently, interest in DT within the optical imaging community has increased because of its potential application to the diffuse-photon density wave tomography [1]–[3].

It was shown previously [4], [5] that, in two-dimensional (2-D) DT employing plane-wave or cylindrical-wave sources and the classical scanning geometry, one can reconstruct the scattering object from a minimal-scan data set comprised of measurements acquired over the angular range  $[0, \phi_{\min}]$ , where  $\pi < \phi_{\min} \leq 3\pi/2$  is specified by the measurement geometry. In this paper, we reveal a relationship between image resolution and maximum scan angle, based upon which short-scan algorithms can be designed for reconstructing a low-pass filtered scattering object from measurements acquired over the angular range  $[0, \Phi^c]$ , where  $\Phi^c < \phi_{\min}$ . When the scattering object is sufficiently bandlimited, it can be exactly reconstructed from the limited-view measurements in  $[0, \Phi^c]$ . We present numerical examples that confirm our theoretical assertions.

### II. BACKGROUND

Consider the classical scanning geometry of DT with a cylindrical wave source, as shown in Fig. 1. Let  $(x, y)$  and  $(r, \theta)$  denote the fixed Cartesian and polar coordinate systems and

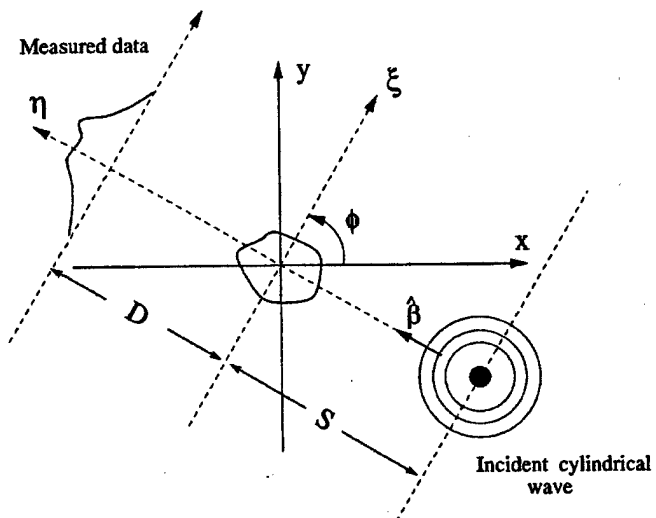


Fig. 1. The fan-beam scanning geometry of 2-D DT. The interrogating cylindrical wave propagates along the  $\eta$  axis and the scattered wave field is measured along the line  $\eta = 1$ .  $S$  (or  $D$ ) denotes the distance between the source (or the detector) and the center of rotation.

$(\xi, \eta)$  the rotated coordinate system. These systems are related by  $x = r\cos\theta$ ,  $y = r\sin\theta$ ,  $\xi = x\cos\phi + y\sin\phi = r\cos(\phi - \theta)$ , and  $\eta = -x\sin\phi + y\cos\phi = -r\sin(\phi - \theta)$ . The scattering object, which is embedded in a lossless and homogeneous background medium, is illuminated by a monochromatic cylindrical-wave  $u_i(\xi, \phi)$  with complex amplitude  $U_0$  and wavenumber  $k = 2\pi\nu_0$ , generated by a line source located at the position  $\eta = -S$  on the  $\eta$  axis. From measurements of the scattered wavefield on the  $\xi$  axis at different view angles  $\phi$ , one seeks to reconstruct the scattering object function  $a(\vec{r})$ , which is related to the refractive index distribution  $n(\vec{r})$  within the scattering object by  $a(\vec{r}) = n^2(\vec{r}) - 1$ .

Let  $u(\xi, \phi)$  and  $u_s(\xi, \phi) = u(\xi, \phi) - u_i(\xi, \phi)$  denote the total and scattered wavefields measured along the line  $\eta = D$  oriented at angle  $\phi$ , as shown in Fig. 1. For the sake of convenience, we introduce a modified data function  $M(\nu_m, \phi)$  that can be obtained readily from the scattered wavefield and is defined as

$$M(\nu_m, \phi) = \frac{\chi}{\pi\nu_0^2} \nu' \exp[-j2\pi(\nu' - \nu_0)D] \mathcal{F}_{\nu_m} \left\{ \frac{u_s(\xi, \phi)}{u_i(\xi, \phi)} \right\} \quad (1)$$

where  $\chi = \sqrt{S/(S+D)}$ ,  $\nu' = \sqrt{\nu_0^2 - \nu_m^2/\chi^2}$ , and  $\mathcal{F}_{\nu_m}\{h(\xi)\} = 1/(2\pi) \int_{-\infty}^{\infty} h(\xi) e^{-j2\pi\nu_m\xi} d\xi$ . The special case of plane-wave illumination ( $S \rightarrow \infty$ ) corresponds to  $\chi = 1$ . Under the Born and paraxial approximations, Devaney derived the fan-beam Fourier diffraction projection (FDP) theorem [6], which relates  $a(\vec{r})$  to the modified data function by

$$M(\nu_m, \phi) = \int_{-\infty}^{\infty} \int_{-\infty}^{\infty} a(\vec{r}) \cdot \exp \left\{ -j2\pi \left[ \frac{\nu_m}{\chi^2} \xi - (\nu' - \nu_0) \eta \right] \right\} d\vec{r},$$

$$\text{if } |\nu_m| \leq \chi\nu_0$$

$$= 0 \quad \text{if } |\nu_m| > \chi\nu_0. \quad (2)$$

Manuscript received April 24, 2001; revised February 14, 2002. The Associate Editor responsible for coordinating the review of this paper and recommending its publication was M. W. Vannier. Asterisk indicates corresponding author.

\*X. Pan is with the Graduate Program in Medical Physics, Department of Radiology, The University of Chicago, 5841 S. Maryland Ave., Chicago, IL 60637 USA (e-mail: x-pan@uchicago.edu).

M. A. Anastasio is with the Pritzker Institute of Medical Engineering, Illinois Institute of Technology, Chicago, IL 60616 USA.

Publisher Item Identifier S 0278-0062(02)04683-9.



The FDP theorem can also be derived by employing the Rytov approximation. In this case, (2) remains unchanged and only (1) needs to be appropriately redefined [6]. When  $\phi$  is varied from 0 to  $2\pi$ , the FDP theorem specifies a circular disk of (double) coverage centered at the origin with radius  $\nu_0 \sqrt{1 + 1/\chi^2}$  in the 2-D Fourier space of  $a(\vec{r})$ . Conventional full-scan reconstruction algorithms, such as the well known filtered backpropagation (FBPP) algorithm [7], utilize this Fourier space coverage for reconstructing  $a(\vec{r})$ . We will refer to such a (low-pass filtered) reconstructed  $a(\vec{r})$  as the "exact" image.

According to the fan-beam FDP theorem in (2), the modified data function  $M(\nu_m, \phi)$  satisfies the consistency condition [4]

$$M(\nu_m, \phi) = M(-\nu_m, \phi + \pi - 2\alpha) \quad (3)$$

where  $\sin \alpha = \text{sgn}(\nu_m) [((\nu' - \nu_0)^2 / (\nu_m^2 / \chi^2) + (\nu' - \nu_0)^2)]^{1/2}$ . Using (3), one can show [4], [5] that the minimal-scan data acquired in the angular range  $[0, \phi_{\min}]$  specifies a circular disk (with radius  $\nu_0 \sqrt{1 + 1/\chi^2}$ ) of coverage in the Fourier space of  $a(\vec{r})$ , where

$$\phi_{\min} = \pi + 2\delta \quad \text{and} \quad \sin \delta = \frac{1}{\sqrt{1 + \frac{1}{\chi^2}}}. \quad (4)$$

### III. A LIMITED-VIEW RECONSTRUCTION PROBLEM FOR 2-D DT

We focus now on a limited-view problem, in which data are acquired only over the angular range  $[0, \Phi^c]$ , where  $\pi < \Phi^c < \phi_{\min}$ . In this situation, it is well known that the exact image cannot, in general, be reconstructed [8]. However, we demonstrate that algorithms can be developed for reconstructing a low-pass filtered approximation of the exact image. Consider a scattering object  $a^c(\vec{r})$  whose 2-D Fourier transform  $A^c(\vec{\nu})$  is bandlimited to a disk of radius  $R_c$  centered at the origin, where

$$R_c(\nu_c) = \left[ \left( \frac{\nu_c}{\chi^2} \right)^2 + \left[ \sqrt{\nu_0^2 - \left( \frac{\nu_c}{\chi} \right)^2} - \nu_0 \right]^2 \right]^{1/2} \quad (5)$$

and  $0 \leq \nu_c \leq \chi\nu_0$ . Then, according to the fan-beam FDP theorem in (4), the modified data function  $M(\nu_m, \phi)$  is nonzero only for  $|\nu_m| \leq \nu_c$ . The data space  $\mathcal{W}_c = [|\nu_m| \leq \nu_c, 0 \leq \phi \leq 2\pi]$ , in which the modified data function  $M(\nu_m, \phi)$  is defined, can be divided into the four subspaces  $\mathcal{A}$ ,  $\mathcal{B}$ ,  $\mathcal{C}$ , and  $\mathcal{D}$ , as shown in Fig. 2, where  $\mathcal{A} = [|\nu_m| \leq \nu_c, 0 \leq \phi \leq 2\alpha(\nu_m) + 2\alpha(\nu_c)]$ ,  $\mathcal{B} = [|\nu_m| \leq \nu_c, 2\alpha(\nu_m) + 2\alpha(\nu_c) \leq \phi \leq \pi + 2\alpha(\nu_m)]$ ,  $\mathcal{C} = [|\nu_m| \leq \nu_c, \pi + 2\alpha(\nu_m) \leq \phi \leq \Phi^c]$ , and  $\mathcal{D} = [|\nu_m| \leq \nu_c, \Phi^c \leq \phi \leq 2\pi]$ . The value of  $\Phi^c$  is determined by

$$\Phi^c = \pi + 2\alpha(\nu_c). \quad (6)$$

Using (3), it can be verified that information of  $M(\nu_m, \phi)$  in subspace  $\mathcal{A}$  is redundant to that of  $M(\nu_m, \phi)$  in subspace  $\mathcal{C}$ . Similarly, information of  $M(\nu_m, \phi)$  in subspace  $\mathcal{B}$  is redundant to that of  $M(\nu_m, \phi)$  in subspace  $\mathcal{D}$ . Therefore, in principle, the modified data function  $M(\nu_m, \phi)$  is completely specified by its values in the subspaces  $\mathcal{A}$  and  $\mathcal{B}$ . However, because the boundary between the subspaces  $\mathcal{B}$  and  $\mathcal{C}$  is a nonlinear function of  $\nu_m$  and  $\phi$  and because each horizontal line in  $\mathcal{W}_c$  corresponds to a measurement acquired at a particular angle  $\phi$ , the information in subspaces  $\mathcal{B}$  and  $\mathcal{C}$  cannot in practice be determined independently of each other. Consequently, in order to determine  $M(\nu_m, \phi)$  in subspaces  $\mathcal{A}$  and  $\mathcal{B}$ , it is necessary to scan the union  $\mathcal{A} \cup \mathcal{B} \cup \mathcal{C} = [|\nu_m| \leq \nu_c, 0 \leq \phi \leq \Phi^c]$ . This observation can also be understood by examining the 2-D Fourier space coverage of  $a(\vec{r})$  that is obtained by varying the scanning angle from 0 to  $\Phi^c$ . As shown in Fig. 3, although the disk of Fourier space coverage with

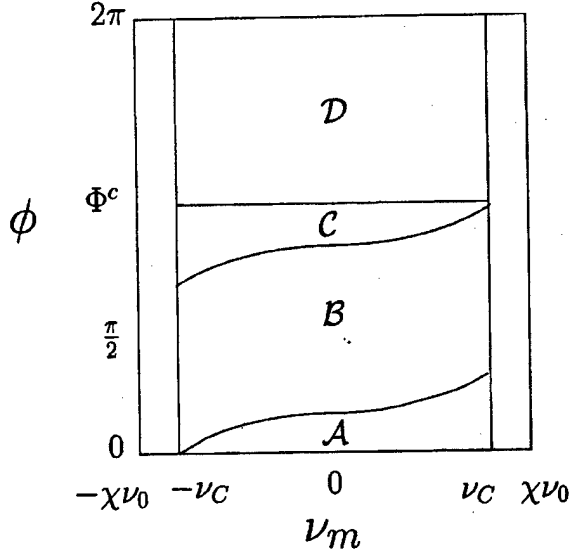


Fig. 2. The full-scan data space  $\mathcal{W}^c = \mathcal{A} \cup \mathcal{B} \cup \mathcal{C} \cup \mathcal{D}$  contains data in the angular range  $[0, 2\pi]$ . The subspace  $\mathcal{A} \cup \mathcal{B} \cup \mathcal{C}$  in  $[0, \Phi^c]$  contains all of the information necessary for exact reconstruction of the scattering object function whose 2-D Fourier transform is bandlimited to a disk of radius  $R_c(\nu_c)$ .

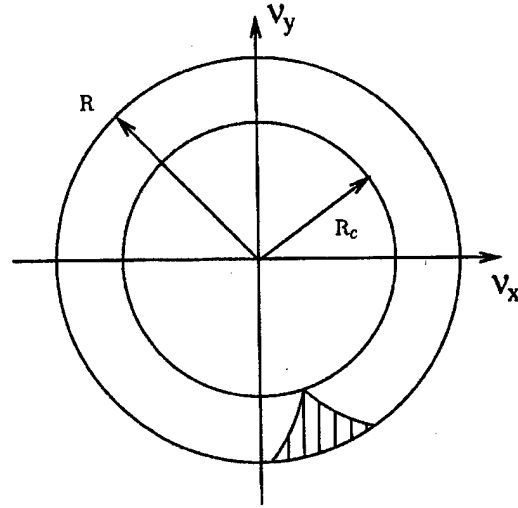


Fig. 3. The 2-D Fourier space coverage of the scattering object that is obtained by varying  $\phi$  from 0 to  $\Phi^c$ . The disk of Fourier space coverage with radius  $R = \nu_0 \sqrt{1 + 1/\chi^2}$  is incomplete, with the shaded region denoting the missing data. However, the coverage corresponding to the disk of radius  $R_c$ , which is defined by (5), is completely specified. In generating the figure,  $\Phi^c = 230^\circ$  and  $\chi = 1$  were utilized.

radius  $R = \nu_0 \sqrt{1 + 1/\chi^2}$  is incomplete, the coverage corresponding to the disk of radius  $R_c(\nu_c)$  is completely specified. Therefore, in order to exactly reconstruct  $a^c(\vec{r})$  whose 2-D Fourier transform  $A^c(\vec{\nu})$  is bandlimited to a disk of radius  $R_c(\nu_c)$ , only measurements corresponding to view angles in  $[0, \Phi^c]$  are required. Alternatively, for an arbitrary scattering object  $a(\vec{r})$  and specified  $\Phi^c > \pi$ , one can readily reconstruct  $a^c(\vec{r})$ , which is a low-pass filtered version of  $a(\vec{r})$  whose 2-D Fourier transform is bandlimited to the disk of radius  $R_c(\nu_c)$ , where the value of the data cutoff frequency  $0 \leq \nu_c \leq \chi\nu_0$  is determined by (6).

A plot of  $\Phi^c$  versus  $\nu_c/\nu_0$  for plane- and cylindrical-wave illumination is shown in Fig. 4. As expected, the maximum scanning angle  $\Phi^c$  is a monotonically increasing function of the data cutoff frequency  $\nu_c$ .

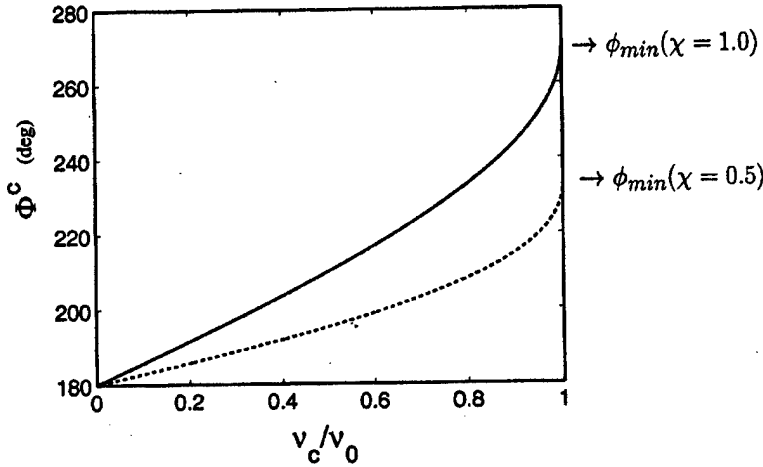


Fig. 4. A plot of  $\Phi^c$  versus  $\nu_c/\nu_0$  for  $\chi = 1$  (solid line) and  $\chi = 0.5$  (dashed line).

The nonlinear shape of the curves indicates the scanning angle can be reduced from  $\phi_{\min}$  (e.g., by  $30^\circ$ ) with little loss of resolution in the reconstructed image. Also, the fact that the plane-wave ( $\chi = 1$ ) curve is everywhere higher than the cylindrical-wave ( $\chi = 0.5$ ) curve reflects the fact that the angular scanning requirements of plane-beam DT are more restrictive than for fan-beam DT [5].

#### IV. SHORT-SCAN RECONSTRUCTION ALGORITHMS FOR LIMITED-VIEW DT

Although the data  $\mathcal{A} \cup \mathcal{B} \cup \mathcal{C}$  in Fig. 2 contains all of the information necessary for reconstruction of  $a^c(\vec{r})$ , subspaces  $\mathcal{A}$  and  $\mathcal{C}$  contain redundant information that needs to be properly normalized in the reconstruction process. This can be achieved by introducing a weighted modified data function as [4], [5]

$$M'(\nu_m, \phi) = w(\nu_m, \phi) M(\nu_m, \phi) \quad (7)$$

where  $w(\nu_m, \phi)$  satisfies

$$w(\nu_m, \phi) + w(-\nu_m, \phi + \pi - 2\alpha) = 1 \quad (8a)$$

everywhere in the data space  $\mathcal{W}_c$

$$w(\nu_m, \phi) = 1 \quad (8b)$$

in subspace  $\mathcal{B}$  and

$$w(\nu_m, \phi) = 0 \quad (8c)$$

in the subspace  $\{\mathcal{D} \cup \{|\nu_m| > \nu_c, 0 \leq \phi \leq 2\pi\}\}$ . The image  $a^c(\vec{r})$  can be reconstructed using a *short-scan FBPP (SS-FBPP) reconstruction algorithm* given by

$$\begin{aligned} a^{(w)}(r, \theta) = & \int_{\phi=0}^{\Phi^c} \int_{\nu_m=-\nu_c}^{\nu_c} \frac{\nu_0}{\nu'} |\nu_m| M'(\nu_m, \phi) \\ & \times \exp \left[ j2\pi \operatorname{sgn}(\nu_m) \sqrt{\frac{\nu_m^2}{\chi^2} + (\nu' - \nu_0)^2} r \cos(\phi - \alpha - \theta) \right] \\ & \times d\nu_m d\phi \end{aligned} \quad (9)$$

which reduces to the full-scan fan-beam FBPP algorithm [5] when  $\Phi^c = 2\pi$  and  $w(\nu_m, \phi) = 1/2$ . Note that different choice for  $w(\nu_m, \phi)$  that satisfy (8), in effect, specify different SS-FBPP algorithms.

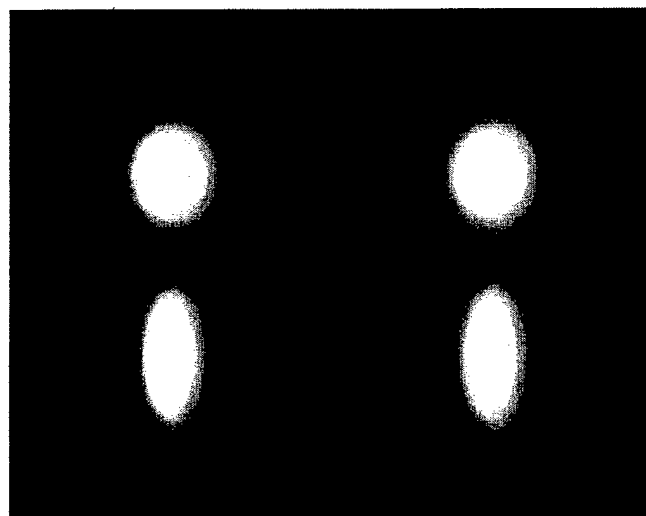
#### V. NUMERICAL RESULTS

To validate the theoretical results above, we considered a numerical phantom containing two elliptical disks whose 2-D Fourier transform was approximately bandlimited to a disk of radius  $R_c(\nu_c = 0.45\nu_0)$  [see (5)]. Data sets of simulated scattered fields were generated using the plane-wave FDP theorem (i.e.,  $\chi = 1$ ) and using various values for  $\Phi^c$ . We reconstructed images, which are shown in Fig. 5, from these data sets using the conventional FBPP and SS-FBPP algorithms. The SS-FBPP algorithm was specified by a weighting function  $w(\nu_m, \phi)$  that took on the values  $1/2, 1, 1/2$ , and  $0$ , in the data subspaces  $\mathcal{A}, \mathcal{B}, \mathcal{C}$ , and  $\mathcal{D}$ , respectively. Fig. 5(a) shows images reconstructed by use of the FBPP algorithm (left) and SS-FBPP algorithm (right), using data sets corresponding to  $\Phi^c = 2\pi$  and  $\Phi^c = \phi_{\min}(\chi = 1) = 3\pi/2$ , respectively. It is observed that both images appear virtually identical, reflecting the fact that both of these data sets contain the complete information about the scattering object.

Fig. 5(b) shows images reconstructed by use of the FBPP algorithm (left) and SS-FBPP algorithm (right), using a data set corresponding to  $\Phi^c = \pi + 2\alpha(0.45\nu_0) (\approx 207^\circ)$ . Clearly, the image reconstructed

using the FBPP algorithm is distorted and contains artifacts. However, the image reconstructed by use of the SS-FBPP algorithm appears correct and virtually identical to the images shown in Fig. 5(a). This confirms our assertion that the SS-FBPP algorithms, which utilize in the angular range  $[0, \Phi^c]$ , can exactly reconstruct a scattering object  $a^c(\vec{r})$  whose 2-D Fourier transform  $A^c(\vec{\nu})$  is bandlimited to a disk of radius  $R_c(\nu_c)$ , where  $\nu_c$  and  $\Phi^c$  are related by (6).

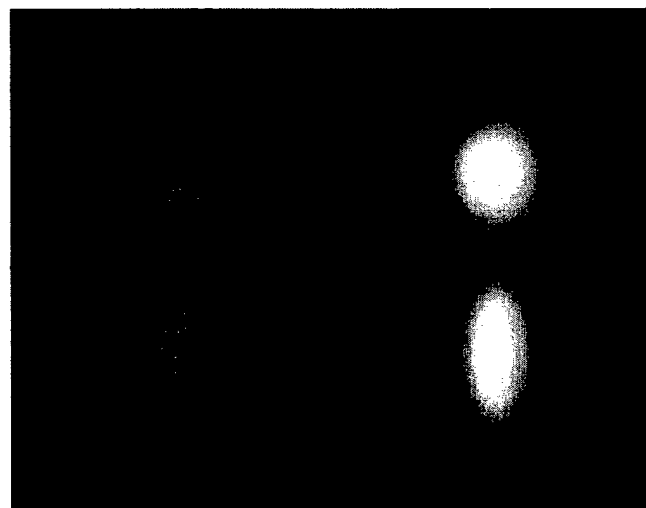
Fig. 5(c) shows images reconstructed by use of the FBPP algorithm (left) and SS-FBPP algorithm (right), using a data set corresponding to  $\Phi^c = \pi + 2\alpha(0.25\nu_0) (\approx 195^\circ)$ . Note that because the 2-D Fourier transform of  $a(\vec{r})$  has support on the disk of radius  $R_c(\nu_c = 0.45\nu_0)$ , the measurements in the angular range  $[0, \Phi^c = 195^\circ]$  do not completely specify the scattering object (i.e., the disk of coverage in 2-D Fourier space with radius  $R_c(\nu_c = 0.45\nu_0)$  will not be completely filled in.) As expected, the image reconstructed using the FBPP algorithm is blurred, distorted and contains artifacts. The image reconstructed using the SS-FBPP algorithm also appears blurred, but does not contain any noticeable distortions or artifacts. This confirms our assertion that, when the 2-D Fourier transform of a scattering object  $a(\vec{r})$  is not bandlimited to a disk of radius  $R_c(\nu_c)$ , the SS-FBPP algorithms that utilize the measurements corresponding to view angles in  $[0, \Phi^c]$  (where  $\nu_c$  and  $\Phi^c$  are related by (6)) can reconstruct a low-pass filtered version of  $a(\vec{r})$  whose 2-D Fourier transform is bandlimited to



(a)



(b)



(c)

Fig. 5. Images reconstructed using the FBPP and SS-FBPP algorithms for various simulated data sets. See the text for a detailed description.

the disk of radius  $R_c(\nu_c)$ . In this particular example, the 2-D Fourier transform of the image reconstructed by use of the SS-FBPP algorithm is bandlimited to a disk of radius  $R_c(.25/.45 \nu_c)$ .

## VI. SUMMARY

We demonstrated previously [4], [5] that in 2-D DT employing plane-wave or cylindrical-wave sources, one can exactly reconstruct the scattering object from a minimal-scan data set acquired using view angles only in  $[0, \phi_{\min}]$ , where  $\pi \leq \phi_{\min} \leq 3\pi/2$  is a specified function of the measurement geometry. In this study, we have demonstrated that when measurements are available only for view angles in  $[0, \Phi^c]$ , where  $\pi < \Phi^c < \phi_{\min}$ , a simple relationship exists between the maximum scanning angle  $\Phi^c$  and the image resolution when a FBPP algorithm is employed to reconstruct the image. By properly weighting the measurement data, a low-pass filtered approximation of the scattering object that is free of conspicuous artifacts can be obtained from the measurements corresponding to view angles in  $[0, \Phi^c]$ . When the scattering object is sufficiently bandlimited, it can be exactly reconstructed. This observation is practically useful, because it provides a convenient mechanism for regularizing the severely ill-posed limited-view DT reconstruction problem; when the maximum scanning angle  $\Phi^c$  is greater than  $\pi$ , a stable reconstruction can always be performed by sacrificing spatial resolution in the reconstructed image. It can be demonstrated that the statistical properties of the SS-FBPP algorithms are qualitatively similar to those of the minimal-scan FBPP reconstruction algorithms investigated previously [5]. In the limited-view radon transform inversion problem [9], an analogous regularization mechanism does not exist and some sort of *a priori* information regarding the object function is generally required to effectively regularize the problem.

Because we have assumed a 2-D imaging geometry in this study, the developed SS-FBPP reconstruction algorithms may be useful for applications in which out-of-plane scattering is not significant. In diffuse-photon density wave tomography, the wavenumber is complex-valued and the FDP theorem describes a mapping between the data function and a set of complex-valued frequencies of the scattering object function's Fourier transform. The extension of the concepts and techniques introduced in this correspondence to the case where the wavenumber is complex-valued and to the three-dimensional reconstruction problem represent important topics for future research.

## REFERENCES

- [1] S. Norton and T. Vo-Ding, "Diffraction tomographic imaging with photon density waves: An explicit solution," *J. Opt. Soc. Amer. A*, vol. 15, pp. 2670-2677, 1998.
- [2] X. Li, T. Durduran, A. G. Yodh, B. Chance, and D. N. Pattanayak, "Diffraction tomography for biomedical imaging with diffuse photon density waves," *Optics Lett.*, vol. 22, pp. 573-575, 1997.
- [3] C. Matson, "A diffraction tomographic model of the forward problem using diffuse photon density waves," *Optics Exp.*, vol. 1, pp. 6-11, 1997.
- [4] X. Pan and M. Anastasio, "Minimal-scan filtered backpropagation algorithms for diffraction tomography," *J. Opt. Soc. Amer. A*, vol. 16, pp. 2896-2903, 1999.
- [5] M. Anastasio and X. Pan, "Full- and minimal-scan reconstruction algorithms for fan-beam diffraction tomography," *Appl. Optics*, vol. 40, no. 20, pp. 3334-3345, 2001.
- [6] A. J. Devaney, "Generalized projection-slice theorem for fan-beam diffraction tomography," *Ultrason. Imag.*, vol. 7, pp. 264-275, 1985.
- [7] —, "A filtered backpropagation algorithm for diffraction tomography," *Ultrason. Imag.*, vol. 4, pp. 336-350, 1982.
- [8] —, "The limited view problem in diffraction tomography," *Inverse Prob.*, vol. 5, p. 501, 1989.
- [9] M. Davison, "The ill-conditioned nature of the limited angle tomography problem," *SIAM J. Appl. Math.*, vol. 43, pp. 428-448, 1983.

# Numerically Robust Minimal-Scan Reconstruction Algorithms for Diffraction Tomography via Radon Transform Inversion

Mark A. Anastasio,<sup>1</sup> Xiaochuan Pan<sup>2</sup>

<sup>1</sup> Pritzker Institute of Medical Engineering, Illinois Institute of Technology, 10 West 32nd Street, Chicago, Illinois 60616-3793

<sup>2</sup> Department of Radiology, The University of Chicago, Chicago, Illinois 60637

**ABSTRACT:** It is widely believed that measurements from a full angular range of  $2\pi$  are generally required to exactly reconstruct a complex-valued refractive index distribution in diffraction tomography (DT). In this work, we developed a new class of minimal-scan reconstruction algorithms for DT that utilizes measurements only over the angular range  $0 \leq \phi \leq 3\pi/2$  to perform an exact reconstruction. These algorithms, referred to as minimal-scan estimate-combination (MS-E-C) reconstruction algorithms, effectively operate by transforming the DT reconstruction problem into a conventional x-ray CT reconstruction problem that requires inversion of the Radon transform. We performed computer simulations to compare the noise and numerical properties of the MS-E-C algorithms against existing filtered backpropagation-based algorithms. © 2002 Wiley Periodicals, Inc. *Int J Imaging Syst Technol*, 12, 84–91, 2002; Published online in Wiley InterScience (www.interscience.wiley.com). DOI 10.1002/ima.10014

**Key words:** topographic reconstruction; diffraction tomography; wavefield inversion

## I. INTRODUCTION

In diffraction tomography (DT), a scattering object is interrogated using a diffracting acoustical or electromagnetic wavefield, and the scattered wavefield around the object is measured and used to reconstruct the refractive index distribution of the scattering object. There are numerous potential applications of DT that can be found in various scientific fields (Andre et al., 1995; Tabbara et al., 1988; Mueller et al., 1979; Kino, 1979; Devaney, 1984; Robinson, 1984). Recently, there has also been considerable interest in using DT to perform coherent x-ray imaging using third-generation synchrotron sources (Cheng and Han, 2001). Unlike the x-rays used in computed tomography (CT) that travel along straight lines, the radiation employed in DT has to be treated in terms of wavefronts and fields scattered by inhomogeneities in the object. In DT, the interaction between the incident wavefield and the object medium is governed by the inhomogeneous Helmholtz equation. Using a weak-scattering approximation, the inhomogeneous equation can be analytically solved (Wolf, 1969; Mueller et al., 1979) to obtain a linear relationship between the scattered field and the refractive index distribution.

This relationship has been used to develop DT reconstruction algorithms such as the well-known filtered backpropagation (FBPP) algorithm (Devaney, 1982), which is a generalization of the filtered backprojection (FBPJ) algorithm of x-ray CT.

It is widely believed that measurements from a full-angular range of  $2\pi$  around the scattering object are generally required to exactly reconstruct a complex-valued refractive index distribution (Devaney, 1982). However, we have recently revealed that one needs measurements only over the angular range  $0 \leq \phi \leq 3\pi/2$  to perform an exact reconstruction, and we developed minimal-scan filtered backpropagation (MS-FBPP) algorithms to achieve this (Pan and Anastasio, 1999). A useful characteristic of the MS-FBPP algorithms is their ability to decrease the data acquisition time by at least 25% over conventional (full-scan) algorithms. They can also reduce artifacts due to movement in or temporal fluctuations of the scattering object. Furthermore, in certain practical situations, it may be impossible to acquire measurements over a full  $2\pi$  angular range.

A new class of reconstruction algorithms has recently been developed for full-scan DT (in other words, DT employing measurements over a full  $2\pi$  angular range). These algorithms, referred to as estimate-combination (E-C) reconstruction algorithms (Pan, 1998; Anastasio and Pan, 2000b; Anastasio and Pan, 2000a), effectively operate by transforming the DT reconstruction problem into a conventional x-ray CT reconstruction problem that can be efficiently solved using the filtered backprojection (FBPJ) algorithm. The E-C reconstruction algorithms are more computationally efficient than the FBPP algorithm, and also provide a flexible framework for imposing unbiased regularization.

Because the E-C reconstruction algorithms involve a Fourier series expansion of the data function that is acquired over the angular range  $0 \leq \phi \leq 2\pi$ , they cannot be applied directly to the minimal-scan problem where measurements are only acquired over the angular range  $0 \leq \phi \leq 3\pi/2$ . Because of the potential advantages of the E-C reconstruction algorithms, it is important to generalize them to the minimal-scan situation. In this work, we developed minimal-scan E-C (MS-E-C) reconstruction algorithms for DT. We performed computer simulations to compare the noise and numerical properties of the MS-E-C and MS-FBPP algorithms. Our results quantitatively demonstrate that the MS-E-C algorithms pos-

Correspondence to: Mark A. Anastasio, Ph.D., Pritzker Institute of Medical Engineering, Illinois Institute of Technology, 10 West 32nd Street, Chicago, IL 60616-3793. (V) 312-567-3926, (F) 312-567-5707, Email: anastasio@iit.edu.

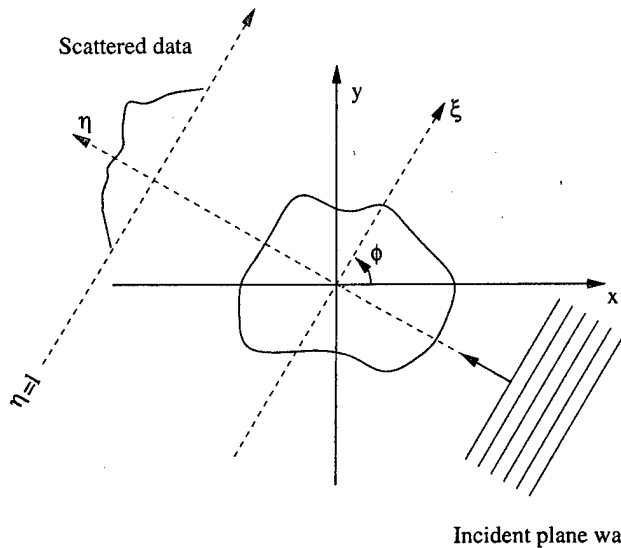


**Figure 1.** The classical scanning geometry of 2D DT. The insonifying plane wave propagates along the  $\eta$  axis, and the scattered wave field is measured along the line  $\eta = l$ . Full-scan and minimal-scan data sets are obtained by varying the measurement angle  $\phi$  between 0 and  $2\pi$  or between 0 and  $3\pi/2$ , respectively.

sess statistical and numerical properties superior to those of the MS-FBPP algorithms.

## II. BACKGROUND

**A. The Fourier Diffraction Projection Theorem.** In two-dimensional (2D) DT employing the classical scanning configuration, as shown in Figure 1, the scattering object is illuminated by monochromatic plane-wave radiation of frequency  $\nu_0$ , and the transmitted wavefield is measured along the  $\xi$  axis oriented at a measurement angle  $\phi$ , at a distance  $\eta = l$  from the origin. From measurements of the scattered wavefield obtained at various angles  $\phi$ , one seeks to reconstruct the scattering object function  $a(\vec{r})$ , which is related to the refractive index distribution  $n(r, \theta)$  by  $a(r, \theta) = n^2(r, \theta) - 1$ .

At a measurement angle  $\phi$ , the scattered data are measured along the line  $\eta = l$ , as shown in figure 1. Let  $U_s(\nu_m, \phi)$  to denote the 1D Fourier transform of the measured scattered data with respect to  $\xi$ . For convenience, we define a modified 1D Fourier transform of the scattered data as

$$M(\nu_m, \phi) = U_s(\nu_m, \phi) \frac{j\nu'}{2\pi^2\nu_0^2 U_0} e^{-j2\pi\nu' l}, \quad (1)$$

where  $\nu' = \sqrt{\nu_0^2 - \nu_m^2}$  and  $|\nu_m| \leq \nu_0$ . The quantities on the right-hand side of equation 1 are known or can be measured. Therefore, we will treat  $M(\nu_m, \phi)$  as a measurable data function. Under the Born approximation (Mueller et al., 1979), the Fourier diffraction projection (FDP) theorem (Mueller et al., 1979) can be derived, which is mathematically stated as

$$\begin{aligned} M(\nu_m, \phi) &= \int_{-\infty}^{\infty} \int_{-\infty}^{\infty} a(\vec{r}) e^{-j2\pi[\nu_m \xi - (\nu' - \nu_0)\eta]} d\vec{r} & \text{if } |\nu_m| \leq \nu_0 \\ &= 0 & \text{if } |\nu_m| > \nu_0, \end{aligned} \quad (2)$$

where the polar coordinates  $(r, \theta)$  and the rotated coordinates  $(\xi, \eta)$  are related through  $\xi = r \cos(\phi - \theta)$  and  $\eta = -r \sin(\phi - \theta)$ . The FDP theorem indicates that  $M(\nu_m, \phi)$  provides the values of the 2D Fourier transform of  $a(\vec{r})$  along the semi-circular arc AOB of radius  $\nu_0$ , as shown in figure 2.

## B. Minimal-Scan Filtered Backpropagation Algorithms.

The widely used filtered backpropagation (FBPP) algorithm (Devaney, 1982) is mathematically expressed as

$$a(\vec{r}) = \frac{1}{2} \int_{\phi=0}^{2\pi} \int_{\nu_m=-\nu_0}^{\nu_0} \frac{\nu_0}{\nu'} |\nu_m| M(\nu_m, \phi) e^{j2\pi\nu_m \xi + 2\pi\nu' \eta} d\nu_m d\phi, \quad (3)$$

where  $\nu_\mu = j(\sqrt{\nu_0^2 - \nu_m^2} - \nu_0)$ . When  $\nu_0 \rightarrow \infty$ , the FBPP algorithm reduces to the filtered backprojection (FBPJ) algorithm of x-ray CT. The FBPP algorithm generally requires full knowledge of  $M(\nu_m, \phi)$  in the data space  $\mathcal{W} = [|\nu_m| \leq \nu_0, 0 \leq \phi \leq 2\pi]$ , for exact reconstruction of the generally complex-valued object function. We will refer to such full knowledge of  $M(\nu_m, \phi)$  as a *full-scan data set*. The full-scan data space  $\mathcal{W}$  can be decomposed into four subspaces,  $\mathcal{A}$ ,  $\mathcal{B}$ ,  $\mathcal{C}$ , and  $\mathcal{D}$ , where  $\mathcal{A} = [|\nu_m| \leq \nu_0, 0 \leq \phi \leq 2\alpha + \pi/2]$ ,  $\mathcal{B} = [|\nu_m| \leq \nu_0, \pi/2 + 2\alpha \leq \phi \leq \pi + 2\alpha]$ ,  $\mathcal{C} = [|\nu_m| \leq \nu_0, \pi + 2\alpha \leq \phi \leq 3\pi/2]$  and  $\mathcal{D} = [|\nu_m| \leq \nu_0, 3\pi/2 \leq \phi \leq 2\pi]$ , where  $\alpha = \text{sgn}(\nu_m) \arcsin \sqrt{\nu_m^2 - \nu_\mu^2} / (2\nu_0)$ . A schematic of this partitioning of the data space is given in figure 3. Using the FDP theorem, it can be shown (Pan and Kak, 1983) that  $M(\nu_m, \phi) = M(-\nu_m, \phi + \pi - 2\alpha)$ . Therefore, the information contained in subspace  $\mathcal{A}$  is redundant to that contained in subspace  $\mathcal{C}$ , and the information contained in subspace  $\mathcal{B}$  is redundant to that contained in subspace  $\mathcal{D}$ . We have demonstrated (Pan and Anastasio, 1999) that it is possible to exactly reconstruct the object function using only knowledge of  $M(\nu_m, \phi)$  in the subspace  $\mathcal{M} = \mathcal{A} \cup \mathcal{B}$ .

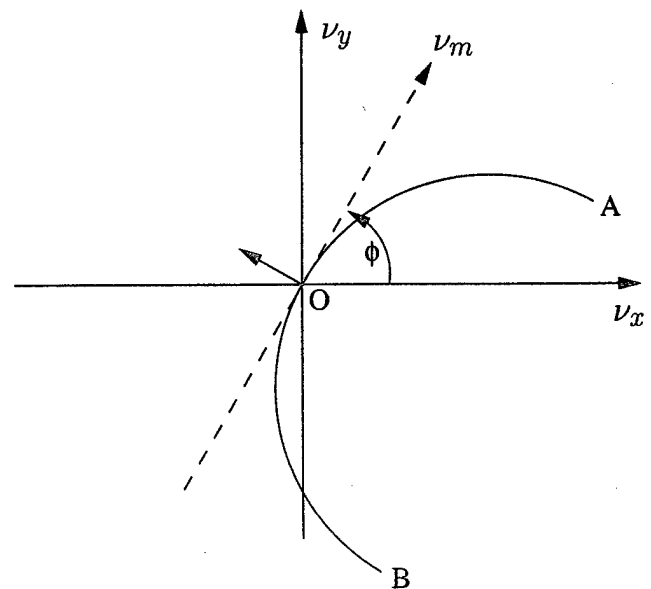


**Figure 2.** The FDP theorem states that  $M(\nu_m, \phi)$  is equal to the 2D Fourier transform of  $a(\vec{r})$  along a semi-circle AOB that has a radius of  $\nu_0$  and is centered at  $\nu_\eta = \nu_0$ .

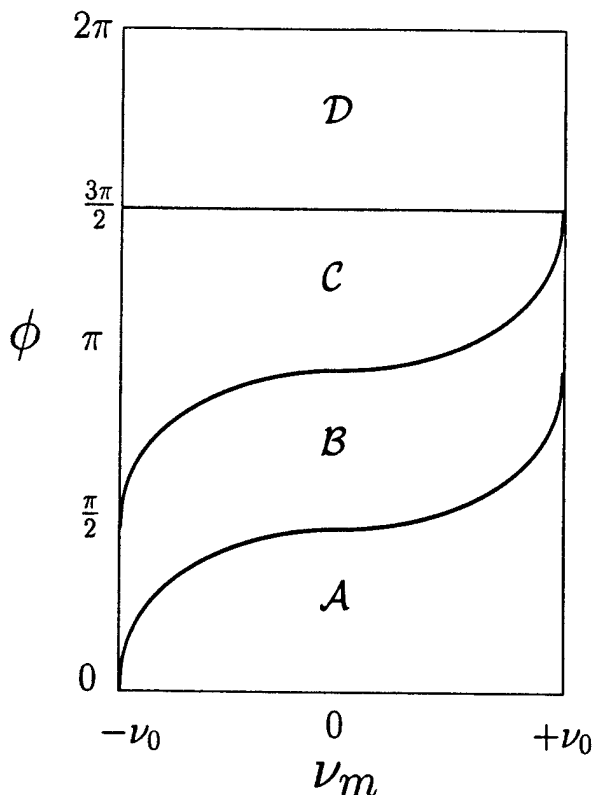


**Figure 3.** The subspaces  $\mathcal{A}$ ,  $\mathcal{B}$ ,  $\mathcal{C}$  and  $\mathcal{D}$  in the complete DT data space.

$\cup \mathcal{C} = \{|\nu_m| \leq \nu_0, 0 \leq \phi \leq 3\pi/2\}$ , which we refer to as a *minimal-scan data set*.

Although the minimal-scan data set  $\mathcal{M}$  contains all of the information necessary for exact reconstruction of the scattering object function, the redundant information contained in the subspaces  $\mathcal{A}$  and  $\mathcal{C}$  needs to be properly normalized in the reconstruction process (Pan and Anastasio, 1999). The MS-FBPP algorithms operate by first normalizing such partially redundant information by generating an appropriately weighted minimal-scan data set  $M'(\nu_m, \phi)$  and subsequently using the FBPP algorithm described by equation 3 (scaled by a factor of 2), to exactly reconstruct the image. The weighted minimal-scan data set is given by (Pan and Anastasio, 1999)

$$M'(\nu_m, \phi) = w(\nu_m, \phi)M(\nu_m, \phi), \quad (4)$$

where  $w(\nu_m, \phi)$  is a function of  $\nu_m$  and  $\phi$ , which satisfies

$$w(\nu_m, \phi) + w(-\nu_m, \phi + \pi - 2\alpha) = 1 \quad (5a)$$

in complete data space  $\mathcal{W}$ ,

$$w(\nu_m, \phi) = 1 \quad (5b)$$

in subspace  $\mathcal{B}$ , and

$$w(\nu_m, \phi) = 0 \quad (5c)$$

in subspace  $\mathcal{D}$ . Although the forms of  $w(\nu_m, \phi)$  in subspaces  $\mathcal{B}$  and  $\mathcal{D}$  are completely specified by equations 5b and 5c, respectively, the explicit forms of  $w(\nu_m, \phi)$  in subspaces  $\mathcal{A}$  and  $\mathcal{C}$  are unspecified for the moment. In principle, one can choose different  $w(\nu_m, \phi)$  in subspaces  $\mathcal{A}$  and  $\mathcal{C}$  as long as these  $w(\nu_m, \phi)$  satisfy equation 5a.

### III. MINIMAL-SCAN ESTIMATE-COMBINATION ALGORITHMS

The previously derived (full-scan) E-C reconstruction algorithms are more computationally efficient than the (full-scan) FBPP reconstruction algorithms, which involve a depth-dependent filtering operation (backpropagation). Accordingly, we expect that the MS-FBPP algorithms, which use the FBPP algorithm to reconstruct the final image from the weighted data function  $M'(\nu_m, \phi)$ , will also be less computationally efficient than the E-C reconstruction algorithms. Because they will involve fewer and less complicated numerical operations, we also expect that the MS-E-C algorithms will be minimize the propagation of data noise and errors as compared to the MS-FBPP algorithms. The full-scan E-C reconstruction algorithms (Pan, 1998; Anastasio and Pan, 2000b) involve a Fourier series expansion of the data function  $M(\nu_m, \phi)$ , which requires knowledge of  $M(\nu_m, \phi)$  over an angular range of  $2\pi$ , and therefore can not be directly applied to the minimal-scan data set containing only measurements in the range  $0 \leq \phi \leq 3\pi/2$ . Below, we develop minimal-scan E-C (MS-E-C) reconstruction algorithms that can be directly applied to the minimal-scan data set.

**A. The Radon Transform.** Let  $p(\xi, \phi)$  and  $P_k(\nu_a)$  denote the Radon transform of  $a(r, \theta)$  and its 2D Fourier transform, respectively. (Here, the 2D Fourier transform is actually a 1D Fourier transform with respect to  $\xi$  and a 1D Fourier series with respect to  $\phi$ .) From knowledge of  $p(\xi, \phi)$ , or equivalently,  $P_k(\nu_a)$ , one can reconstruct  $a(r, \theta)$  by use of the computationally efficient and numerically stable FBPP algorithm, which is given by

$$a(r, \theta) = \frac{1}{2} \int_0^{2\pi} \int_{-\infty}^{\infty} \sum_{k=-\infty}^{\infty} P_k(\nu_a) e^{ik\phi} |\nu_a| e^{j\nu_a r \cos(\phi - \theta)} d\nu_a d\phi. \quad (6a)$$

For theoretical convenience, the FBPP algorithm can also be expressed as

$$a(r, \theta) = 2\pi \sum_{k=-\infty}^{\infty} j^k \int_{\nu_a=0}^{\infty} P_k(\nu_a) e^{ik\theta} J_k(2\pi\nu_a r) \nu_a d\nu_a, \quad (6b)$$

where  $J_k(\cdot)$  is a Bessel function of the first kind. The MS-E-C algorithms will operate by estimating  $P_k(\nu_a)$ , or equivalently  $p(\xi, \phi)$ , from the minimal-scan data set, and using the FBPP algorithm to reconstruct the final image  $a(r, \theta)$ .

**B. Derivation of the MS-E-C Algorithms.** Consider a given weighting function  $w(\nu_m, \phi)$  in equation 4. The corresponding MS-FBPP algorithm can be expressed as (Pan and Anastasio, 1999)

$$a(r, \theta) = \frac{1}{2} \int_{\phi=0}^{2\pi} \int_{\nu_m=-\nu_0}^{\nu_0} \frac{\nu_0}{\nu'} |\nu_m| M'(\nu_m, \phi) e^{j2\pi\nu_m \cdot \xi + 2\pi\nu_m \eta} d\nu_m d\phi. \quad (7)$$

Let  $M'_k(\nu_m)$  denote the Fourier series expansion of  $M'(\nu_m, \phi)$ . One can re-express equation 7 as

$$a(r, \theta) = \frac{1}{2} \int_{\phi=0}^{2\pi} \int_{\nu_m=-\nu_0}^{\nu_0} \frac{\nu_0}{\nu'} |\nu_m| e^{j2\pi\nu_m\xi + 2\pi\nu_m\eta + jk\phi} \sum_{k=-\infty}^{\infty} M'_k(\nu_m) e^{jk\phi} d\nu_m d\phi. \quad (8)$$

Using the definition  $\gamma(\nu_m) = e^{j\alpha}$  and separating the contribution to the integral from positive and negative  $\nu_m$ , equation 8 can be re-written as

$$a(r, \theta) = \frac{1}{2} \int_{\phi=0}^{2\pi} \int_{\nu_m=0}^{\nu_0} \frac{\nu_0}{\nu'} \nu_m e^{j2\pi\nu_m\xi + 2\pi\nu_m\eta + jk\phi} \sum_{k=-\infty}^{\infty} M'_k(\nu_m) d\nu_m d\phi + \frac{1}{2} \int_{\phi=0}^{2\pi} \int_{\nu_m=-\nu_0}^0 \frac{\nu_0}{\nu'} (-\nu_m) e^{j2\pi\nu_m\xi + 2\pi\nu_m\eta + jk\phi} \sum_{k=-\infty}^{\infty} M'_k(\nu_m) d\nu_m d\phi. \quad (9)$$

Changing  $\nu_m$  to  $-\nu_m$  in the second term in equation 9 and grouping  $\phi$ -dependent terms yields

$$a(r, \theta) = \frac{1}{2} \int_{\nu_m=0}^{\nu_0} \frac{\nu_0}{\nu'} \nu_m \left\{ \int_{\phi=0}^{2\pi} e^{j2\pi\nu_m\xi + 2\pi\nu_m\eta + jk\phi} d\phi \right\} \times \sum_{k=-\infty}^{\infty} M'_k(\nu_m) d\nu_m + \frac{1}{2} \int_{\phi=0}^{2\pi} \int_{\nu_m=0}^{\nu_0} \frac{\nu_0}{\nu'} \nu_m \left\{ \int_{\phi=0}^{2\pi} e^{-j2\pi\nu_m\xi + 2\pi\nu_m\eta + jk\phi} d\phi \right\} \sum_{k=-\infty}^{\infty} M'_k(-\nu_m) d\nu_m. \quad (10)$$

The integrals in the curly braces of the first and second terms of equation 10 can be evaluated (Metz and Pan, 1995) yielding the expressions  $2\pi j^k \gamma(\nu_m)^k e^{jk\theta} J_k(2\pi r \sqrt{\nu_m^2 - \nu_\mu^2})$  and  $2\pi (-1)^k j^k \gamma(\nu_m)^{-k} e^{jk\theta} J_k(2\pi r \sqrt{\nu_m^2 - \nu_\mu^2})$ , respectively. Using this result and the change of variables  $\nu_a = \sqrt{\nu_m^2 - \nu_\mu^2}$  (which implies  $\nu_a d\nu_a = \nu_0/\nu' \nu_m d\nu_m$ ), we arrive at

$$a(r, \theta) = \pi \sum_{k=-\infty}^{\infty} j^k \int_{\nu_a=0}^{\sqrt{2}\nu_0} [\gamma^k M'_k(\nu_m) + (-1)^k \gamma^{-k} M'_k(-\nu_m)] \times e^{jk\theta} J_k(2\pi\nu_a r) \nu_a d\nu_a, \quad (11)$$

where  $\nu_m = \nu_a \sqrt{1 - \nu_\mu^2/2\nu_0^2}$ . Comparison of Eqns. 11 and 6b indicates that, for  $0 \leq \nu_a \leq \sqrt{2}\nu_0$ ,

$$P_k(\nu_a) = \frac{1}{2} [\gamma^k M'_k(\nu_m) + (-1)^k \gamma^{-k} M'_k(-\nu_m)], \quad (12)$$

and therefore the Radon transform of the scattering object function  $a(r, \theta)$  can be estimated from the appropriately weighted minimal-scan data set. The use of equation 12 to estimate  $P_k(\nu_a)$  coupled with the 2D FBPJ algorithm to reconstruct  $a(r, \theta)$  is referred to as a MS-E-C reconstruction algorithm. In practice, the FBPJ algorithm described by equation 6a requires knowledge of  $P_k(\nu_a)$  for evenly spaced values of  $\nu_a$  spanning the range  $-\sqrt{2}\nu_0 \leq \nu_a \leq \sqrt{2}\nu_0$  in order to be efficiently implemented using the fast Fourier transform (FFT). In this case, the consistency condition (Deans, 1983)  $P_k(\nu_a) = (-1)^k P_k(-\nu_a)$  can be employed to obtain values of  $P_k(\nu_a)$  for negative  $\nu_a$ .

#### IV. NUMERICAL SIMULATIONS

We performed simulation studies to evaluate and compare the numerical and statistical properties of images obtained by use of the MS-E-C and MS-FBPP reconstruction algorithms.

**A. Measurement Data.** We investigated the statistical properties of the reconstruction algorithms under near-ideal conditions by employing a single component scattering object that exactly satisfied the (first-order) Born approximation. The propagation of deterministic artifacts by the reconstruction algorithms under less-than-ideal conditions was investigated by employing a two component scattering object that introduced strong and multiple-scattering effects into the measurement data.

**A.1 Single-Scattered (Born) Data and Noise Model.** The scattering object function, shown in figure 4, was taken to be a lossless, uniform cylindrical disk with a diameter of 30 pixels that was convolved with a symmetric Gaussian function with a standard deviation of 0.2 pixel. The Fourier transform of the object function was therefore approximately bandlimited to a circular disk of radius  $\sqrt{2}\nu_0$  in its 2D Fourier space. It was assumed that the scatterer was weakly scattering, so that the Born approximation may reasonably be taken to hold. Therefore, these numerical simulations were designed to investigate the statistical properties of the reconstruction algorithms rather than the weak scattering model. Minimal-scan data sets were generated by using the FDP theorem to calculate simulated scattered field data for 96 measurement angles  $\phi$  that were evenly spaced between 0 and  $3\pi/2$ . At each measurement angle, 128 samples were calculated with a sampling increment  $\Delta\xi = 1/2\nu_0$ , where  $\nu_0$  is the frequency of the incident plane wave.

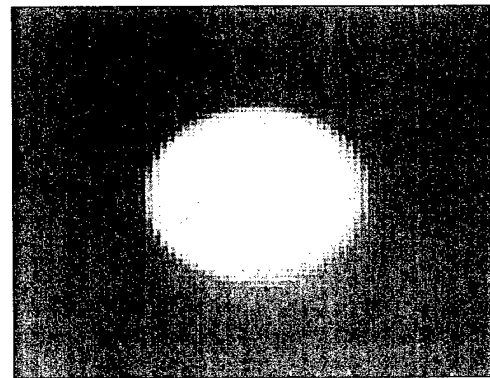


**Figure 4.** The original scattering object function was formed by convolving a uniform circular disk with a diameter of 30 pixels with a circularly symmetric Gaussian function with a standard deviation of 0.2 pixels.

Table I. Error values of the reconstructed images shown in Figs. 9–11.

Contrast	MS-E-C Error	MS-FBPP Error
1.01	12.03	13.68
1.05	51.26	53.70
1.08	115.25	119.13

## V. RESULTS

**A. Single-Scattered (Born) Data Case.** We first used the MS-E-C and MS-FBPP algorithms to reconstruct the scattering object function using the simulated noiseless minimal-scan data set. The images reconstructed using the MS-E-C and MS-FBPP algorithms are displayed in figures 5a and 5b, respectively. It is observed that, in the absence of noise, both the MS-E-C and MS-FBPP algorithms can, with high fidelity, reconstruct the original scattering object function from the minimal-scan data set.

Using one of the noisy minimal-scan data sets, we used the MS-E-C and MS-FBPP algorithms to reconstruct the scattering object function. The noisy images reconstructed using the MS-E-C and MS-FBPP algorithms are displayed in figures 6a and 6b, respectively. The image reconstructed using the MS-E-C algorithm (Fig. 6a) appears less affected by the data noise and more closely resembles the original object than does the image reconstructed using the MS-FBPP algorithm (Fig. 6b). The local image variance, which was empirically calculated from the two sets of 250 noisy images reconstructed using the MS-E-C and MS-FBPP algorithms, quantitatively confirms this observation. Figure 7 is a plot of the local variance obtained from the MS-FBPP reconstructed images divided by the local variance obtained from the MS-E-C reconstructed images. Clearly, the ratio of the variances is everywhere greater than one, and near the corners of the reconstructed image is as great as ten. This quantitatively demonstrates that the MS-E-C reconstruction algorithms are less susceptible to the effects of data noise than are the MS-FBPP reconstruction algorithms.

**B. Multiple-Scattering Case.** Using the MS-E-C and MS-FBPP algorithms we reconstructed the two component scattering objects shown in figures 9–11, which correspond to the cases where the cylinders had refractive index values of  $n(\vec{r}) = 1.01, 1.05$ , and  $1.08$ , respectively. In each case, the image reconstructed by use of the MS-E-C algorithm (Figs. 9a–11a) appears to contain less pronounced artifacts than does the image reconstructed by use of the MS-FBPP algorithm (Figs. 9b–11b). This observation is confirmed by Table I, which shows that for each value of  $n(\vec{r})$  the MS-E-C algorithm produced images that have lower error values than the corresponding images produced by the MS-FBPP algorithm. This quantitatively demonstrates that the MS-E-C algorithms are less susceptible to multiple-scattering effects and other deterministic inconsistencies than are the MS-FBPP algorithms. However, as one would expect, the performance of both algorithms dramatically deteriorates as the refractive index values increases and the Born condition (Chen and Stamnes, 1998) is severely violated.

## VI. DISCUSSION

Previously we have shown (Pan and Anastasio, 1999) that, in DT employing the 2D classical scanning geometry, the minimal-scan data set acquired using view angles only in  $[0, 3\pi/2]$  contains all of the information necessary to exactly reconstruct the scattering object function. We subsequently developed a class of MS-FBPP algo-

gorithms that were capable of exactly reconstructing the scattering object function from the minimal-scan data set.

In this work, we have developed a novel class of reconstruction algorithms for the minimal-scan DT reconstruction problem. These algorithms, referred to as MS-E-C reconstruction algorithms, have distinct advantages over the MS-FBPP reconstruction algorithms. Because the FBPP algorithm used by the MS-E-C algorithms does not involve a depth-dependent filtering, the MS-E-C algorithms are more computationally efficient than are the MS-FBPP algorithms. More importantly, we have quantitatively demonstrated that the MS-E-C algorithms are less susceptible to data noise, modeling errors due to the violation of weak scattering conditions, and other finite sampling effects than are the MS-FBPP algorithms. This result is consistent with the observation that the MS-FBPP algorithms involve more complicated numerical operations than do the MS-E-C algorithms, which may amplify the propagation of noise and errors into the reconstructed image. Therefore, the use of a MS-E-C algorithm instead of a MS-FBPP algorithm (using the same weighting function) will generally result in a reduction of the reconstructed image variance and/or a reduction of the image artifacts.

Recently, non-linear reconstruction algorithms that incorporate higher-order scattering approximations have been proposed for full-scan DT (Lu and Zhang, 1996; Tsihrintzis and Devaney, 2000b; Tsihrintzis and Devaney, 2000a). The generalization of these works to case of minimal-scan DT is an important task that is currently under way.

## REFERENCES

- M. Anastasio and X. Pan, Computationally efficient and statistically robust image reconstruction in 3D diffraction tomography, *J Opt Soc Amer*, 17 (2001a), 391–400.
- M. Anastasio and X. Pan, A new reconstruction algorithm for reflection-mode diffraction tomography, *IEEE Trans Image Process*, 9 (2001b), 1262–1271.
- M.P. Andre, P.J. Martin, G.P. Otto, L.K. Olson, T.K. Barrett, B.A. Apivey, and D.A. Palmer, A new consideration of diffraction computed tomography for breast imaging, *Acoust Imag*, 21 (1995), 379–390.
- M. Azimi and A. Kak, Distortion in diffraction tomography caused by multiple scattering, *IEEE Trans Med Imag*, 2 (1983), 176–195.
- B. Chen and J. Stamnes, Validity of diffraction tomography based on the first-Born and first-Rytov approximations, *Appl Opt*, 37 (1998), 2996–3006.
- J. Cheng and S. Han, Diffraction tomography reconstruction algorithms for quantitative imaging of phase objects, *J Opt Soc Amer (A)*, 18, 7 (2001), 1460–1464.
- S. Deans, *The Radon Transform and Some of Its Applications*, (1983), Wiley, New York.
- A. Devaney, A filtered backpropagation algorithm for diffraction tomography, *Ultra Imag*, 4 (1982), 336–350.
- A. Devaney, Geophysical diffraction tomography, *IEEE Trans Geo Rem Sens*, 22 (1984), 3–13.
- A. Ishimaru, *Wave Propagation and Scattering in Random Media*, (1978), Academic, New York.
- G. Kino, Acoustic imaging for nondestructive evaluation, *Proc IEEE*, 67 (1979), 510–525.
- Z.-Q. Lu and Y.-Y. Zhang, Acoustical tomography based on the second-order born transform perturbation approximation, *IEEE Trans Ultra, Ferro, and Freq Cont*, 43 (1996), 296–302.
- C.E. Metz and X. Pan, A unified analysis of exact methods of inverting the 2-D exponential radon transform, with implications for noise control in spect, *IEEE Trans Med Imag*, 14 (1995), 643–658.



- R. Mueller, M. Kaveh, and G. Wade, Reconstructive tomography and applications to ultrasonics, *Proc IEEE*, 67 (1979), 567-587.
- S. Pan and A. Kak, A computational study of reconstruction algorithms for diffraction tomography: Interpolation versus filtered backpropagation, *IEEE Trans Acous Sp and Sig Proc*, 31 (1983), 1262-1275.
- X. Pan, A unified reconstruction theory for diffraction tomography with considerations of noise control, *J Opt Soc Amer (A)*, 15 (1998), 2312-2326.
- X. Pan and M. Anastasio, Minimal-scan filtered back-propagation algorithms for diffraction tomography, *J Opt Soc Amer (A)*, 16 (1999), 2896-2903.
- E. Robinson, Image reconstruction in exploration geophysics, *IEEE Trans Son and Ultrason*, 31 (1984), 259-270.
- W. Tabbara, B. Duchene, C. Pichot, D. Lesselier, L. Chommeloux, and N. Joachimowicz, Diffraction tomography: contribution to the analysis of some applications in microwaves and ultrasonics, *Inverse Problems*, 4 (1988), 305-331.
- G. Tsihrintzis and A. Devaney, Higher order (nonlinear) diffraction tomography: Inversion of the Rytov series, *IEEE Tran Inf Theory*, 46 (2000a), 1748-1761.
- G. Tsihrintzis and A. Devaney, Higher-order (nonlinear) diffraction tomography: Reconstruction algorithms and computer simulation, *IEEE Trans Imag Proc*, 9 (2000b), 1560-1572.
- E. Wolf, Three-dimensional structure determination of semi-transparent objects from holographic data, *Opt Comm*, 1 (1969), 153-156.

# An Improved Reconstruction Algorithm for 3D Diffraction Tomography Using Spherical-Wave Sources

Mark A. Anastasio and Xiaochuan Pan<sup>†</sup>

Pritzker Institute of Medical Engineering  
Illinois Institute of Technology  
Chicago, Illinois 60616

<sup>†</sup> Department of Radiology  
The University of Chicago  
Chicago, Illinois 60637

## Abstract

Diffraction tomography (DT) is an inversion technique that reconstructs the refractive index distribution of a weakly scattering object. In this paper, a novel reconstruction algorithm for 3D diffraction tomography employing spherical-wave sources is mathematically developed and numerically implemented. Our algorithm is numerically robust and is much more computationally efficient than the conventional filtered backpropagation algorithm. Our previously developed algorithm for DT using plane-wave sources is contained as a special case.

## Keywords

Diffraction tomography, wavefield inversion, 3D imaging

## I. INTRODUCTION

In diffraction tomography (DT), a weakly scattering object is interrogated using a diffracting wavefield, and the scattered wavefield around the object is measured and used to reconstruct the (low-pass filtered) refractive index distribution of the scattering object. The principles of DT have been extensively utilized for developing optical [1, 2] and acoustic [3] tomographic imaging systems for biomedical applications.

It is widely known that the filtered backpropagation (FBPP) and direct Fourier (DF) reconstruction algorithms for three-dimensional (3D) DT possess certain limitations [4]. The depth-dependent filtering (back-propagation) in the 3D FBPP algorithm requires a large number of 2D fast Fourier transforms (FFTs) to be performed for processing the measured data at each measurement view, which renders the 3D FBPP algorithm extremely computationally demanding. Furthermore, we have shown that (in two-dimensional (2D) DT) the FBPP algorithm may considerably amplify data noise [5]. The 3D DF algorithms require the use of a 3D interpolation method to obtain samples on a 3D Cartesian grid in the Fourier space of the scattering object, upon which a 3D inverse FFT can be employed to reconstruct the scattering object function. Because the sample density in the 3D Fourier space obtained from the measured data is non-uniform, sophisticated and computationally demanding interpolation strategies are generally required to avoid producing significant interpolation errors that would degrade the accuracy of the reconstructed image.

For 3D DT employing plane-wave sources, we have recently developed a new class of reconstruction algorithms that circumvent the shortcomings of the 3D FBPP and DF algorithms [4]. These algorithms, referred to as plane-wave estimate-combination (E-C) reconstruction algorithms, effectively reduce the 3D DT reconstruction problem to a series of 2D X-ray reconstruction problems, and thus greatly reduce the

large computational load required by conventional 3D DT reconstruction algorithms. Additionally, these algorithms do not require an explicit 3D interpolation in the Fourier space of the scattering object.

In many imaging applications [1, 6], it may be useful to utilize a diverging spherical-wave rather than a plane-wave to interrogate the scattering object. Because of the distinct advantages of the E-C reconstruction algorithms for plane-wave DT [4], it is important to generalize them to DT employing spherical-wave sources. In this work, we generalize our previously developed (plane-wave) E-C reconstruction algorithms to DT employing spherical-wave sources and numerically demonstrate the developed algorithm using simulated data.

## II. BACKGROUND

We will utilize the model of spherical-wave DT described by Devaney in [7], the scanning geometry of which is shown in Fig. 1. The case of 3D DT utilizing a plane-wave source can be viewed as a special case of spherical-wave DT and will be discussed below. The scattering object is illuminated by monochromatic spherical-wave source located at the position  $\eta = -S$  on the  $\eta$ -axis, emitting a wavefield of the form

$$u_0(\xi, z, \phi) = A_0 \frac{e^{j2\pi\nu_0|\vec{r}-S\hat{\beta}|}}{|\vec{r}-S\hat{\beta}|} = A_0 \frac{e^{j2\pi\nu_0\sqrt{\xi^2+z^2+(S+D)^2}}}{\sqrt{\xi^2+z^2+(S+D)^2}}, \quad (1)$$

where  $A_0$  is the complex amplitude,  $k = 2\pi\nu_0$  is the wavenumber,  $\hat{\beta}$  is a unit vector pointing along the positive  $\eta$ -axis, and  $D$  is the distance of the detector surface from the center of rotation. From the scattered wavefield measured in the  $\xi$ - $z$  plane oriented at a measurement angle  $\phi$  and located at a distance  $\eta = D$  from the origin, one seeks to reconstruct the scattering object function  $a(\vec{r})$ . The underlying physical property of the scattering object that is mapped in DT is the refractive index distribution  $n(\vec{r})$ , which is related to the scattering object function by the equation  $a(\vec{r}) = n^2(\vec{r}) - 1$ .

Let  $u(\xi, z, \phi)$  denote the measured total wavefield in the  $\xi$ - $z$  plane positioned at  $\eta = D$ , as shown in Fig. 1. The scattered data is given by

$$u_s(\xi, z, \phi) = u(\xi, z, \phi) - u_0(\xi, z, \phi), \quad (2)$$

which can be treated as a measurable data function because  $u(\xi, z, \phi)$  can be measured and because  $u_0(\xi, z, \phi)$  is assumed known. We can introduce a modified data function

$$M(\nu_m, \nu_z, \phi) = \frac{\chi}{\pi\nu_0^2} \nu' e^{-j2\pi(\nu'-\nu_0)D} \mathcal{F}_{\nu_m} \left\{ \frac{u_s(\xi, z, \phi)}{u_0(\xi, z, \phi)} \right\}, \quad (3)$$

where  $\mathcal{F}_{\nu_m, \nu_z} \{h(\xi, z)\} = \frac{1}{2\pi} \int_{-\infty}^{\infty} \int_{-\infty}^{\infty} h(\xi) e^{-j2\pi(\nu_m\xi + \nu_z z)} d\xi dz$ ,

$$\chi = \sqrt{\frac{S}{S+D}}, \quad (4)$$

and

$$\nu' = \sqrt{\nu_0^2 - \frac{\nu_m^2}{\chi^2} - \frac{\nu_z^2}{\chi^2}}. \quad (5)$$

Using paraxial<sup>1</sup> and weak scattering approximations, Devaney derived [7] the spherical-wave FDP theorem that is given by

$$M(\nu_m, \nu_z, \phi) = \int_{-\infty}^{\infty} \int_{-\infty}^{\infty} a(\vec{r}) e^{-j2\pi[\frac{\nu_m}{\chi^2}\xi + \frac{\nu_z}{\chi^2}z + (\nu' - \nu_0)\eta]} d\vec{r} \quad \text{if } \nu_m^2 + \nu_z^2 \leq \chi^2\nu_0^2$$

<sup>1</sup>The paraxial approximation requires that both  $S$  and  $D$  are much larger than the size of the scattering object.

$$= 0 \quad \text{if } \nu_m^2 + \nu_z^2 > \chi^2 \nu_0^2. \quad (6)$$

Equation 6 states that the modified data function,  $M(\nu_m, \nu_z, \phi)$ , is equal to a semi-ellipsoidal slice, oriented at angle  $\phi$ , through the 3D Fourier transform of the object function  $a(\vec{r})$ . In this work we assume the validity of the first-order Born approximation; the spherical-wave FDP theorem can also be derived based upon the Rytov approximation by appropriately redefining Eqn. 3 [7].

Equation 6, coupled with a 3D interpolation method, can be used to implement a DF reconstruction algorithm. The 3D FBPP algorithm for plane-wave DT [8] can readily be extended to 3D spherical-wave DT [6] and is given by [6, 9]

$$a(\vec{r}) = \frac{1}{2} \int_{\phi=0}^{2\pi} d\phi \int_{\nu_m^2 + \nu_z^2 \leq \chi^2 \nu_0^2} \frac{|\nu_m|}{\chi^6 \nu'} [(1 - \chi^2) \nu' + \chi^2 \nu_0] \times M(\nu_m, \nu_z, \phi) e^{j2\pi(\nu'_m \xi - j2\pi \nu_\mu \eta + \nu'_z z)} d\nu_m d\nu_z, \quad (7)$$

where

$$\nu'_m = \frac{\nu_m}{\chi^2} \quad \nu'_z = \frac{\nu_z}{\chi^2} \quad \text{and} \quad \nu_\mu = -j(\sqrt{\nu_0^2 - \chi^2(\nu_m'^2 + \nu_z'^2)} - \nu_0).$$

### III. E-C RECONSTRUCTION ALGORITHM

In deriving the E-C reconstructions algorithms for spherical-wave DT, we will modify the procedure employed for the derivation of the plane-wave DT algorithms described in [4]. Let  $a(r, \theta, z)$  denote a 3D scattering object function in the cylindrical coordinate system. The X-ray transform,  $p(\xi, z, \phi_0)$ , of  $a(r, \theta, z)$  is defined as

$$p(\xi, z, \phi_0) = \int_{\eta=-\infty}^{\infty} a(r, \theta, z) d\eta, \quad (8)$$

where  $\phi_0$  is the projection angle,  $\xi = r \cos(\phi_0 - \theta)$  and  $\eta = -r \sin(\phi_0 - \theta)$ . Equation 8 states that  $p(\xi, z, \phi_0)$  is the geometrical projection of  $a(r, \theta, z)$  onto the  $\xi-z$  plane oriented at angle  $\phi_0$  about the  $z$  axis. Consequently,  $p(\xi, z, \phi_0)$  can be interpreted as a stack of 2D Radon transforms of  $a(r, \theta, z)$  along the  $z$  axis. The combination of a 2D Fourier transform with respect to  $\xi$  and  $z$  and a 1D Fourier series expansion with respect to  $\phi_0$  of  $p(\xi, z, \phi_0)$  is given by

$$P_k(\nu_a, \nu_z) = \frac{1}{2\pi} \int_{\phi_0=0}^{2\pi} \int_{\xi, z=-\infty}^{\infty} p(\xi, z, \phi_0) e^{-j2\pi \nu_a \xi - j2\pi \nu_z z - jk \phi_0} d\xi dz d\phi_0, \quad (9)$$

where the integer  $k$  is the angular frequency index with respect to  $\phi_0$ , and  $\nu_a$  and  $\nu_z$  are the continuous spatial frequencies conjugate to  $\xi$  and  $z$ , respectively. As a matter of convenience, we refer to  $P_k(\nu_a, \nu_z)$  as the "3D Fourier transform" of  $p(\xi, z, \phi_0)$ . Substituting Eqn. 8 into Eqn. 9 and carrying out the integral over  $\phi_0$  yields

$$P_k(\nu_a, \nu_z) = (-j)^k \int_{z=-\infty}^{\infty} e^{-j2\pi \nu_z z} dz \int_{\theta=0}^{2\pi} \int_{r=0}^{\infty} a(r, \theta, z) e^{-jk\theta} J_k(2\pi \nu_a r) r dr d\theta. \quad (10)$$

Again for convenience, we refer to  $M_k(\nu_m, \nu_z) = \frac{1}{2\pi} \int_0^{2\pi} M(\nu_m, \nu_z, \phi) e^{-jk\phi} d\phi$  as the "3D Fourier transform" of the modified data function. Using Eqn. 6 and noting that  $\xi = r \cos(\phi - \theta)$  and  $\eta = -r \sin(\phi - \theta)$  one can obtain

$$M_k(\nu_m, \nu_z) = \int_{z=-\infty}^{\infty} e^{-j2\pi \nu'_z z} dz \int_{\theta=0}^{2\pi} \int_{r=0}^{\infty} a(r, \theta, z) \times \left\{ \frac{1}{2\pi} \int_{\phi=0}^{2\pi} e^{2\pi \nu_\mu r \sin(\phi-\theta) - j(k\phi + 2\pi \nu'_m r \cos(\phi-\theta))} d\phi \right\} r dr d\theta, \quad (11)$$

where  $\nu_m^2 + \nu_z^2 \leq \chi^2 \nu_0^2$ . Carrying out the integral [10] in the curly brackets in Eqn. 11, one can re-express  $M_k(\nu_m, \nu_z)$  as

$$M_k(\nu_m, \nu_z) = (-j)^k \left[ \frac{\nu'_m + \nu_\mu}{\sqrt{\nu'^2_m - \nu_\mu^2}} \right]^k \int_{z=-\infty}^{\infty} e^{-j2\pi\nu'_z z} dz \\ \times \int_{\theta=0}^{2\pi} \int_{r=0}^{\infty} a(r, \theta, z) e^{-jk\theta} J_k(2\pi r \sqrt{\nu'^2_m - \nu_\mu^2}) r dr d\theta \quad (12)$$

where  $\nu_m^2 + \nu_z^2 \leq \chi^2 \nu_0^2$ .

Comparison of Eqns. 10 and 12 yields that for  $\nu_m^2 + \nu_z^2 \leq \chi^2 \nu_0^2$

$$P_k(\nu_a, \nu'_z) = [\gamma(\nu'_m, \nu'_z)]^k M_k(\nu_m, \nu_z), \quad (13)$$

where

$$\nu_a^2 = \nu'^2_m - \nu_\mu^2 \quad (14)$$

and

$$\gamma(\nu'_m, \nu'_z) = \frac{\sqrt{\nu'^2_m - \nu_\mu^2}}{\nu'_m + \nu_\mu}. \quad (15)$$

The explicit forms of this general relationship in Eqn. 13 are determined completely by the forms of the relationship between  $\nu_a$  and  $\nu_m$  implied in Eqn. 14. Equation 14 indicates that the condition  $\nu_m^2 + \nu_z^2 \leq \chi^2 \nu_0^2$  is equivalent to the condition  $\nu_a^2 + \nu_z^2 \leq \nu_0^2(1 + 1/\chi^2)$ . In order to determine  $\nu_m$  as a function of  $\nu_z$  and  $\nu_a$ , we must solve for the roots of the fourth-order equation

$$C_1 \nu'^4_m + C_2 \nu'^2_m + C_3 = 0, \quad (16)$$

where the coefficients  $C_i$  are given by

$$C_1 = (1 - \chi^2)^2,$$

$$C_2 = 2(1 - \chi^2)(2\nu_0^2 - \nu_a^2 - \frac{\nu_z^2}{\chi^2}) + 4\nu_0^2\chi^2,$$

and

$$C_3 = (2\nu_0^2 - \nu_a^2 - \frac{\nu_z^2}{\chi^2})^2 - 4\nu_0^2(\nu_0^2 - \frac{\nu_z^2}{\chi^2}).$$

The four roots of Eqn. 16 are given by

$$\nu'_{m1} = -\nu'_{m2} = \left[ \frac{-C_2 + \sqrt{C_2^2 - 4C_1C_3}}{2C_1} \right]^{1/2}, \quad (17)$$

and

$$\nu'_{m3} = -\nu'_{m4} = \left[ \frac{-C_2 - \sqrt{C_2^2 - 4C_1C_3}}{2C_1} \right]^{1/2}. \quad (18)$$

Let  $\nu_{mi} \equiv \nu'_{mi}\chi^2$ ,  $i = 1, 2, 3$ , and 4. For  $\nu_a^2 + \nu_z^2 \leq \nu_0^2(1 + 1/\chi^2)$ , the two roots  $\nu'_{m3}$  and  $\nu'_{m4}$  are complex-valued and therefore not physically meaningful. In the plane-wave case ( $\chi = 1$ ), there are only two roots that are given by [4]

$$\nu_{m1} = -\nu_{m2} = \nu_m = \left\{ (\nu_a^2 + \nu_z^2) \left[ 1 - \frac{\nu_a^2 + \nu_z^2}{4\nu_0^2} \right] - \nu_z^2 \right\}^{1/2}, \quad (19)$$

where  $\nu_a^2 + \nu_z^2 \leq 2\nu_0^2$ .

Therefore, for a given pair of  $\nu_a$  and  $\nu'_z$  satisfying  $0 \leq \nu_a^2 + \nu_z'^2 \leq \nu_0^2(1 + 1/\chi^2)$ ,  $P_k(\nu_a, \nu'_z)$  can be obtained from  $M_k(\nu_m, \nu_z)$  at  $\nu_{m1} = \nu_m$  and  $\nu_z$  as

$$\begin{aligned} P_k(\nu_a, \nu'_z) &= [\gamma(\nu'_{m1}, \nu'_z)]^k M_k(\nu_{m1}, \nu_z) \\ &= [\gamma(\nu'_m, \nu'_z)]^k M_k(\nu_m, \nu_z) \end{aligned} \quad (20)$$

and also from  $M_k(\nu_m, \nu_z)$  at  $\nu_{m2} = -\nu_m$  and  $\nu_z$  as

$$\begin{aligned} P_k(\nu_a, \nu'_z) &= [\gamma(\nu_{m2}, \nu'_z)]^k M_k(\nu_{m2}, \nu_z) \\ &= (-1)^k [\gamma(\nu'_m, \nu'_z)]^{-k} M_k(-\nu_m, \nu_z). \end{aligned} \quad (21)$$

The fact that there are two distinct ways to obtain  $P_k(\nu_a, \nu'_z)$  from the measured data can be explained by the existence of a double coverage of the scattering object Fourier space [7]. At a given measurement angle  $\phi$ , the spherical-wave FDP theorem relates the 2D Fourier transform of the modified measured data to the 3D Fourier transform of  $a(\vec{r})$  evaluated over a semi-ellipsoid oriented at angle  $\phi$ . As the measurement angle  $\phi$  is varied from 0 to  $2\pi$ , two overlapping coverages of the Fourier space are generated, with each coverage producing one of the relationships described by Eqns. 20 or 21.

Equations 20 and 21 yield two identical values of  $P_k(\nu_a, \nu'_z)$  when the measured data are consistent. However, when the measured data contain noise, Eqns. 20 and 21 will generally produce different values of  $P_k(\nu_a, \nu'_z)$ . These two values can be combined to obtain a final estimate of  $P_k(\nu_a, \nu'_z)$  that has a reduced noise level as

$$\begin{aligned} P_k^{(\omega)}(\nu_a, \nu'_z) &= \omega_k(\nu_m, \nu_z) [\gamma(\nu'_m, \nu'_z)]^k M_k(\nu_m, \nu_z) \\ &\quad + (1 - \omega_k(\nu_m, \nu_z)) (-1)^k [\gamma(\nu'_m, \nu'_z)]^{-k} M_k(-\nu_m, \nu_z), \end{aligned} \quad (22)$$

where  $\omega_k(\nu_m, \nu_z)$  is a generally complex-valued combination coefficient. The superscript " $\omega$ " indicates that  $P_k^{(\omega)}(\nu_a, \nu'_z)$  is obtained by use of a combination coefficient  $\omega_k(\nu_m, \nu_z)$ . If  $M_k(\nu_m, \nu_z)$  and  $M_k(-\nu_m, \nu_z)$  are interpreted as a random variables, then for a given  $\omega_k(\nu_m, \nu_z)$ , Eqn. 22 can be interpreted as an *estimation method* for obtaining the ideal sinogram. Because  $\omega_k(\nu_m, \nu_z)$  may be any complex-valued function of  $\nu_m, \nu_z$  and  $k$ , Eqn. 22, in effect, represents an infinite class of estimation methods. An estimate of  $p(\xi, z, \phi_0)$  can be obtained by taking the 3D inverse Fourier transform of  $P_k^{(\omega)}(\nu_a, \nu_z)$ . For a fixed value of  $z$ , the filtered back-projection (FBP) algorithm of X-ray CT can be employed to reconstruct the corresponding transverse slice of  $a(r, \theta, z)$  from  $p(\xi, z, \phi_0)$ . We refer to the *combination* of Eqn. 22 to estimate  $P_k^{(\omega)}(\nu_m, \nu_z)$  coupled with the 2D FBP algorithm to reconstruct transverse slices of  $a(r, \theta, z)$  as a *spherical-wave E-C reconstruction algorithm for 3D DT*.

#### IV. NUMERICAL RESULTS

We performed numerical simulations to demonstrate the spherical-wave E-C reconstruction algorithm. We considered a mathematical phantom comprised of two different (uniform) spheres whose 3D Fourier transforms were approximately bandlimited to a sphere of radius  $\sqrt{2}\nu_0$ . Our intention was not to test the validity of the weak scattering (Born) condition (see the Discussion Section), but rather to demonstrate that the spherical-wave E-C reconstruction algorithm can accurately reconstruct the scattering object function from weakly scattered data. We therefore employed Eqns. 3 and 6, along with the analytic expression for the 3D Fourier transform of a the spheres, to calculate noiseless samples of  $u_s(\xi, z, \phi)$  over a  $128 \times 128$  detector array at 128 view angles that were evenly spaced over  $360^\circ$ . In generating the simulation data, we assumed a scanning geometry with  $S=100$  (arbitrary units) and  $D=104.0816$  that, according to Eqn. 4, yields  $\chi = 0.7$ . In order to simulate the stochastic nature of noisy scattered data, we created a second data set,  $\hat{u}_s(\xi, z, \phi)$ , where the measured scattered data were treated as samples of an uncorrelated bivariate Gaussian stochastic process. When generating  $\hat{u}_s(\xi, z, \phi)$ , the mean and variance parameters describing the

real (imaginary) component of the stochastic process were set equal to the real (imaginary) values of the noiseless data  $u_s(\xi, z, \phi)$ . Therefore, at a given position  $(\xi, z, \phi)$  in the data space, the magnitude of noise contained in the real and imaginary components of  $\hat{u}_s(\xi, z, \phi)$  was proportional to the magnitude of the real and imaginary components of  $u_s(\xi, z, \phi)$ , respectively.

We reconstructed three transverse slices of the scattering object by use of the spherical-wave E-C algorithm specified by  $\omega_k(\nu_m, \nu_z) = \frac{1}{2}$  in Eqn. 22. It can readily be shown that when the data noise is uncorrelated,  $\omega = \frac{1}{2}$  is a statistically optimal choice in the sense that it minimizes the variance of the estimate  $P_k^{(\omega)}(\nu_a)$ , which in turn, results in a minimization of the global image variance<sup>2</sup> [4]. For more general noise models, it is, in principle, possible to derive other optimal forms for  $\omega_k(\nu_m, \nu_z)$ . The true images of the chosen transverse slices are shown in Fig. 3-(a). The images reconstructed from the noiseless data, shown in Fig. 3-(b), do not contain any artifacts and accurately represent the corresponding true slices shown in Fig. 3-(a). The same images reconstructed from the noisy data set are shown in Fig. 3-(c). Although noisy in appearance, the images are not distorted which confirms that the spherical-wave E-C algorithm are numerically stable. Out of curiosity, we also reconstructed the same transverse slices by use of our previously developed plane-wave E-C reconstruction algorithm (that assumes the measurement geometry corresponds to  $\chi = 1$ ) and the noiseless data set. The reconstructed images, shown in Fig. 4, clearly contain artifacts and distortions. This numerically demonstrates the importance of properly accounting for the wavefield curvature in 3D DT.

## V. DISCUSSION

Previously, we developed a novel class of reconstruction algorithms for 3D DT using plane-wave sources. These algorithms, referred to as plane-wave E-C reconstruction algorithms, had a significant computational advantage over the conventional 3D FBPP algorithm, and unlike the 3D DF method, did not require an explicit 3D interpolation in the Fourier space of the scattering object.

The use of a plane-wave source may not be feasible in many experimental situations, and it may be more convenient to interrogate the scattering object using a diverging spherical wave that is produced by a point source. In this work, we have developed a class of spherical-wave E-C reconstruction algorithms for DT using spherical-wave sources and measurement geometries that satisfy the paraxial approximation [7]. The spherical-wave E-C reconstruction algorithms can be viewed as generalizations of the plane-wave E-C reconstruction algorithms, and reduce to the plane-wave E-C algorithms in the special case  $\chi = 1$ . The spherical-wave E-C reconstruction algorithms possess the same advantages as their plane-wave counterparts. For example, to reconstruct an  $N^3$  image volume the spherical-wave E-C algorithm requires  $\sim N^3 \log N$  numerical operations while the spherical-wave FBPP algorithm described by Eqn. 7 would require  $\sim N^4 \log N$  numerical operations. Unlike DF methods, the spherical-wave E-C algorithms do not require an explicit 3D interpolation in the Fourier space of the scattering object.

The spherical-wave E-C reconstruction algorithms have been developed using the first-order Born (or Rytov) weak scattering approximation. In certain applications, the weak scattering approximation may not be valid and the reconstructed image may contain artifacts. However, the spherical-wave E-C algorithms provide a natural framework for the incorporation of higher-order scattering perturbation approximations [11–13] into the algorithms.

## ACKNOWLEDGEMENTS

This work was funded in part by a Department of Defense Breast Cancer Research Concept Award (DAMD 17-01-1-0502).

## REFERENCES

- [1] S. Norton and T. Vo-Ding, "Diffraction tomographic imaging with photon density waves: An explicit solution," *Journal of the Optical Society of America A*, vol. 15, pp. 2670–2677, 1998.

<sup>2</sup>The global image variance is equal to the local variance of an image at a point summed over all points in image space.

- [2] N. Jayshree, G.K. Datta, and R.M. Vasu, "Optical tomographic microscope for quantitative imaging of phase objects," *Applied Optics*, vol. 39, pp. 277–283, 2000.
- [3] M. Andre, P. Martin, G.P. Otto, L.K. Olson, T.K. Barrett, and B.A. Spivey, "A new consideration of diffraction computed tomography for breast imaging: Studies in phantoms and patients," *Acoustical Imaging*, vol. 21, pp. 379–390, 1995.
- [4] M. Anastasio and X. Pan, "Computationally efficient and statistically robust image reconstruction in 3D diffraction tomography," *Journal of the Optical Society of America A*, vol. 17, pp. 391–400, 2000.
- [5] M. Anastasio and X. Pan, "Numerically robust minimal-scan reconstruction algorithms for diffraction tomography via. radon transform inversion," *International Journal of Imaging Systems and Technology* (In press), 2002.
- [6] Z. Lu, "Multidimensional structure diffraction tomography for varying object orientation through generalised scattered waves," *Inverse Problems*, vol. 1, pp. 339–356, 1985.
- [7] A.J. Devaney, "Generalized projection-slice theorem for fan-beam diffraction tomography," *Ultrasonic Imaging*, vol. 7, pp. 264–275, 1985.
- [8] A.J. Devaney, "A filtered backpropagation algorithm for diffraction tomography," *Ultrasonic Imaging*, vol. 4, pp. 336–350, 1982.
- [9] M. Anastasio, *Development and Analysis of Image Reconstruction Algorithms in Diffraction Tomography*, Ph.D. thesis, The University of Chicago, 2001.
- [10] Charles E. Metz and X. Pan, "A unified analysis of exact methods of inverting the 2-d exponential radon transform, with implications for noise control in SPECT," *IEEE Transactions on Medical Imaging*, vol. 14, pp. 643–658, 1995.
- [11] Zhen-Qiu Lu and Yan-Yun Zhang, "Acoustical tomography based on the second-order Born transform perturbation approximation," *IEEE Transactions on Ultrasonics, Ferroelectrics, and Frequency Control*, vol. 43, pp. 296–302, 1996.
- [12] G.A. Tsihrintzis and A.J. Devaney, "Higher-order (nonlinear) diffraction tomography: Reconstruction algorithms and computer simulation," *IEEE Transactions on Image Processing*, vol. 9, pp. 1560–1572, 2000.
- [13] G.A. Tsihrintzis and A.J. Devaney, "Higher order (nonlinear) diffraction tomography: Inversion of the Rytov series," *IEEE Transactions on Information Theory*, vol. 46, pp. 1748–1761, 2000.

#### FIGURE CAPTIONS

Fig. 1. The classical scanning geometry of spherical-wave 3D DT. A spherical-wave is incident at angle  $\phi$ , and the scattered field is measured in the  $\xi$ - $z$  plane positioned at  $\eta = D$ . The measurement angle  $\phi$  is varied from 0 to  $2\pi$ .

Fig. 2. A plot of  $\nu_m$  as a function of  $\nu_z$  and  $\nu_a$  as described by Eqn. 17. The plot was generated using  $\chi = 0.7$  and  $\nu_0 = \pi$ .

Fig. 3. (a) True slices through the numerical phantom. Transverse slices reconstructed from (b) noiseless and (c) noisy data using a spherical-wave E-C reconstruction algorithm.

Fig. 4. Transverse slices reconstructed from the spherical-wave data function ( $\chi = 0.7$ ) using a plane-wave DT reconstruction algorithm. As expected, the images contain distortions.



## FIGURES

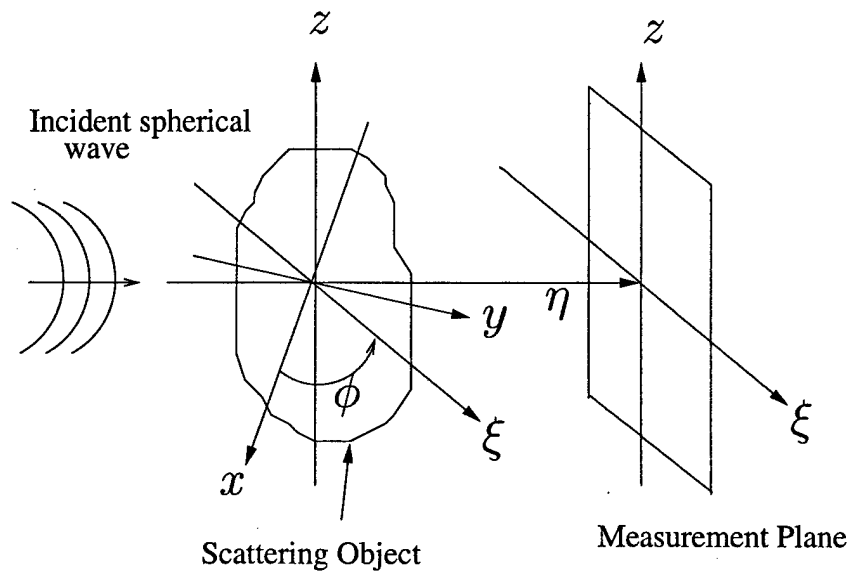


Fig. 1.

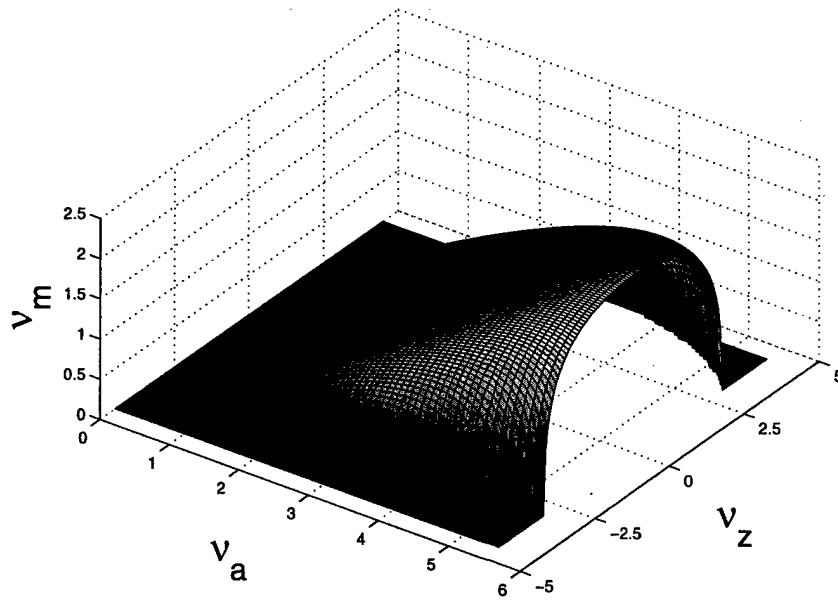
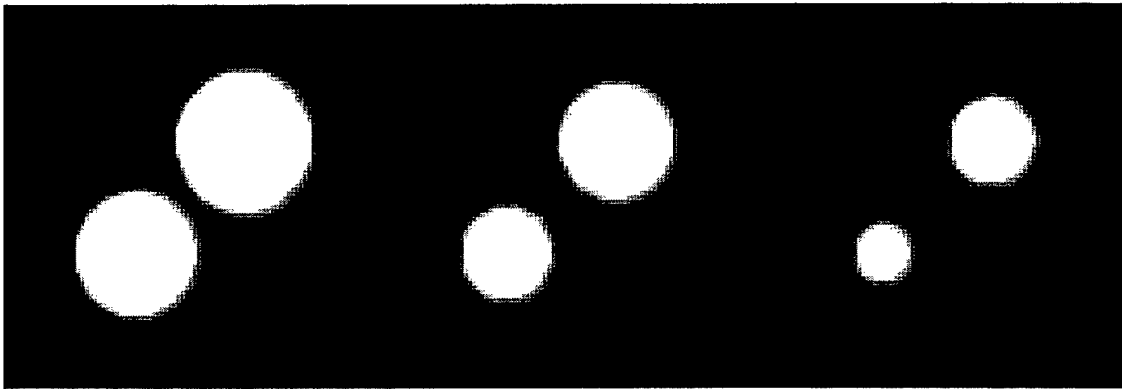
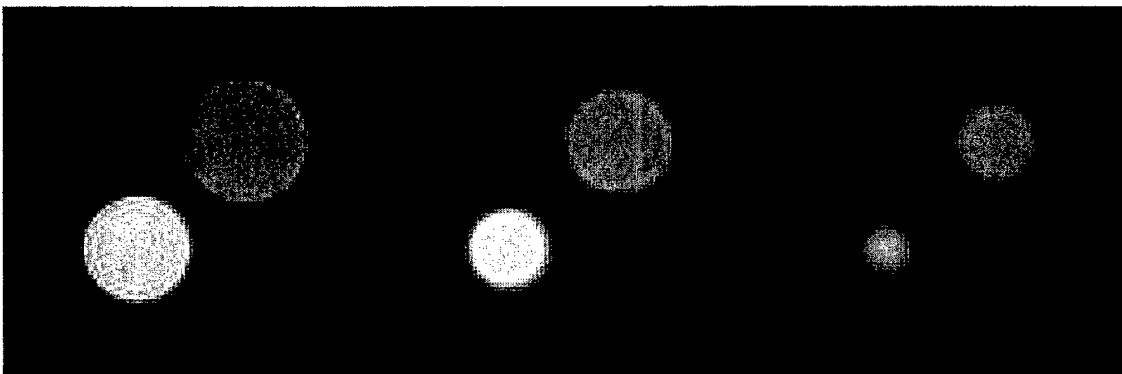


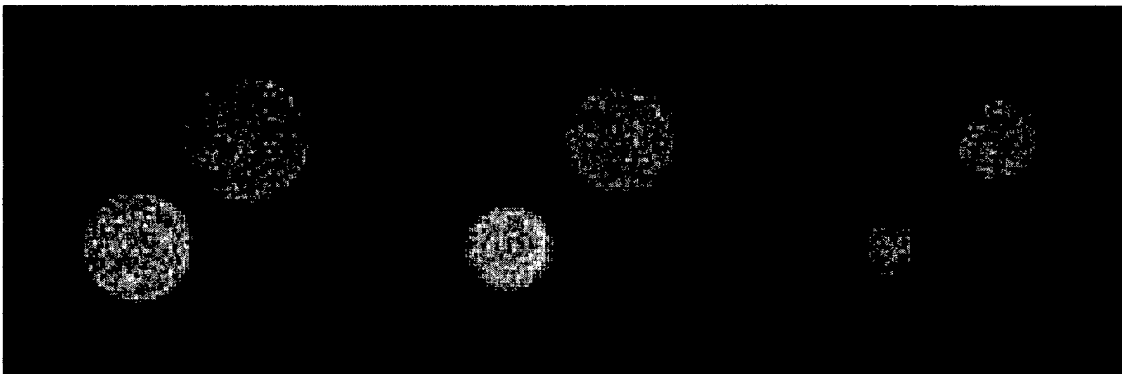
Fig. 2.



(a)



(b)



(c)

Fig. 3.

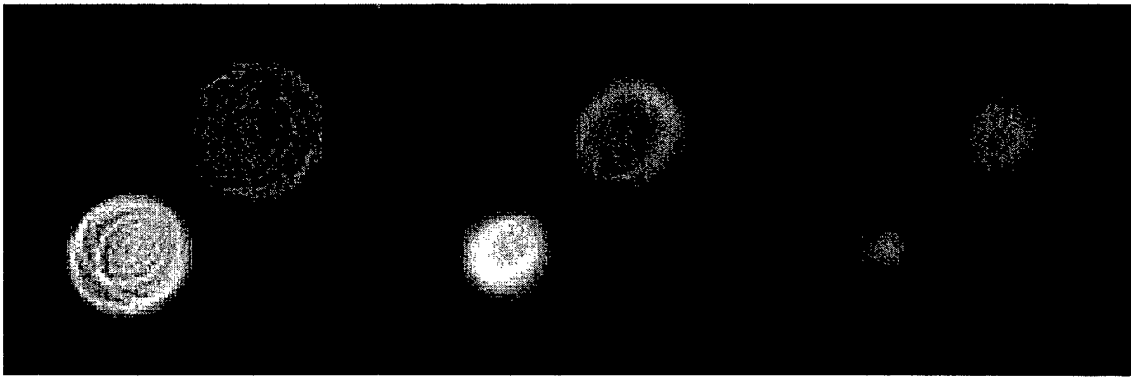


Fig. 4.

# **Data Redundancy and Reduced-Scan Reconstruction in Reflectivity Tomography**

Xiaochuan Pan, Yu Zou, and Mark A. Anastasio<sup>†</sup>

Department of Radiology, The University of Chicago, Chicago, IL 60637

<sup>†</sup>Pritzker Institute of Medical Engineering, Illinois Institute of Technology, Chicago, IL 60616

March, 2002

## **Corresponding Author:**

Xiaochuan Pan, Ph.D.

Department of Radiology, MC-2026

The University of Chicago Medical Center

5841 S. Maryland Avenue

Chicago, IL 60637

(773)702-1293 (Voice)

(773)702-5986 (Fax)

E-mail: [xpan@midway.uchicago.edu](mailto:xpan@midway.uchicago.edu)

## Abstract

In reflectivity tomography, conventional reconstruction approaches require that measurements be acquired at view angles that span a full angular range of  $2\pi$ . It is often, however, advantageous to reduce the angular range over which measurements are acquired, which can, for example, minimize artifacts due to movements of the imaged object. Moreover, in certain situations it may not be experimentally possible to collect data over a  $2\pi$  angular range. In this work, we investigate the problem of reconstructing images from reduced-scan data in reflectivity tomography. By exploiting symmetries in the data function of reflectivity tomography, we *heuristically* demonstrate that an image function can be uniquely specified by reduced-scan data that correspond to measurements taken over an angular interval (possibly disjoint) that spans at least  $\pi$  radians. We also identify sufficient conditions that permit for a stable reconstruction of image boundaries from reduced-scan data. Numerical results in computer-simulation studies indicate that images can be reconstructed accurately from reduced-scan data.

**EDICS Category: 3-TOMO (Computer tomography)**

## 1 Introduction

Reflectivity tomography has been applied to numerous biomedical [1,2] and non-destructive testing [3] imaging problems. In two-dimensional (2D) reflectivity tomography [4, 5], a weakly reflecting object that is immersed in an acoustically homogeneous background medium is illuminated with infinitesimally short ultrasonic pulses, and the concomitant reflected signals are measured as functions of time at each of the multiple source locations. The task in reflectivity tomography is to reconstruct from such measured data a function describing the reflectivity distribution within the scattering object<sup>1</sup>.

In reflectivity tomography, an imaging configuration that acquires data over the complete angular interval of  $2\pi$  is referred to as a *full-scan* configuration. Norton derived [4] an analytic algorithm for reconstructing the object function from data acquired with a full-scan configuration. In tomographic imaging, however, it is often desirable to minimize the angular range over which data are acquired. When ionizing radiation is employed, this can reduce the radiation dose that is delivered to the subject during the imaging process. An advantage of reducing the scanning angle, which is also relevant to biomedical imaging applications employing non-ionizing radiation, is that the time needed to collect data is reduced, thus diminishing image artifacts and distortions created by movements of

---

<sup>1</sup>For simplicity, we refer to the object's reflectivity function as the object function.

the object during the imaging process. Furthermore, in certain situations it may not be experimentally possible to collect data over a full angular range of  $2\pi$ .

An imaging configuration that acquires data over an angular interval  $\Phi$ , where  $\pi \leq \Phi < 2\pi$ , is referred to as a *reduced-scan* configuration. It has been shown that one can accurately reconstruct images from data acquired with reduced-scan configurations in tomographic imaging modalities including fan-beam computed tomography (CT) [6] and single-photon emission computed tomography (SPECT) [7, 8]. However, it remains unclear whether an accurate object function can be reconstructed from reduced-scan data in reflectivity tomography.

In this work, we investigate the problem of image reconstruction from reduced-scan data in reflectivity tomography. A potato-peeler perspective<sup>2</sup> is proposed for identifying data symmetries in reflectivity tomography. Using the identified data symmetries, we *heuristically* demonstrate that data acquired with reduced-scan configurations in reflectivity tomography are, in principle, sufficient to specify the object function. We also apply results from microlocal analysis [10] to investigate the stability of reconstructing image boundaries from reduced-scan data in reflectivity tomography.

Norton's algorithm [4], which can be applied only to full-scan data, cannot accurately reconstruct images from reduced-scan data. Instead, we propose to use the expectation maximization (EM) algorithm [11] for reconstruction of the object function from reduced-scan data. Using computer-simulation studies, we evaluate the numerical properties of images that are reconstructed from reduced-scan data. The results of these studies indicate that, under practically relevant conditions, images can be reconstructed accurately from reduced-scan data. In particular, for reflecting objects and scanning configurations that may arise in realistic experiments, numerically accurate images can be reconstructed from reduced-scan data acquired over, e.g., an angular interval of only  $\pi$ .

## 2 Data Function in Reflectivity Tomography

In this section, we briefly discuss the data function in reflectivity tomography and summarize Norton's algorithm [4] for image reconstruction from full-scan data. Let  $f(r, \theta)$  denote a two-dimensional (2D), bounded, and non-negative object function with compact support on the disk of radius  $R_f$  centered at the origin, for some fixed real number  $R_f > 0$ . As shown

---

<sup>2</sup>The potato-peeler perspective is conceptually similar to the so-called "layer-stripping" method for solving the Helmholtz equation, e.g., in impedance imaging [9], in the sense that the object function is determined layer by layer. However, the mathematical formulation of the potato-peeler perspective differs entirely from that of the existing "layer-stripping" method [9]. We are currently developing a mathematical formulation for the potato-peeler perspective for reflectivity tomography and will report such results elsewhere.

in Fig. 1, the object function is embedded in an acoustically homogeneous background medium, and an omni-directional point source-receiver is located at the polar coordinates  $(R, \phi + \pi)$  on a circular source-receiver trajectory curve  $\mathcal{C}$  that encloses the object function. At time  $t = 0$ , an infinitesimally short pulse of sound is emitted from the point source, and the wavefield that is backscattered (i.e., reflected) from the reflecting object is measured at the source location as a function of time.

The measured data can, under certain conditions [5], be interpreted as a set of line integrals of  $f(r, \theta)$  defined over all circular arcs (with varying radii) that are centered at a source-receiver location  $(R, \phi + \pi)$ , where  $R_f \leq R$ . If this transmit/receive process is repeated for all points on  $\mathcal{C}$ , multiple sets of these line integrals are obtained. These line integrals can be expressed mathematically as

$$g(\xi, \phi) = \int_0^{2\pi} d\theta \int_0^{R_f} dr r f(r, \theta) \delta(\sqrt{R^2 + r^2 - 2Rr \cos(\phi - \theta)} - R - \xi), \quad (1)$$

where  $\xi \in [-R, R]$ , and the Dirac  $\delta$  function restricts the integration over a circular arc with a radius  $R + \xi > 0$  and centered at the point  $(R, \phi + \pi)$  on the curve  $\mathcal{C}$ . The reconstruction problem in reflectivity tomography is to determine the object function  $f(r, \theta)$  from knowledge of the data function  $g(\xi, \phi)$ .

In full-scan reflectivity tomography, because  $g(\xi, \phi)$  is measured for all  $\phi \in [0, 2\pi)$ , one can calculate its Fourier series expansion coefficient as

$$g_n(\xi) = \frac{1}{2\pi} \int_0^{2\pi} d\phi g(\xi, \phi) e^{-jn\phi}. \quad (2)$$

The object function can be expressed as a Fourier series,

$$f(r, \theta) = \sum_{n=-\infty}^{\infty} f_n(r) e^{jn\theta}, \quad (3)$$

where  $f_n(r) = \frac{1}{2\pi} \int_0^{2\pi} d\theta f(r, \theta) e^{-jn\theta}$ . Norton [4] showed that  $f_n(r)$  (i.e., the object function) can be determined from knowledge of  $g_n(\xi)$  (i.e., the full-scan data  $g(\xi, \phi)$ ) as

$$f_n(r) = \int_0^\infty dz z \frac{J_n(rz)}{J_n(Rz)} \left[ \int_{-R}^R d\xi \xi \frac{g_n(\xi) J_0(\rho z)}{2\pi \rho} \right], \quad (4)$$

where  $\rho = R + \xi$  and  $J_n(\cdot)$  is the  $n$ th-order Bessel function of the first kind. Therefore, Eqns. 2, 3, and 4 provide a recipe for reconstruction of the object function from full-scan data.

### 3 Data Symmetry and Reduction of Scanning Angle

Data symmetries have been exploited to demonstrate whether accurate object functions can be reconstructed from reduced-scan data in other tomographic imaging modalities

(e.g., fan-beam CT [6] and SPECT [7,8]). Below, we use the Radon transform of an object function as a data function to illustrate a data symmetry. The Radon transform of an object function  $f(r, \theta)$  is defined as

$$p(\xi, \phi) = \int_0^{2\pi} d\theta \int_0^{R_f} dr r f(r, \theta) \delta(\xi - r \cos(\phi - \theta)), \quad (5)$$

where  $\xi \in [-R_f, R_f]$ , and  $\phi$  is the projection angle. A symmetry of the Radon transform exists because its values at conjugate views are identical, i.e.,

$$p(\xi, \phi) = p(-\xi, \phi + \pi). \quad (6)$$

Such a symmetry suggests that the full-scan Radon transform contains redundant information. Knowledge of the Radon transform acquired over  $[0, \pi)$  can be used for reconstructing an image exactly because knowledge of the Radon transform corresponding to the un-measured angular intervals is fully specified by Eqn. 6. Inspection of Eqn. 1 indicates that the data function  $g(\xi, \phi)$  in reflectivity tomography possesses no symmetry analogous to that of the Radon transform in Eqn. 6. However, we reveal below that the data function  $g(\xi, \phi)$  does admit symmetries and that such symmetries can be exploited to identify redundant information in full-scan data in reflectivity tomography.

### 3.1 Potato-Peeler Perspective for Reflectivity Tomography

Although the data function in Eqn. 1 does not admit a simple symmetry analogous to that of the Radon transform in Eqn. 6, the fact that the imaging transform in Eqn. 1 is linear and that  $f(r, \theta)$  has a compact support can facilitate the explicit identification of data symmetries in reflectivity tomography. We generalize the potato-peeler perspective, which was developed previously for analyzing data symmetry in SPECT [12], to investigate data symmetries in reflectivity tomography. It should be emphasized that this perspective, to be presented below, is not intended as a mathematically stable and computationally practical reconstruction algorithm. Instead, it is used only for *heuristically* revealing data symmetries in reflectivity tomography.

Without loss of generality, as shown in Fig. 2, we assume that the non-zero support of  $f(r, \theta)$  is a disk of radius  $R_f$  centered at the origin, i.e.,  $f(r, \theta) \neq 0$  for  $r \leq R_f$  and  $f(r, \theta) = 0$  for  $r > R_f$ . (The procedures and discussion to be presented below can, however, readily be modified to address any compactly supported object functions.) We use  $L(\xi, \phi)$  to denote the circular integrating line in Eqn. 1.

At a given view angle  $\phi_0$ , one can identify a value  $\xi_{max} \geq 0$  such that  $g(\xi_{max}, \phi_0) \neq 0$  and  $g(\xi, \phi_0) = 0$  for  $\xi > \xi_{max}$ . The assumption on the support compactness of  $f(r, \theta)$  indicates that

$$\xi_{max} = R_f. \quad (7)$$



Therefore, one can determine  $R_f$  from knowledge of  $\xi_{max}$ . Conceptually, we treat  $f(r, \theta)$  as a collection of weighted 2D Dirac delta functions.<sup>3</sup> Because the integrating line  $L(\xi_{max}, \phi_0)$  intersects  $f(r, \theta)$  only at the single point  $(R_f, \phi_0)$  (i.e., point  $B$  in Fig. 2a), Eqn. 1 reduces to

$$g(\xi_{max}, \phi_0) = f(R_f, \phi_0). \quad (8)$$

On the other hand, at the conjugate view angle  $\phi_0 + \pi$ , one can identify a same value  $\xi_{max} \geq 0$  such that  $g(-\xi_{max}, \phi_0 + \pi) \neq 0$  and  $g(-\xi, \phi_0 + \pi) = 0$  for  $\xi > \xi_{max}$ . In this situation, the integrating line  $L(-\xi_{max}, \phi_0 + \pi)$  also intersects only at a single point  $(R_f, \phi_0)$  (i.e., point  $B$  in Fig. 2a) on the outermost edge of the support. Again, as a result, Eqn. 1 reduces to

$$g(-\xi_{max}, \phi_0 + \pi) = f(R_f, \phi_0). \quad (9)$$

Therefore, the object function  $f(r, \theta)$  at the outermost point  $(R_f, \phi_0)$  (i.e., point  $B$  in Fig. 2a) can be specified completely by either one of the two measurements  $g(\xi_{max}, \phi_0)$  and  $g(-\xi_{max}, \phi_0 + \pi)$ .

The component of  $f(r, \theta)$  corresponding to the point  $(R_f, \phi_0)$  produces (via. Eqn. 1) a component of the data function given by

$$g_B(\xi, \phi) = g(\xi_{max}, \phi_0)I(\xi, \phi), \quad (10)$$

where  $I(\xi, \phi)$  is an indicator function defined as  $I(\xi, \phi) = 1$  for  $\xi = [R_f^2 + R^2 - 2R_f R \cos(\phi_0 - \phi)]^{\frac{1}{2}} - R$  and  $I(\xi, \phi) = 0$  otherwise. As shown in Fig. 2b, the function  $I(\xi, \phi)$  specifies the loci of points in the data space that receive a contribution when  $f(r, \theta)$  in Eqn. 1 is replaced by  $f(R_f, \phi_0) \frac{\delta(r-R_f)\delta(\theta-\phi_0)}{r}$ . From  $g(\xi, \phi)$  and  $g_B(\xi, \phi)$ , one can obtain a new data function as

$$\hat{g}(\xi, \phi) = g(\xi, \phi) - g_B(\xi, \phi), \quad (11)$$

which contains no contributions from point  $B$  in the object function. In a similar manner, all points (e.g., points  $A$  and  $C$ ) on the outermost edge of  $f(r, \theta)$  can be determined and “peeled away”, and their contributions to the data function  $g(\xi, \phi)$  can be removed, each time forming a new data function. The next set of points at the interior of the object function will be exposed. By the same procedure, the next layer of the object function can be determined and “peeled away”, and their contributions to the new data function can be removed. By repeating this procedure, one can determine  $f(r, \theta)$  by completely peeling, layer by layer, the object function away.

<sup>3</sup>i.e.,  $f(r, \theta) = \int_0^{2\pi} d\theta' \int_0^{R_f} dr' r' f(r', \theta') \frac{\delta(r-r')\delta(\theta-\theta')}{r'}$ .

### 3.2 Reduction of Scanning Angle

From Eqns. 8 and 9, one can readily identify a symmetry of the data function as

$$g(\xi_{max}, \phi_0) = g(-\xi_{max}, \phi_0 + \pi). \quad (12)$$

Furthermore, using the potato-peeler perspective described above, one can identify a symmetry of  $\hat{g}(\xi, \phi)$  as

$$\hat{g}(\xi_m, \phi) = \hat{g}(-\xi_m, \phi + \pi), \quad (13)$$

where  $\hat{g}(\xi_m, \phi) \neq 0$  and  $\hat{g}(-\xi_m, \phi + \pi) \neq 0$  for  $0 \leq \xi_m \leq \xi_{max}$ , and  $g(\xi, \phi) = 0$  for  $|\xi| > \xi_m$ . The symmetry condition in Eqn. 13 indicates that any point of the object function can be specified by the values of a (processed) data function  $\hat{g}(\xi, \phi)$  at conjugate views. As a result, the potato-peeler perspective suggests that the object function may be specified by knowledge of the measured data  $g(\xi, \phi)$  available over  $\phi \in [0, \pi)$ . We refer to a scanning configuration that acquires  $g(\xi, \phi)$  over  $\phi \in [0, \pi)$  as the *short-scan* configuration. More generally, the potato-peeler perspective indicates that an object function may be specified by knowledge of data  $g(\xi, \phi)$  measured over  $\phi \in \Phi$ , where  $\Phi$  is any proper subset of  $[0, 2\pi)$  such that  $\phi' \in \Phi$  OR  $\phi' + \pi \in \Phi$ , for all  $\phi' \in [0, \pi)$ . We refer to a scanning configuration that acquires data at  $\phi \in \Phi$  as a  $\pi$ -scheme configuration [8]. Obviously, the short-scan configuration can be viewed as a special case of the  $\pi$ -scheme configurations. The data symmetries above indicate that full-scan data in reflectivity tomography contain redundant information that can be exploited for reducing the angular range over which measurements need to be acquired.

By use of the potato-peeler perspective, it was revealed heuristically above that an object function  $f(r, \theta)$  in reflectivity tomography can be specified uniquely by knowledge of short-scan or  $\pi$ -scheme data. This is consistent with the result of an analysis of a family of Radon transforms over circles [13]. One can use principles from microlocal analysis [10, 14], as described in Appendix A, to derive theoretically sufficient conditions for stable reconstruction of boundaries (more generally, singularities) in the object function. One of the sufficient conditions suggests that all boundaries in the object function can stably be reconstructed from data acquired over  $[0, 3\pi/2)$ . Also, as discussed in Appendix A, depending upon the boundary locations within an object function, it is theoretically possible that all boundaries can stably be recovered from short-scan or  $\pi$ -scheme data. More important, as the results of numerical studies below show, under realistic practical conditions (e.g., in the presence of data noise), images reconstructed from short-scan or  $\pi$ -scheme data generally appear to be comparable to those obtained from full-scan data.

## 4 Results

Using simulation studies, we numerically investigated the accuracy of images reconstructed from reduced-scan data in reflectivity tomography.

### 4.1 Data and Reconstruction Algorithm

We used three different numerical phantoms, which are shown in Fig. 3, to generate simulated measurement data corresponding to the imaging transform in Eqn. 1. The phantom in the left panel of Fig. 3 is comprised of three 2D Gaussian functions, representing a smooth object function containing no boundaries, whereas the phantoms in the middle and right panels of Fig. 3 contain boundaries and complex structures. We refer to the two phantoms in the left and middle panels of Fig. 3 as the Gaussian phantom and the ellipse phantom, respectively. The phantom on the right panel, known as the Shepp-Logan phantom, is widely used in the medical imaging community. When we simulated the measured data, the phantoms were centered at the origin of the  $x$ - $y$  coordinate system, which was also the center of the circular source-receiver trajectory (see Fig. 1). The matrix size of the reconstructed images is 128x128.

It remains unclear whether analytic algorithms exist for accurate reconstruction of images from reduced-scan data. In this work, we use the EM algorithm [11] for image reconstruction. For notational convenience, let  $x = (r, \theta)$  and  $y = (\xi, \phi)$  denote 2D vectors in the image and data spaces, respectively. Equation 1 can then be expressed as

$$g(y) = \int_{D_x} dx h(x, y) f(x) \quad \forall y \in D_y, \quad (14)$$

where the real and non-negative functions  $g(y)$  and  $f(x)$  denote the data and object functions that are supported on the domains  $D_y$  and  $D_x$ , respectively. (For instance, for a short-scan configuration,  $D_y = \{y \mid -R \leq \xi \leq R, \phi \in \pi\}$ .) The kernel  $h(x, y)$  of the imaging transformation is given by

$$h(x, y) = \delta \left( \left[ r^2 + R^2 - 2rR \cos(\phi - \theta) \right]^{\frac{1}{2}} - R - \xi \right). \quad (15)$$

We use

$$f^{(n+1)}(x) = \frac{f^{(n)}(x)}{\int_{D_y} dy h(x, y)} \int_{D_y} dy \frac{h(x, y) g(y)}{\int_{D_x} dx h(x, y) f^{(n)}(x)} \quad (16)$$

as the estimate of the object function, where  $n$  is the number of iterations. The initial image  $f^{(0)}(x, y)$  is often chosen as a non-zero constant function. The EM algorithm has been shown to yield the maximization-likelihood solution to Eqn. 14 when the data function  $g(y)$  contain Poisson noise [15]. From a practical point of view, the EM algorithm is easy

to implement because it involves only forward and backward transformations between the image and data spaces. In our work, in an attempt to enhance the computational efficiency, we utilized an ordered-subsets [16] implementation of the EM algorithm.

## 4.2 Reconstruction of Smooth Object Functions

We first investigated the accuracy of reconstructed images of a smooth object function containing no boundaries. To do so, we used the Gaussian phantom in Fig. 3 to generate three noiseless data sets containing measurements over the angular ranges of  $[0, \pi/2)$ ,  $[0, 3\pi/4)$ , and  $[0, \pi)$ . The radius of the source-receiver trajectory was taken to be  $R = r_0$ , where  $r_0$  represents half of the image-array size. From the three data sets, we reconstructed images and, in each case, calculated a difference image between the reconstructed image and the Gaussian phantom.

In Fig. 4, we display profiles through the three difference images at  $x = 64$  and  $y = 44$  obtained from the  $[0, \pi/2)$ ,  $[0, 3\pi/4)$ , and  $[0, \pi)$  data sets, respectively. It can be observed that the difference profiles obtained from the  $[0, \pi)$  data set are almost zero. Because the Gaussian phantom studied has no obvious symmetries, such an observation appears to suggest that an accurate image of a smooth object function can be reconstructed from short-scan data.<sup>4</sup> It can also be seen in Fig. 4 that the difference profiles calculated from the  $[0, \pi/2)$  and  $[0, 3\pi/4)$  data sets are significantly different from zero, suggesting that accurate images cannot be reconstructed from data acquired over angular intervals less than  $\pi$ .

## 4.3 Reconstruction of Images Containing Boundaries

For the ellipse and Shepp-Logan phantoms that contain boundaries, we generated simulated data sets containing measurements over angular ranges  $[0, \pi/2)$ ,  $[\pi, 2\pi)$ ,  $[\pi/3, 2\pi/3] \cup [\pi, 4\pi/3] \cup [5\pi/3, 2\pi]$ ,  $[0, 3\pi/2)$ , and  $[0, 2\pi)$ , as shown in Fig. 5. The second and third configurations correspond to short-scan and  $\pi$ -scheme configurations, whereas the last configuration is the full-scan configuration. For each of the ellipse and Shepp-Logan phantoms and for each of the scanning configurations in Fig. 5, we generated two sets of noiseless data by use of two circular source-receiver trajectories with different radii. Using these noiseless data as the means, we generated the corresponding noisy data by adding Gaussian noise.

In Fig. 6, we display images reconstructed from noiseless and noisy data acquired over  $[0, \pi/2)$  (see the configuration in the far left panel of Fig. 5). Clearly, all of the images contain significant distortions, suggesting that images cannot be reconstructed accurately

---

<sup>4</sup>In reflectivity tomography, the stable reconstruction of smooth components of an object function can be deduced by exploiting a correspondence between the Sobolev wavefront sets of the data and object functions [17, 18].

from data acquired over an angular interval less than  $\pi$ . This observation is consistent with that for smooth images above.

For the ellipse phantom, we show in Figs. 7 and 8 images reconstructed from data acquired over angular ranges  $[\pi, 2\pi)$ ,  $[\pi/3, 2\pi/3] \cup [\pi, 4\pi/3] \cup [5\pi/3, 2\pi]$ ,  $[0, 3\pi/2)$ , and  $[0, 2\pi)$ . The radii of the source-receiver trajectory for obtaining the results in Figs. 7 and 8 were  $r_0$  and  $3r_0$ , respectively, where  $r_0$  represents half of the image-array size. Images reconstructed from noiseless data are shown in the first columns in Figs. 7 and 8. The overall visual quality of the noiseless images reconstructed from short-scan or  $\pi$ -scheme data appears comparable to that obtained from full-scan data. In particular, for the case of  $R = 3r_0$  (Fig. 8), which may correspond to a typical realistic experimental geometry, the noiseless images reconstructed from the short-scan and  $\pi$ -scheme data appear to be virtually identical to that reconstructed from the full-scan data. Images in the second, third, and fourth columns in Figs. 7 and 8 were reconstructed from data containing Gaussian noise with standard deviations of 1, 2, and 4, respectively. These noisy images appear distinct, but are not qualitatively different (for a given noise level). Differences in the statistical characteristics of the images (i.e. the appearance of the image noise) are to be expected because the same reconstruction algorithm is applied to different noisy data sets. Furthermore, the full-scan data contain redundant information that is not present in the short-scan or  $\pi$ -scheme data, which serves to effectively average out certain components of the data noise.

For the Shepp-Logan phantom, we show images in Figs. 9 and 10 reconstructed from data acquired over angular ranges  $[\pi, 2\pi)$ ,  $[\pi/3, 2\pi/3] \cup [\pi, 4\pi/3] \cup [5\pi/3, 2\pi]$ ,  $[0, 3\pi/2)$ , and  $[0, 2\pi)$ , respectively. The radii of the source-receiver trajectory for obtaining the results in Figs. 9 and 10 were  $r_0$  and  $3r_0$ , respectively. Images reconstructed from noiseless data are shown in the first columns of Figs. 9 and 10, and images in the second, third, and fourth columns in Figs. 9 and 10 were reconstructed from data containing Gaussian noise with standard deviations of 1, 2, and 4, respectively. Again, for images in Figs. 9 and 10, one can make observations similar to those for images in Figs. 7 and 8. The overall visual quality of the images reconstructed from short-scan or  $\pi$ -scheme data appears comparable to that obtained from the full-scan data, and images reconstructed from various noisy data sets appear qualitatively similar (for a given noise level).

According to microlocal analysis [10], certain image boundaries may not theoretically be reconstructed stably from short-scan or  $\pi$ -scheme data. For example, in the short-scan case in which the source-receiver trajectory is within the lower half plane (see the configuration in the second panel in Fig. 5), the microlocal analysis suggests that vertical boundaries in the ellipse phantom that reside in the upper half plane cannot be reconstructed stably. This is because the normal vectors of such vertical boundaries do not intersect the source-receiver trajectory in the lower half plane. From the noiseless image in the far left panel of

the first row in Fig. 7, one can see artifacts near the vertical boundaries of the square region in the upper half. However, it is interesting to observe that such artifacts do not appear to be prominent. Furthermore, as the radius of the source-receiver trajectory increases, such artifacts become almost undetectable numerically, as confirmed by the virtually artifact-free noiseless images in the far left panels of the first and second rows in Fig. 8 for the case  $R = 3r_0$ .

The boundaries in the images in the far left panels of the third rows in Figs. 7-10 appear identical to those displayed in the far left panels of the fourth rows in Figs. 7-10. This confirms our assertion (see Appendix A) that image boundaries can stably be reconstructed from data acquired over an angular range of  $3\pi/2$ . As images in the second, third, and fourth columns in Figs. 7-10 show, for a given noise level, image boundaries reconstructed from noisy data acquired with the reduced-scan and full-scan data appear qualitatively similar.

For completeness, we also used Norton's algorithm (Eqns. 2, 3, and 4) to reconstruct images of the Shepp-Logan phantom from data that are acquired with the short-scan and full-scan configurations in which the radius of the source-receiver trajectory is  $3r_0$ . Images reconstructed from short-scan and full-scan data are shown in the first and second rows in Fig. 11, respectively. Noiseless images are shown in the first columns in Fig. 11, whereas noisy images shown in the second, third, and fourth columns in Fig. 11 were reconstructed from data containing Gaussian noise with standard deviations of 1, 2, and 5, respectively. As expected, images reconstructed from short-scan data contain significant artifacts. Also, images reconstructed from full-scan data contain slight ringing artifacts and have poorer resolution as compared to those obtained with the EM algorithm, suggesting that Norton's algorithm is susceptible to numerical errors.

## 5 Discussion

In this work, we used a potato-peeler perspective to investigate data symmetries in reflectivity tomography. Based upon the identified data symmetries, we showed heuristically that an object function with a compact support can be specified by knowledge of half of the full-scan data. This observation has led to the development of reduced-scan configurations such as short-scan and  $\pi$ -scheme configurations in reflectivity tomography. Reduced-scan reflectivity tomography not only poses a theoretically interesting reconstruction problem, but also has practical implications. For example, in certain situations, it may not be experimentally possible to collect data over a full angular range of  $2\pi$ , thus demanding reduced-scans. A unique feature of the potato-peeler perspective is that it provides informative insights into a complex mathematical problem in a conceptually straightforward manner. We also employed the results of microlocal analysis to analyze theoretically the stability of recon-

structing image boundaries from reduced-scan data, and we derived theoretically sufficient conditions on reduced-scan configurations which acquire data for accurate reconstruction of an object function.

As predicted by microlocal analysis, certain image boundaries cannot stably be reconstructed from short-scan or  $\pi$ -scheme data in reflectivity tomography. Although artifacts due to the unstable boundary reconstruction can be observed, such artifacts appear generally weak and become difficult to discern when the data contain noise and/or when the radius  $R$  of the source-receiver trajectory becomes large. For example, for  $R = 3r_0$ , such artifacts were virtually undetectable for the ellipse and Shepp-Logan phantoms studied. This is significant because the ellipse phantom containing the square structures was specifically designed to reveal the possible instabilities of boundary reconstruction in short-scan reflectivity tomography predicted by the microlocal analysis, and because the Shepp-Logan phantom is sufficiently complex to represent many real-world reflecting objects that may be of practical interest. Conceptually, these results might be explained by the fact that the data are becoming more "Radon-like" as the radius  $R$  of the source-receiver trajectory increases. (In the limit  $R \rightarrow \infty$ , Eqn. 1 reduces to the Radon transform, and an exact image can be reconstructed from short-scan or  $\pi$ -scheme data.) Our numerical results have important practical implications: For many reflecting objects possessing boundaries and for scanning configurations with different  $R$  that may arise in realistic experiments, images reconstructed from reduced-scan data, such as the short-scan and  $\pi$ -scheme data, can have a numerical accuracy similar to that of full-scan images. The numerical results also verified the sufficient condition that all image boundaries can stably be reconstructed from reduced-scan data taken over an angular range of  $3\pi/2$ . For smooth object functions, our numerical results suggest that images can be reconstructed accurately from short-scan and  $\pi$ -scheme data.

We are currently developing a mathematical formulation for the potato-peeler perspective for reflectivity tomography and will report such results elsewhere. The perspectives and methods utilized in this work can readily be extended to investigation of, e.g., reconstruction problems in reflectivity tomography for which the source-receiver trajectory is not a circular curve, but is a general curve satisfying certain conditions. This work is also relevant to generalized Radon transforms that integrate over certain (non-circular) curves and to exterior reconstruction problems. Investigation of these topics is currently under way.

## Appendix A: Stability of Reconstructing Image Boundaries from Reduced-Scan Data

Microlocal analysis [14,18,19] can be employed for examining whether image boundaries can stably be reconstructed from reduced-scan data in reflectivity tomography. Without loss of generality, we consider boundary reconstruction from short-scan data acquired with the configurations shown in Fig. 12, where the source-receiver trajectories are semi-circles of radii  $R$  residing in the lower half plane. According to the microlocal analysis [10], a boundary can stably be reconstructed if and only if the normal vector at that boundary intersects the source-receiver trajectory [17]. For example, as shown in Fig. 12a, assume  $R = R_1$ , and consider the three boundaries labeled  $P_1$ ,  $P_2$ , and  $P_3$ . The normal vector at boundary  $P_1$  intersects the source-receiver trajectory, and therefore boundary  $P_1$  can stably be reconstructed. However, because the normal vectors at boundaries  $P_2$  and  $P_3$  do not intersect the trajectory with a radius  $R_1$ , boundaries  $P_2$  and  $P_3$  cannot stably be reconstructed. If the radius of the source-receiver trajectory is increased to be large enough, the normal vectors that are not parallel to the  $x$ -axis will eventually intersect the trajectory, and the number of boundaries that can stably be reconstructed will increase. For example, as shown in Fig. 12, when  $R = R_2$ , boundary  $P_2$  can now be reconstructed stably. Therefore, when one reconstructs an image from short-scan data in reflectivity tomography, the manifestation of artifacts due to boundaries that cannot be stably reconstructed would depend on the magnitude of  $R$ . Notice that the normal vector at boundary  $P_3$  is parallel to the  $x$ -axis, and will therefore never intersect the source-receiver trajectory with a finite radius in the lower half plane. Therefore, one can conclude that certain boundaries cannot, in theory, be reconstructed stably from short-scan data in reflectivity tomography. Similar conclusions can be made for the stability of boundary reconstruction in  $\pi$ -scheme reflectivity tomography. However, as the results in numerical studies indicated, for object functions with complicated boundaries and for source-receiver trajectories with radii  $R$  of practical interest, artifacts due to unstable reconstruction of the boundaries from short-scan and  $\pi$ -scheme data do not appear to be prominent.

Based upon the microlocal analysis, one can derive theoretically sufficient conditions for stable reconstruction of image boundaries. In the limiting case, i.e.,  $R \rightarrow \infty$ , the data function (see Eqn. 1) in reflectivity tomography reduces to the Radon transform, and normal vectors of any boundaries will intersect the source-receiver trajectory at infinity. Therefore, all of the boundaries can stably be reconstructed from short-scan or  $\pi$ -scheme Radon data. Also, considering the scanning configuration in the fourth panel of Fig. 5, the source-receiver trajectory of radius  $R$  in this configuration covers an angular interval of  $3\pi/2$ . In this case, it can readily be verified that any normal vectors on image boundaries intersect the source-receiver trajectory. Therefore, one can obtain a sufficient condition



that all of the boundaries can stably be reconstructed from data acquired over a reduced angular interval that spans  $3\pi/2$ . Furthermore, one can design a scanning configuration such that all of the boundaries within an object function can stably be reconstructed from, e.g., the short-scan data. As shown in Fig. 12b, for the entire object that is placed in the lower half of the plane and is enclosed by the source-receiver trajectory, all boundaries in the object can stably be reconstructed because their normal vectors, in this situation, intersect the source-receiver trajectory.

## Acknowledgments

The authors thank Dr. E. T. Qunito for helpful communications regarding the application of microlocal analysis to this work.

## References

- [1] J. Ylitalo, J. Kaovukangas, and J. Oksman. Ultrasonic reflection mode computed tomography through a skullbone. *IEEE Transactions on Biomedical Engineering*, 37:1059–1065, 1990.
- [2] K. Dines and A. Goss. Computer ultrasonic reflection tomography. *IEEE Transactions on Ultrasonics, Ferroelectrics and Frequency Control*, 34:309–317, 1987.
- [3] M. Moshfeghi. Ultrasound reflection-mode tomography using fan-shaped-beam insonification. *IEEE Transactions on Ultrasonics, Ferroelectrics and Frequency Control*, 33:299–314, 1986.
- [4] S. Norton. Reconstruction of a two-dimensional reflecting medium over a circular domain: Exact solution. *Journal of the Acoustical Society of America*, 67(4):1266–1273, 1980.
- [5] S. Norton and M. Linzer. Ultrasonic reflectivity imaging in three dimensions: Exact inverse scattering solutions for plane, cylindrical, and spherical apertures. *IEEE Transactions on Biomedical Engineering*, 28:202–220, 1981.
- [6] D. Parker. Optimal short scan convolution reconstruction for fanbeam CT. *Medical Physics*, 9:254–257, 1982.
- [7] F. Noo and J. Wagner. Image reconstruction in 2D SPECT with  $180^\circ$  acquisition. *Inverse Problems*, 17:1357–1371, 2001.

- [8] X. Pan, C. M. Kao, and C. E. Metz. A family of  $\pi$ -scheme exponential Radon transforms and the uniqueness of their inverses. *Inverse Problems*, 18:825–836, 2002.
- [9] E. Somersalo, M. Cheney, D. Isaacson, and E. Isaacson. Layer stripping: a direct numerical method for impedance imaging. *Inverse Problems*, 7:899–926, 1991.
- [10] A. K. Louis and E. T. Quinto. Local tomographic methods in SONAR. In *Surveys on Solution Methods for Inverse Problems*. Springer-Verlag, To appear (2002).
- [11] Y. Vardi and D. Lee. From image deblurring to optimal investments: Maximum likelihood solutions for positive linear inverse problems. *Journal of the Royal Statistical Society B*, 55:569–612, 1993.
- [12] X. Pan, E. Sidky, C. Kao, Y. Zou, and C. E. Metz. Image reconstruction in  $\pi$ -scheme SPECT with non-uniform attenuation. *IEEE Transactions on Nuclear Science*, (submitted), 2002.
- [13] M. Agranovsky and E. T. Quinto. Injectivity of the Radon transform over circles and complete systems of radial functions. *Journal of Functional Analysis*, 139:383–414, 1996.
- [14] E. T. Quinto. Radon transforms, differential equations, and microlocal analysis. In E. Quinto, L. Ehrenpreis, A. Faridani, F. Gonzalez, and E. Grinberg, editors, *Radon Transforms and Tomography*, Contemporary Mathematics. American Mathematical Society, 2001.
- [15] L. A. Shepp and Y. Vardi. Maximum likelihood reconstruction for emission tomography. *IEEE Transactions on Medical Imaging*, 1:113–122, 1982.
- [16] H. Hudson and R. Larkin. Accelerated image reconstruction using ordered subsets of projection data. *IEEE Transactions on Medical Imaging*, 13:601–609, 1994.
- [17] E. T. Quinto, 2002. Department of Mathematics, Tufts University, Personal Communication.
- [18] E. T. Quinto. Singularities of the X-ray transform and limited data tomography in  $\mathbf{R}^2$  and  $\mathbf{R}^3$ . *SIAM Journal on Mathematical Analysis*, 24:1215–1225, 1993.
- [19] V. Guillemin and S. Sternberg. Some problems in integral geometry and some related problems in micro-local analysis. *American Journal of Mathematics*, 101:915–955, 1979.

## Figure Captions

1. Schematic illustration of the scanning geometry in reflectivity tomography.
2. Schematic illustration of the measurements at the edge of an object function in reflectivity tomography (left panel). Points A, B, and C in the object function contribute to the measured data on curves with the same labels in the data space (right panel).
3. Numerical phantoms used in simulation studies. The phantom in the left panel, which is referred to as the Gaussian phantom, is comprised of three Gaussian functions, representing a smooth object function. The phantoms in the middle and right panels, which contain boundaries (i.e., discontinuities), are referred to as the ellipse and Shepp-Logan phantoms, respectively, and are used to investigate boundary-reconstruction stability from short-scan and  $\pi$ -scheme data in reflectivity tomography.
4. Profiles through difference images at  $x = 64$  (left) and  $y = 44$  (right) obtained from data acquired over  $[0, \pi)$  (solid),  $[0, 3\pi/4)$  (dotted), and  $[0, \pi/2)$  (dashed).
5. Scanning configurations that acquire data over angular intervals  $[0, \pi/2)$  (left),  $[\pi, 2\pi)$  (second from left),  $[\pi/3, 2\pi/3] \cup [\pi, 4\pi/3] \cup [5\pi/3, 2\pi]$  (middle),  $[0, 3\pi/2)$  (second from right), and  $[0, 2\pi)$  (right). The configurations in the second, third, and fifth panels are also referred to as the short-scan,  $\pi$ -scheme, and full-scan configurations, respectively.
6. Images reconstructed from noiseless and noisy data acquired over  $[0, \pi/2)$  for the ellipse and Shepp-Logan phantoms. The radii of the source-receiver trajectory were set to  $r_0$  in (a) and (c), and  $3r_0$  in (b) and (d). Images in the first column were reconstructed from noiseless data, and images in the second, third, and fourth columns were reconstructed from data containing three different levels of Gaussian noise. All of these images contain significant distortions, suggesting that images cannot accurately be reconstructed from data acquired over angular intervals less than  $\pi$ .
7. Images reconstructed for the ellipse phantom from data acquired over angular intervals  $[\pi, 2\pi)$  (1st row),  $[\pi/3, 2\pi/3] \cup [\pi, 4\pi/3] \cup [5\pi/3, 2\pi]$  (2nd row),  $[0, 3\pi/2)$  (3rd row), and  $[0, 2\pi)$  (4th row). The radius of the source-receiver trajectory is  $r_0$ . Images in the first column were reconstructed from noiseless data, and images in the second, third, and fourth columns were reconstructed from data containing three different levels of Gaussian noise.
8. Images reconstructed for the ellipse phantom from data acquired over angular intervals

$[\pi, 2\pi)$  (1st row),  $[\pi/3, 2\pi/3] \cup [\pi, 4\pi/3] \cup [5\pi/3, 2\pi]$  (2nd row),  $[0, 3\pi/2)$  (3rd row), and  $[0, 2\pi)$  (4th row). The radius of the source-receiver trajectory is  $3r_0$ . Images in the first column were reconstructed from noiseless data, and images in the second, third, and fourth columns were reconstructed from data containing three different levels of Gaussian noise.

9. Images reconstructed for the Shepp-Logan phantom from data acquired over angular intervals  $[\pi, 2\pi)$  (1st row),  $[\pi/3, 2\pi/3] \cup [\pi, 4\pi/3] \cup [5\pi/3, 2\pi]$  (2nd row),  $[0, 3\pi/2)$  (3rd row), and  $[0, 2\pi)$  (4th row). The radius of the source-receiver trajectory is  $r_0$ . Images in the first column were reconstructed from noiseless data, and images in the second, third, and fourth columns were reconstructed from data containing three different levels of Gaussian noise.

10. Images reconstructed for the Shepp-Logan phantom from data acquired over angular intervals  $[\pi, 2\pi)$  (1st row),  $[\pi/3, 2\pi/3] \cup [\pi, 4\pi/3] \cup [5\pi/3, 2\pi]$  (2nd row),  $[0, 3\pi/2)$  (3rd row), and  $[0, 2\pi)$  (4th row). The radius of the source-receiver trajectory is  $3r_0$ . Images in the first column were reconstructed from noiseless data, and images in the second, third, and fourth columns were reconstructed from data containing three different levels of Gaussian noise.

11. Images reconstructed by use of Norton's algorithm from short-scan data (1st row) and full-scan data (2nd row) that were acquired with a circular source-trajectory of radius  $R = 3r_0$ . Images in the first column were reconstructed from noiseless data, and images in the second, third, fourth columns were reconstructed from data containing three different levels of Gaussian noise.

12. Short-scan configurations and boundaries in the objects. (a) Some of the boundaries such as  $P_2$  and  $P_3$  reside in the upper half plane; and (b) the entire object resides in the lower half plane and is enclosed by the source-receiver trajectory.

## Figures

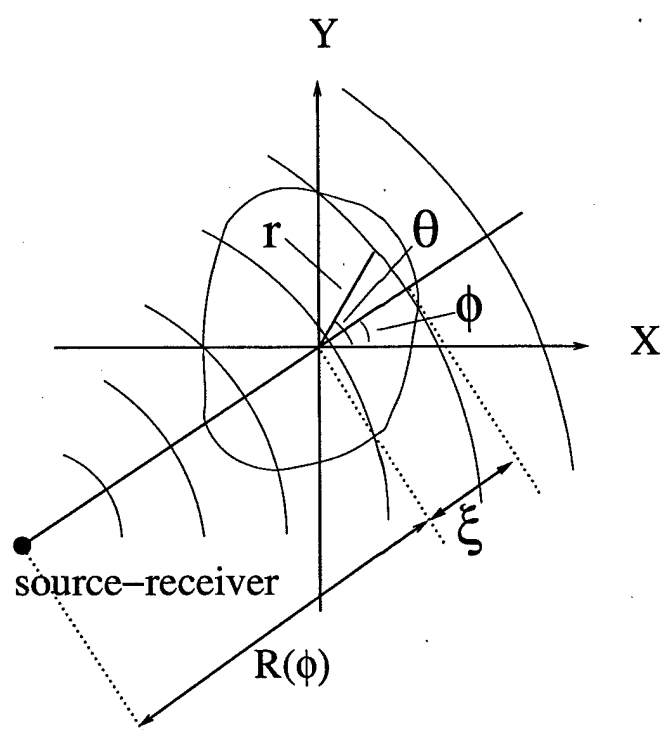


Figure 1:

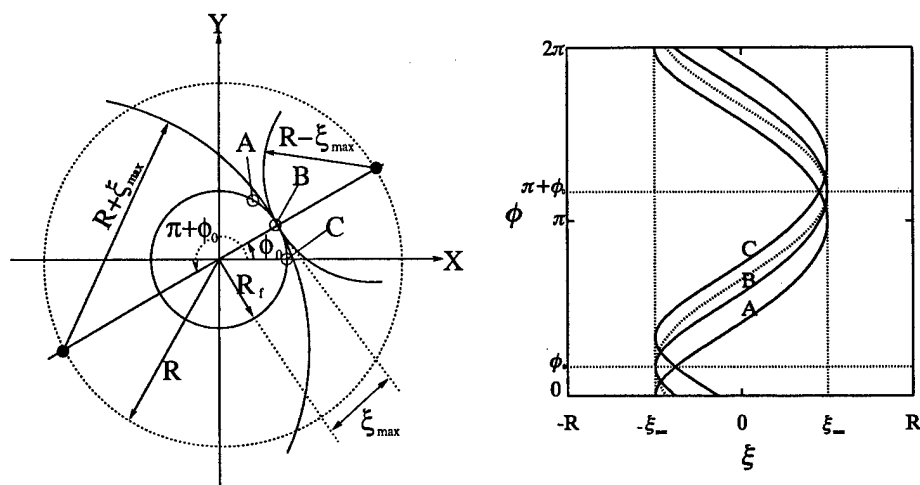


Figure 2:

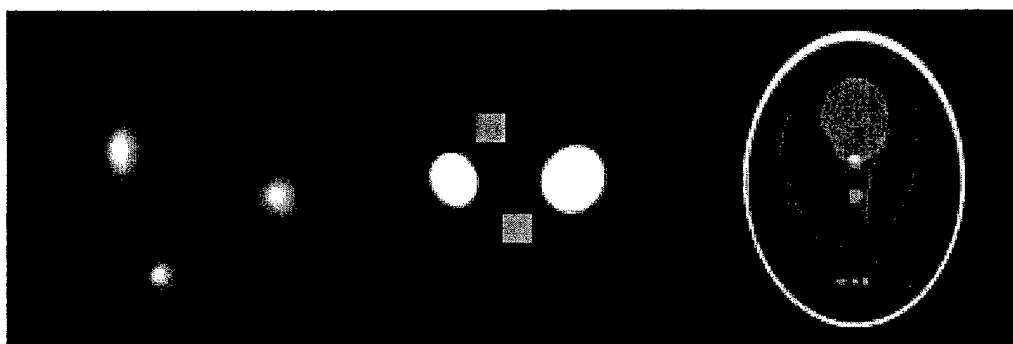


Figure 3:

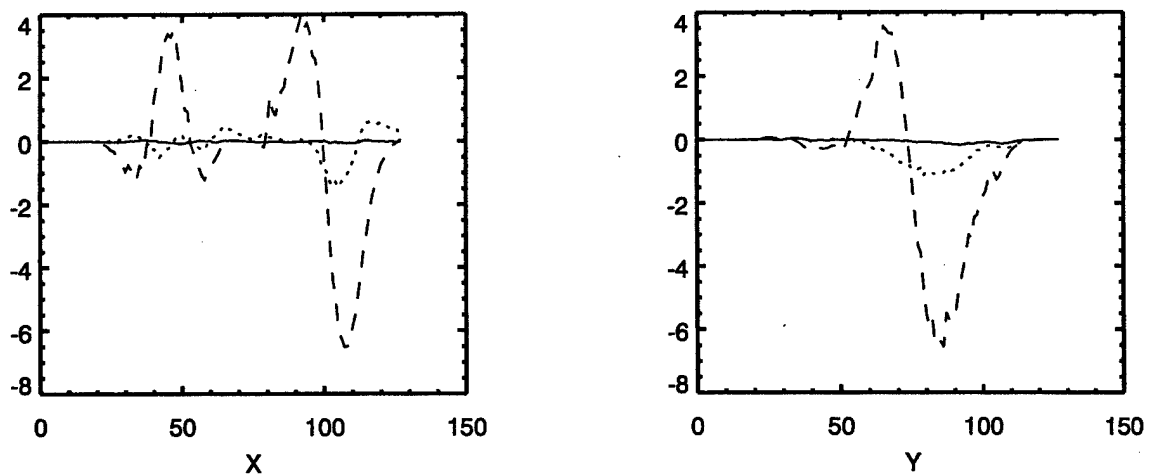


Figure 4:

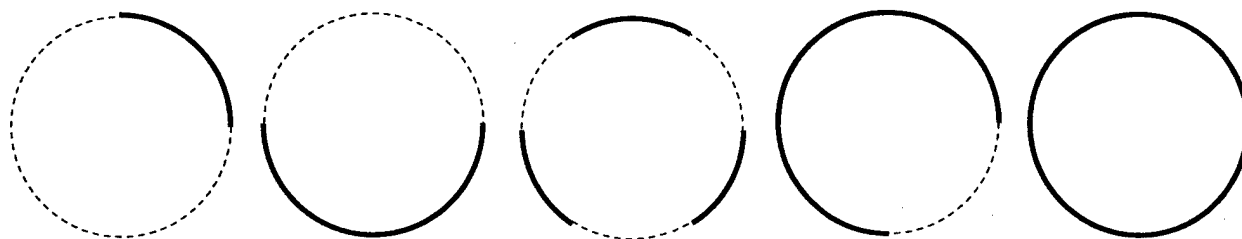


Figure 5:

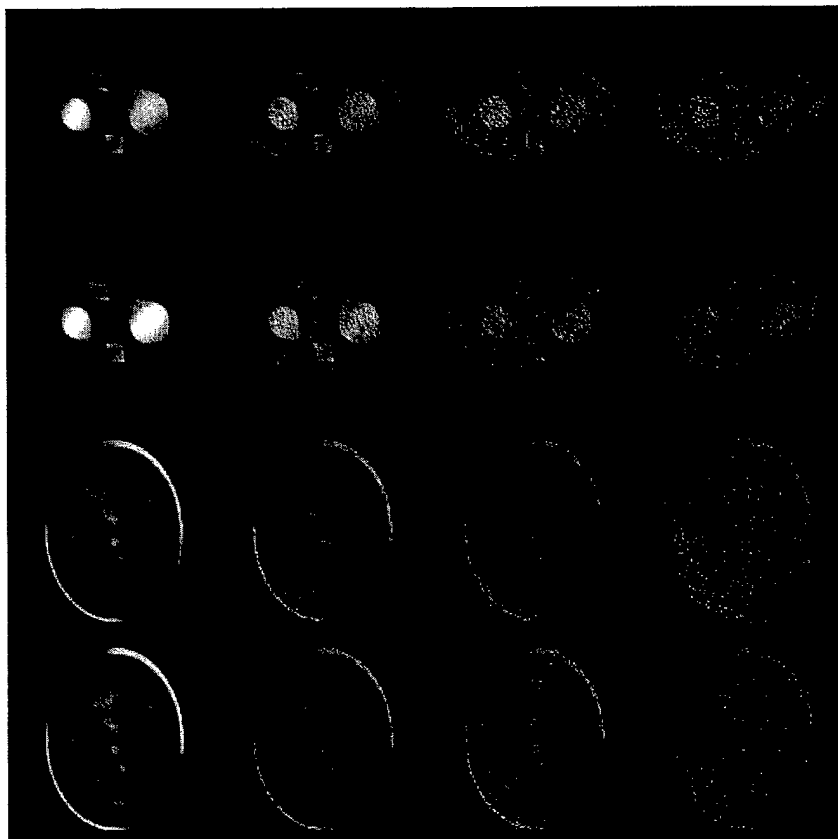


Figure 6:



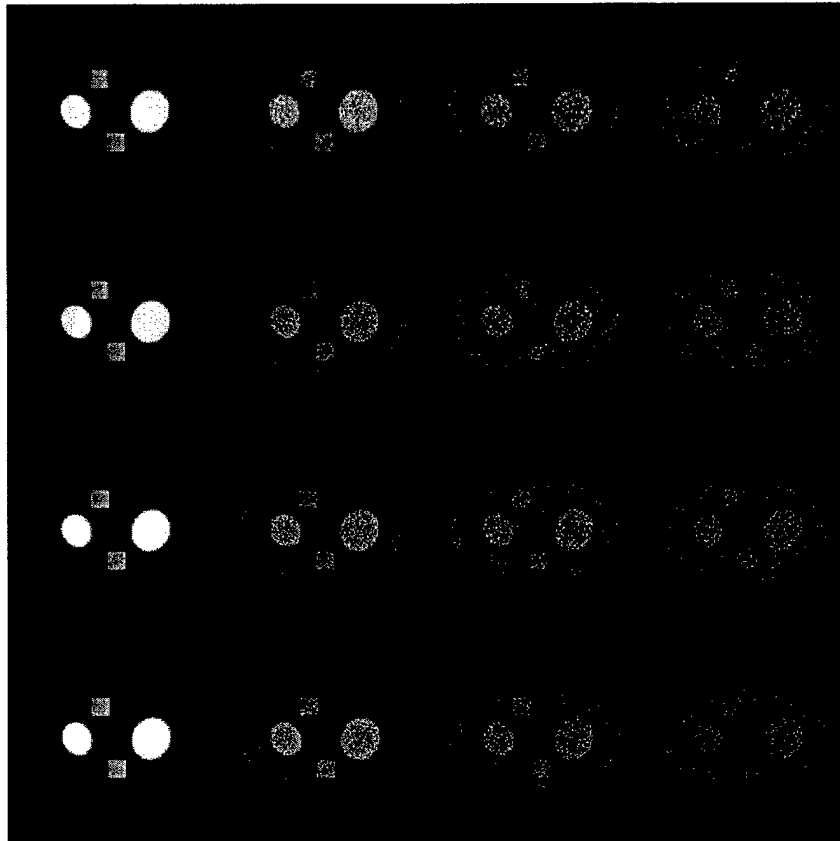


Figure 7:

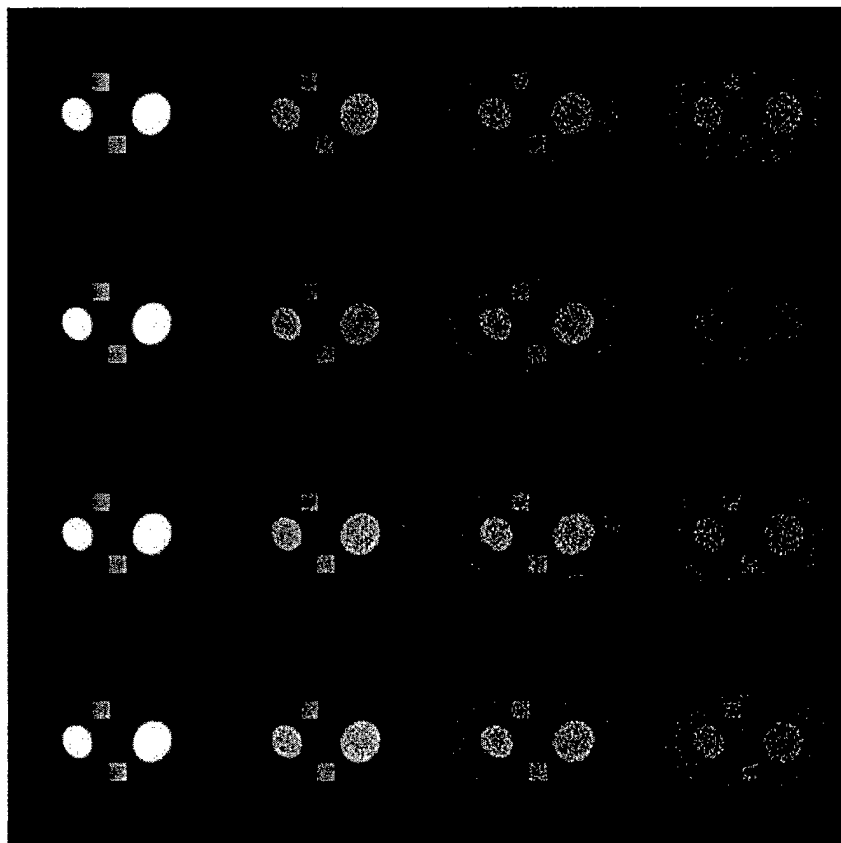


Figure 8:

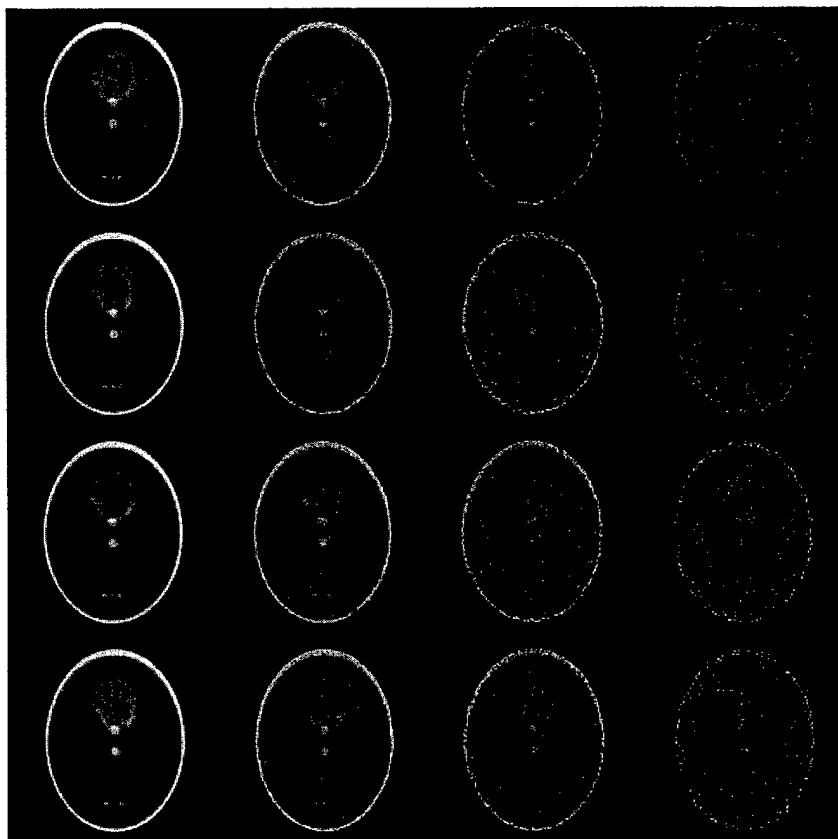


Figure 9:

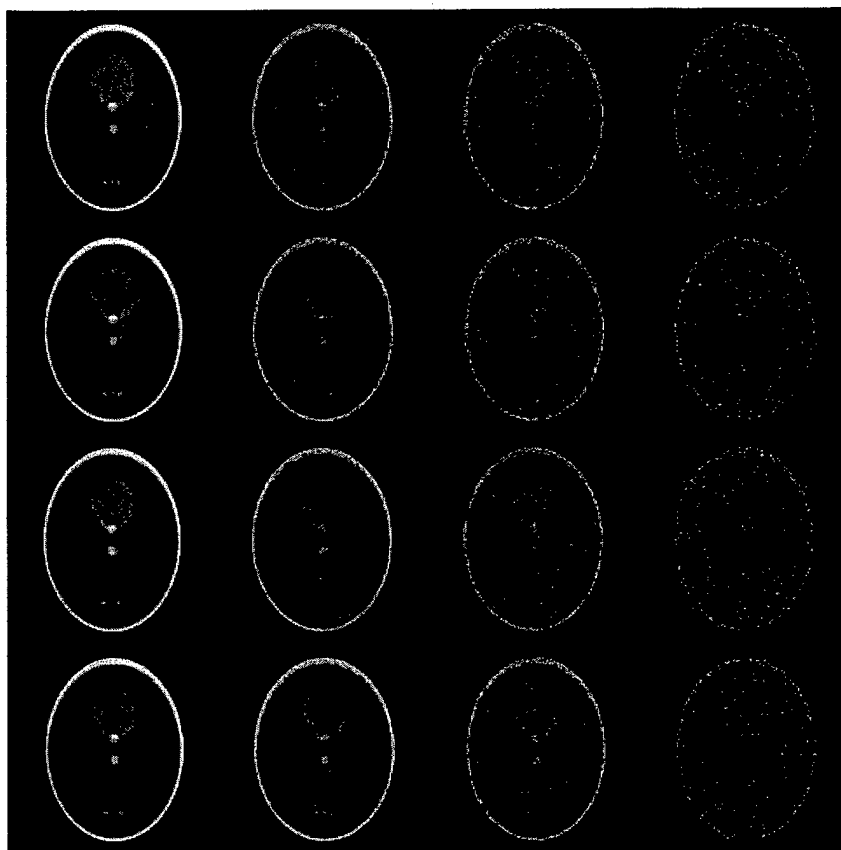


Figure 10:

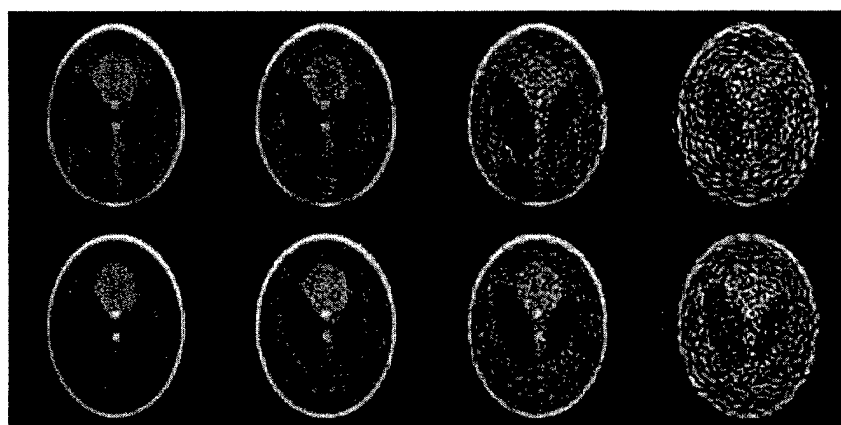
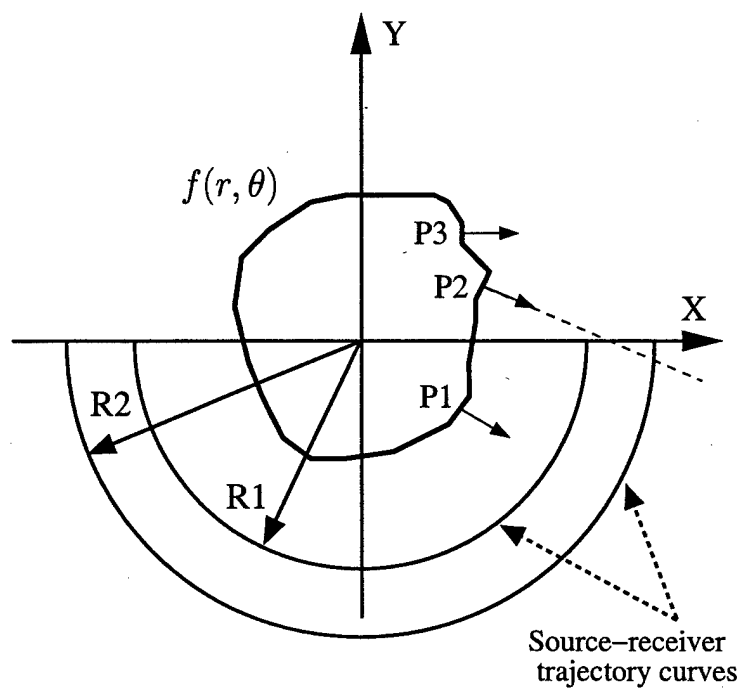
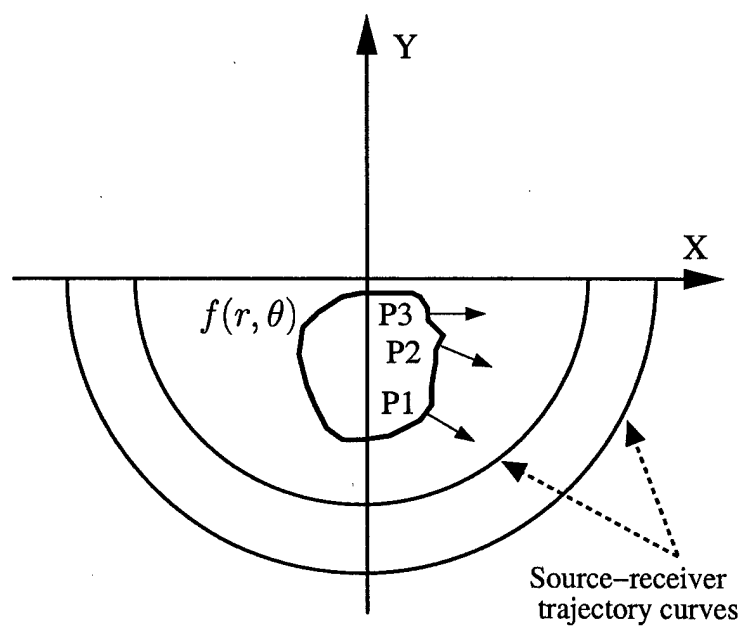


Figure 11:



(a)



(b)

Figure 12: